Sedimentary processes controlling ultralong cells of littoral transport : placer formation and termination of the Orange sand highway in southern Angola

EDUARDO GARZANTI[1*], PEDRO DINIS[2], PIETER VERMEESCH[3], SERGIO ANDÒ[1], ANNETTE HAHN[4], JOÃO HUVI[5], MARA LIMONTA[1], MARTA PADOAN[1] ALBERTO RESENTINI[1], MARTIN RITTNER[3], GIOVANNI VEZZOLI[1]

[1] *Laboratory for Provenance Studies, Department of Earth and Environmental Sciences, Università di Milano-Bicocca, 20126 Milano, Italy*

[2] *IMAR-CMA Centro do Mar e Ambiente, Departamento de Ciências da Terra, Universidade de Coimbra, Largo Marquês de Pombal, 3000-272 Coimbra, Portugal*

[3] *London Geochronology Centre, Department of Earth Sciences, University College London, London WC1E 6BT, UK*

[4] *MARUM Center for Marine Environmental Sciences, University of Bremen, Bremen, Germany*

[5] *Marine and Environmental Sciences Centre, University Katyavala Bwila, Angola*

* Corresponding author. Tel.: +39-02-64482088

E-mail: eduardo.garzanti@unimib.it (E. Garzanti), pdinis@dct.uc.pt (P. Dinis), p.vermeesch@ucl.ac.uk (P.Vermeesch), sergio.ando@unimib.it (S. Andò), ahahn@marum.de (A.Hahn), hjoaobaptistahuvi@yahoo.com.br (J.Huvi), mara.limonta@unimib.it (M.Limonta), marta.padoan@unimib.it (M.Padoan), alberto.resentini@unimib.it (A. Resentini), m.rittner@ucl.ac.uk (M.Rittner), giovanni.vezzoli@unimib.it (G. Vezzoli)

Key words: Sedimentary petrology, heavy minerals, detrital-zircon geochronology, Raman counting of deep-sea silt, grain density and geochemistry of placer deposits, garnet and pyroxene chemistry, longshore sediment transport, Moçamedes Desert and Cunene River sands.

ABSTRACT

This study focuses on the causes, modalities and obstacles of sediment transfer in the longest cell of littoral sand drift documented on Earth so far. Sand derived from the Orange River is dragged by swell waves and persistent southerly winds to accumulate in four successive dunefields in coastal Namibia to Angola. All four dunefields are terminated by river valleys, where eolian sand is flushed back to the ocean. And yet sediment transport continues at sea, tracing a 1800 km-long submarine sand highway. Sand drift would extend northward to beyond the Congo if the shelf did not become progressively narrower in southern Angola, where drifting sand is funnelled towards oceanic depths via canyon heads connected to river mouths. Garnet-magnetite placers are widespread along this coastal stretch, indicating systematic loss of the low-density feldspatho-quartzose fraction to the deep ocean. More than half of Moçamedes Desert sand is derived from the Orange River, and the rest in similar proportions from the Cunene River and from the Swakop and other rivers draining the Damara orogen in Namibia. The Orange fingerprint, characterized by basaltic rock fragments, clinopyroxene grains, and bimodal zircon-age spectra with peaks at ~0.5 and ~1.0 Ga, is lost abruptly at Namibe, and beach sands farther north have abundant feldspar, amphibole-epidote suites, and unimodal zircon-age spectra with peak at ~2.0 Ga, documenting local provenance from Paleoproterozoic basement. Along this oblique-rifted continental margin, beach placers are dominated by Fe-Ti-Cr oxides with more monazite than garnet, and thus have a geochemical signature sharply different from beach placers found all along the Orange littoral cell. High-resolution mineralogical studies allow us to trace sediment dispersal over distances of thousands of kilometers, providing essential information for the correct reconstruction of source-to-sink relationships in hydrocarbon exploration and to predict the long-term impact of man-made infrastructures on coastal sediment budgets.

Water dissolving ... and water removing / There is water at the bottom of the ocean /
Letting the days go by / Water flowing underground / Into the blue again /
Into the silent water / Under the rocks and stones / There is water underground /
And you may ask yourself / Where does that highway go to?
Talking Heads, Once in a lifetime, 1980.

INTRODUCTION

The long-distance transfer of huge detrital masses from one site to another on the Earth's surface is of essence to understand sedimentological processes, enhance the resolution of source-to-sink studies for hydrocarbon exploration, and improve the quality of environmental management (Dickinson, 1988; Kaminsky *et al.*, 2010; Scott *et al.*, 2014). Hundreds of million tons of sediment are carried each year for thousands of kilometers along the largest fluvial systems, such as the Amazon, the Ganga-Brahmaputra or the Yellow River (Hay, 1998; Milliman & Farnsworth, 2011). Equally established is the underwater transport of large sediment volumes over similar distances via turbidity currents, as across the present Bengal and Indus Fans or their ancient analogues (Ingersoll *et al.*, 2003). Far less documented is the transport of large sediment volumes in the shallow sea, which can cover distances of a thousand kilometers and more under the action of persistent longshore currents. The major implications of littoral sediment transport for the paleogeographic interpretation of ancient sedimentary deposits remain notably underexplored.

Only a few cases of modern ultralong-distance littoral sand transport have been documented in detail so far. Swell-driven coastal-transport systems hundreds of kilometers in length exist in many parts of the world (Silvester, 1962; Davies, 1972), as in southern Brasil (Calliari & Toldo, 2016) or eastern Australia, where sand is dragged alongshore for ~1500 km to north of Fraser Island, the largest sand island on Earth (Boyd *et al.*, 2008). Even longer is the littoral cell fed by the Orange River, the object of the present study, rivaled in length only by the mud-dominated Amazon cell

(Allison & Lee, 2004; dos Santos *et al.*, 2016). Littoral dispersal of Nile sand under the action of longshore currents fuelled by strong northwesterly winds, which has fed the beaches of Gaza and Israel through most of the Quaternary, terminates at Haifa Bay and Akhziv submarine canyon ~700 km from the Delta (Inman & Jenkins, 1984; Garzanti *et al.*, 2015a). The littoral cell associated with the Columbia River, the third largest in the United States by discharge, extends for 165 km only (Ruggiero *et al.*, 2005), although sand transport by turbidity currents continues for ~1100 km along a devious route reaching far into the Pacific Ocean (Zuffa *et al.*, 2000).

The present article builds upon previous studies that monitored sediment dispersal along the Atlantic coast of southern Africa – from the Orange River to the Namib Erg, and beyond to the Skeleton Coast and Moçamedes Desert of southernmost Angola (Vermeesch *et al.*, 2010; Garzanti *et al.*, 2012a, 2014, 2015b) – and focuses on physical processes of sediment mixing and unmixing in the terminal tract of this ultralong submarine sand highway (Fig. 1). We will investigate specifically provenance of sand accumulating in the Moçamedes Desert north of the Cunene River mouth (Fig. 2) and along the Angolan coast farther north (Fig. 3), in order to understand where, how, and why the compositional fingerprint of Orange-derived sand is eventually lost after ~1800 km of littoral drift. We will examine whether and to what extent northward sand transport is blocked on land by incised river valleys and/or at sea by submarine canyons, the influence of atmospheric and oceanic circulation, and the role played by shelf width, representing both a control and a consequence of longshore sediment drift. An accurate evaluation of such factors is essential to understand the physical processes promoting such a large-scale transfer of sediment volumes, and how they are reflected in the composition of continental-margin sediments.

THE ANGOLAN COAST

The coastal region of southern Angola is affected profoundly by atmospheric and oceanic circulation in the southeastern Atlantic Ocean. Here the warm, southward flowing Angola Current converges with the cold, northward flowing Benguela Current, forming the Angola-Benguela front (Meeuwis & Lutjeharms, 1990; Shannon & Nelson, 1996; Lass *et al.*, 2000). Reflecting this oceanic circulation pattern and the influence of the subtropical high-pressure system, climate along the coast is very arid between ~30ºS and ~15ºS. Annual rainfall increases progressively from as low as 15 mm at Foz do Cunene and Baia dos Tigres, to 20 mm at Tombua, 50 mm at Namibe, and 200 mm at Lobito (Guilcher, 2010). Rainfall increases much more rapidly inland to reach 1000-1500 mm/a in the mountainous hinterland, where climate becomes humid subtropical, temperate-highland tropical with dry winters, or even of savanna type (Peel *et al.*, 2007; Jury, 2010). This gradient is blurred at latitudes > 20ºS, where rainfall hardly reaches 500 mm/a in the hinterland and temperature decreases significantly marking the transition to cold desert climate. Southerly to south-westerly winds generated in subtropical high-pressure systems prevail throughout the year; inversions may take place during the night, when continental areas become colder than the ocean.

The intensities of the Angola and Benguela currents are seasonally variable and the position of the Angola-Benguela front usually shifts between 14°S and 16°S (Hardman-Mountford *et al.*, 2003), north of which climate changes from hot desert to hot semi-arid. Responding to seasonal variation in oceanic circulation and solar radiation, the region is characterized by alternating wet and dry seasons varying with latitude and distance from the coast. In the continental hinterland, the rainy season usually starts in September or October and lasts up to 7 months at lower latitudes, whereas it may be delayed until December at higher latitudes. No rainy season exists along the hyperarid southern coast, where much of the precipitation is in the form of fog (locally called *cassimbo*). The region is also affected by the so-called Benguela Niño, when the Angola-Benguela front is displaced southward causing the advection of warm, highly saline waters as far as 25°S (Shannnon *et al.*, 1986; Kirst *et al.*, 1999; Rouault *et al.*, 2007). The recurrence of major floods, as those of the Bero and Giraul Rivers in April 2001 or March 2011 that caused casualties of tens of people, displacement of thousands of families, and loss of a large extent of arable land, may be associated with the Benguela Niño phenomenon (Manhique *et al.*, 2015). Estimates on sediment volumes carried at sea during such catastrophic events are unfortunately lacking.

The microtidal coast of Angola (mean spring tide 1-2 m) is characterized by extensive northward sediment transport. Littoral drift is generated by a powerful southerly swell originating from persistent stormy winds between 40° and 60°S, far away in the Southern Ocean. Scarcely affected by either local winds or the Benguela Current, such wave-driven transport system extends from Cape Town to the Gulf of Guinea, its direction being controlled by the oblique incidence of the wave front to the coast. In proximity of coastal re-entrants, waves are refracted and lose their longshore transporting capacity; sand thus accumulates offshore as a sand spit. Before it was detached from shore in March 1962, the 37 km-long spit enclosing Baia dos Tigres, characterized by 60 m-thick sand deposits at its northern end and completely devoid of vegetation owing to hyperarid climate, was the longest of the African coast (Guilcher *et al.*, 1974).

SAMPLING AND ANALYTICAL METHODS

In order to monitor changes in sediment composition in the terminal tract of the Orange littoral cell, 24 sand samples of beach, eolian and fluvial sands from south of Tombua to Lucira were collected in southern Angola in June 2015, including three beach placers (Fig. 4). To quantify provenance of dune and beach sand in the Moçamedes coastal desert, and to establish whether and in what proportions it was derived proximally from the Cunene River or long-distance from the Orange River, this sample set was integrated with 10 beach and dune samples collected from Foz do Cunene to Tombua mostly in January 2016 (Fig. 5), 13 samples collected between 2008 and 2016 from the Cunene River and its Angolan and Namibian tributaries, one Hoarusib River sand, and one fossil dune collected in the terminal tract of the Curoca valley. To monitor sediment transport across the shelf to the deep sea, we have analysed several sediment samples retrieved from the MARUM repository in Bremen (Fig. 1). Offshore samples were collected mostly with a giant box corer just below the seafloor, on the Walvis Ridge (Meteor Expedition M20/2, Sites GeoB1704 and GeoB1705; Schulz *et al.*, 1992) and seaward of the Cunene mouth (Meteor Expedition M6/6, Sites GeoB1019 to GeoB1022; Wefer *et al.*, 1988). Three samples are from the upper ~8 meters of two 52 m and 38 m-long cores spanning the last Ma drilled offshore of Baia dos Tigres during ODP Leg 175 (Site 1080; Wefer *et al.*, 1998). Sixty-one samples were considered overall (full information on sampling sites is provided in Appendix Table A1 and Google Earth file *Mocamedes.kmz*).

Petrography and heavy minerals

Bulk sand was impregnated with araldite, cut into a thin section, and analysed by counting 400 points under the microscope (Gazzi–Dickinson method; Ingersoll *et al.*, 1984). Metamorphic rock fragments were subdivided into very low to low-rank metasedimentary (Lms) or metavolcanic (Lmv), and medium to high-rank felsic (Lmf) or mafic (Lmb) categories (Garzanti & Vezzoli, 2003). Sand classification is based on the main components quartz, feldspars and lithic fragments considered if exceeding 10%QFL (e.g., a sand is named feldspatho-quartzose if Q > F > 10%QFL > L; Garzanti, 2016).

Heavy-mineral analyses were carried out on a quartered aliquot of the bulk sample or < 500 µm fraction for well sorted eolian and beach sands, and of the 15-500 µm class obtained by wet-sieving for fluvial sands. Heavy minerals were separated by centrifuging in sodium polytungstate (density ~2.90 g/cm^3), and recovered by partial freezing with liquid nitrogen. On grain mounts, 200-250 transparent heavy-mineral grains were point-counted at suitable regular spacing under the petrographic microscope to obtain real volume percentages (Galehouse, 1971). On offshore samples, heavy-mineral analyses were carried out by Raman point-counting (Andò *et al.*, 2011) on the > 5 µm (silty-clay samples) or > 15 µm fraction (sandy-silt to silty-sand samples) obtained by wet sieving. Three beach-placer deposits were analysed by grain-counting, point-counting, and Raman point-counting of bulk-sample slides. Raman spectroscopy analyses, carried out with a

Raman Renishaw inVia, were used to identify opaque Fe-Ti-Cr oxide grains, to assess the chemical composition of detrital pyroxenes and garnets, and to check the determination of altered or dubious transparent heavy minerals (Andò & Garzanti, 2014).

Heavy-mineral concentration, calculated as the volume percentage of total (HMC) and transparent (tHMC) heavy minerals, ranges from extremely poor (HMC < 0.1) and poor (0.5 ≤ HMC < 1), to rich (5 ≤ HMC < 10), very rich (10 ≤ HMC < 20), and extremely rich (20 ≤ HMC < 50); placer sands are defined by HMC ≥ 50. The Source Rock Density (SRD) index of Garzanti & Andò (2007), defined as the weighted average density of extrabasinal terrigenous grains, was used to detect and correct for hydraulic-controlled concentration of denser minerals. Detrital components are listed in order of abundance throughout the text. The complete petrographic and mineralogical datasets and grain-density measurements are provided in Appendix Tables A2 to A7.

Geochemistry and detrital-zircon geochronology

Chemical analyses of 22 selected samples, including three beach placers, were carried out at ACME Laboratories (Vancouver) on a quartered aliquot of the 63-2000 μm class obtained by wet-sieving. Following a lithium metaborate/tetraborate fusion and nitric acid digestion, major oxides and several minor elements were determined by ICP-ES and trace elements by ICP-MS (see http://acmelab.com for detailed information on adopted procedures, standards used, and precision for elements of group 4A-4B and code LF200).

The U-Pb ages of detrital zircons identified by QEMScan electron microscopy (Vermeesch *et al.*, 2017) on heavy-mineral separates of 25 selected samples (mostly < 500 or 15-500 μm size class) were determined at the London Geochronology Centre using an Agilent 7700 LA-ICP-MS system, employing a New Wave NWR193 Excimer Laser operated at 11 Hz with a 20 μm spot size and 2.5-3.0 J/cm^2 fluence. No cathodoluminesce-imaging was done. Data reduction was peformed using GLITTER 4.4.2 software (Griffin *et al.*, 2008). $^{206}Pb/^{238}U$ and $^{207}Pb/^{206}Pb$ ages were used for zircons younger and older than 1100 Ma, respectively. No common Pb correction was applied. Grains with +5/-15% age discordance were discarded, and 1423 concordant ages were obtained overall. Geochemical and geochronological datasets are provided in Appendix Table A8 and Appendix B.

TRACING ORANGE SAND TO SOUTHERN ANGOLA

This section illustrates the petrographic, mineralogical, and geochronological fingerprints of sand-sized sediments from the Orange mouth to southern Angola, focusing on the Cunene catchment (Fig. 6) and Moçamedes Desert (Fig. 7).

Orange River sand

The Orange River has remained the most prominent sand source to coastal Namibia through most of the Neogene, as inferred from mapping of sedimentary facies and longshore patterns of swell-driven littoral drift (Rogers, 1977; Rogers & Bremner, 1991 p.24). The Orange catchment includes much of South Africa, where source rocks range from Archean and Paleoproterozoic basements exposed north of its Vaal tributary to the Carboniferous-Lower Jurassic Karoo siliciclastics capped by flood basalts in Lesotho (Fig. 8). Orange sand is feldspatho-litho-quartzose to litho-feldspatho-quartzose, with plagioclase prevailing over K-feldspar, and equally abundant mafic volcanic/subvolcanic and sedimentary (shale/sandstone, carbonate) rock fragments. Heavy-mineral suites are rich and clinopyroxene-dominated, with subordinate opaque Fe–Ti–Cr oxides, epidote, amphibole, and garnet. The remarkably homogeneous clinopyroxene chemistry indicates provenance from Karoo basalts (fig. 5 in Garzanti *et al.*, 2012). U/Pb zircon ages are characterized by prominent Damara and Namaqua peaks at ~0.6 and ~1.0 Ga, with a few older grains clustering at 1.8-2.1 Ga and younger grains at ~0.3 Ga (fig. 1 in Vermeesch *et al.*, 2010).

Sand of coastal Namibia

Sand and gravel delivered at the Orange mouth are dragged northward by a powerful longshore drift, whereas mud is largely carried offshore and southward (Rogers & Rau, 2006). Much of the sand, retained within the breaker zone and moving northward in a ≤ 3 km wide belt (Spaggiari *et al.*, 2006), bypasses the Sperrgebiet deflation area and accumulates in the Namib Erg (Corbett, 1993). Dune and beach sands of the Coastal Namib Erg are feldspatho-quartzose volcaniclastic with rich clinopyroxene-dominated suites including garnet, amphibole and epidote, and display the same clinopyroxene chemistry and zircon-age spectra of Orange sand, indicating that they are derived virtually entirely from the Orange mouth.

Littoral sand drift continues to beyond Walvis Bay (Bluck *et al.*, 2007). New corridors of eolian transport form ~350 km to the north, where coastal orientation changes to SSE/NNW and sand is blown landward to accumulate in the Skeleton Coast Erg (Lancaster, 1982). Relative to Coastal Namib dunes, Skeleton Coast dunes have less volcanic rock fragments, less pyroxene, and more staurolite, garnet, tourmaline, and amphibole (Fig. 9). The geochemical signatures of detrital clinopyroxenes are the same, indicating that only a few are derived locally from Etendeka lavas (fig. 4 in Garzanti *et al.*, 2014). Garnet grains are mostly almandine-pyrope as in Coastal Namib sands, but some almandine-spessartine grains similar to those carried by the Swakop River are found. U-Pb age spectra of detrital zircons show the same prominent Damara and Namaqua peaks as in Orange and Coastal Namib sands. Petrographic, mineralogical, geochemical, and geochronological data concur to indicate that Skeleton Coast dune sand is derived mostly from the Orange River and ~20% from metamorphic and granitoid rocks of the Damara Orogen principally via the Swakop River.

Other rivers drain the Damara Orogen (Kuiseb, Omaruru, Ugab, Huab, Hoanib) or the Etendeka volcanic province (Koigab, Uniab), but owing to arid climate their sediment contribution to coastal sand is minor. Summer thunderstorms in the mountainous hinterland may generate high-magnitude floods that last several days, but otherwise they may experience several years of drought. The Hoarusib River farther north receives higher rainfall, and more frequent flows reach the ocean almost every year (Jacobson *et al.*, 1995). Hoarusib sand is feldspatho-quartzose with moderately rich epidote-amphibole suite. Detrital-zircon ages display a major cluster between 1668 and 1863 Ma (56% of ages, with peak around 1850 Ma) and a lesser cluster between 1261 and 1423 Ma (19% of ages; Appendix B).

The Cunene Erg, starting with barchan trains and linear sand streaks north of Cape Frio and bounded to the north by the Cunene River, is characterized by crescentic dunes near the coast and curving linear ridges inland (Goudie & Viles, 2015).

Cunene River sand

The perennial Cunene River (basin area 10^5 km^2, maximum discharge 1000 m^3/s, annual water and sediment fluxes 5 km^3 and 9 million tons) is sourced in recently uplifted Angolan highlands (Al-Hajri *et al.*, 2009), where annual rainfall reaches 1400 mm and Paleoproterozoic granitoid and metasedimentary rocks are exposed (De Carvalho *et al.*, 2000). The river flows southward along a structurally-controlled depression hosting the westernmost edge of the fossil Kalahari dunefield (Shaw & Goudie 2002), and finally traverses the Epupa Neoarchean to Mesoproterozoic gneissic basement intruded by one of the largest anorthosite bodies on Earth (dated as ~1.37 Ga; Becker *et al.*, 2006), and eventually the high-grade metasediments and granitoids of the western Kaoko Zone (Gray *et al.*, 2008). The sharp westward turn upstream of this final youthful tract points to recent capture of interior drainage, formerly directed towards the Etosha Pan, by a stream eroding backwards from the coast (Haddon & McCarthy 2005; Goudie & Viles, 2015). Terrigenous deposits blanket most of the shelf seaward of the Cunene mouth, where phosphorite and glauconite occur (Bremner & Willis,1993).

Tributaries of the Cunene drain different geological domains, and thus carry sand with varied composition (Fig. 9). Angolan tributaries draining the Kalahari paleodesert (e.g., Mucope and Caculuvar Rivers; Fig. 6A) carry recycled quartzose sand with extremely poor heavy-mineral suites including mainly zircon with tourmaline, epidote, and minor andalusite, staurolite and rutile. Namibian tributaries draining Neoproterozoic siliciclastic rocks (Nosib Group) carry feldspatho-quartzose sedimentaclastic sand with a very poor epidote-amphibole-zircon suite. Tributaries draining the Cunene igneous complex (e.g., Omuhongo River, Fig. 6B) carry quartzo-feldspathic sand with abundant plutonic rock fragments, twinned plagioclase, and a rich epidote-dominated suite including hornblende and pyroxene. Tributaries draining the Epupa metamorphic basement (e.g., Otjinjange River, Fig. 6D) carry feldspatho-quartzose sand with granitoid and high/very-high-rank metamorphic rock fragments including amphibolite, and a very rich hornblende-dominated suite with epidote and minor sillimanite.

Trunk river sand in Angola is feldspatho-quartzose with K-feldspar > plagioclase, common twinned microcline and a few siltstone and carbonate rock fragments, reflecting extensive recycling of fossil Kalahari dunes. Heavy-mineral suites change from very poor and zircon-dominated upstream, to amphibole-dominated with common epidote, and minor sillimanite, zircon, tourmaline, apatite, garnet, rutile and andalusite at Ruacana Falls. Sand changes markedly in the final tract, and at Epupa Falls it is notably enriched in plagioclase, plutonic, metamorphic (metasandstone, gneiss, amphibolite) and sedimentary (sandstone/sitlstone) rock fragments, and contains a moderately rich amphibole > epidote suite including kaersutite and oxy-hornblende, green to brown clynopyroxene, hypersthene, and rare olivine (Fig. 6C). At the mouth, Cunene sand reveals extensive mixing with far-travelled sand wind-blown from the coast, as indicated by less plagioclase and more garnet, staurolite and clinopyroxene (Fig. 7A).

U-Pb zircon ages in Cunene sand at Ruacana Falls are characterized by Eburnean (46% of ages between 1710 and 1982 Ma) and mid-Mesoproterozoic clusters (24% of ages between 1240 and 1428 Ma). At Epupa Falls downstream they change drastically, and display a broad, slightly asymmetrical peak between 1 and 2 Ga, centered at ~1.38 Ga (Fig. 10). Zircon-age spectra change drastically again and become trimodal at the mouth, with peaks between 460 and 629 Ma (18%), 981 and 1086 Ma (22%), and 1758 and 1831 Ma (18%).

Moçamedes Desert sand

The ~3500 km^2 Moçamedes (Baia dos Tigres) dunefield, characterized by the transition from larger crescentic dunes to smaller dunes and linear ridges inland, is sharply delimited to the north by the Curoca River (Fig. 4; Torquato, 1970). A field of coppice dunes (in Arabic *nabkhah*, "sandy hillocks with pointed top") occurs between Subida Grande and Namibe (Fig. 2E). Dune and beach sands between the Cunene mouth (Fig. 7B) and Subida Grande (Fig. 7C) are feldspatho-quartzose with lathwork volcanic rock fragments and moderately poor to extremely rich garnet-clinopyroxene-epidote-amphibole suites including hypersthene, staurolite, and minor tourmaline, zircon, apatite and titanite.

Multimodal U/Pb age spectra of detrital zircons show prominent Damara (29% of ages between 446 and 685 Ma) and Namaqua peaks (26% of ages between 898 and 1129 Ma), Eburnean (16% of ages between 1.6 and 2.1 Ga, peak around 1.74 Ga) and mid-Mesoproterozoic clusters (14% of ages between 1164 and 1413 Ma, peaks around 1.20 and 1.36 Ga), minor Early Cretaceous (ages between 120 and 132 Ma) and Permo-Triassic peaks (ages between 238 and 278 Ma), and a Neoarchean scatter (Fig. 11). Chemical composition is virtually identical to that of Skeleton Coast dunes, with greater intersample variability controlled by hydrodynamic effects (as discussed below). More phosphorous indicates greater abundance of phosphate grains, largely of organic origin. More Mn, Y, and HREE relatively to Coastal Namib sand reflects progressive concentration of garnet northward along the littoral cell. Petrographic, mineralogical, geochemical, and geochronological data concur to indicate that Moçamedes sands are principally derived from the Orange mouth, with subordinate contribution from the Cunene River (as quantified below).

The same feldspatho-quartzose composition with equally abundant lathwork volcanic grains and clinopyroxene characterizes the Curoca River upstream of the mouth, indicating overwhelming contribution by windblown sand flushed in the lower course. Very rich heavy-mineral suites do not include additional amphibole or epidote derived from basement rocks exposed in the upper catchment, and U-Pb zircon-age spectra are hardly distinguished from Moçamedes Desert sand (Fig 9).

From Namibe to Lucira

Beach sand composition changes abruptly at Namibe (Fig. 7D), where feldspar-rich sand with plutonic, gneissic and amphibolite grains yields a very rich amphibole-epidote suite including clinopyroxene, hypersthene, minor enstatite, olivine, garnet, and rare staurolite. Amphibole and epidote grains are notably angular, and pink zircon grains commonly strongly metamictic, suggesting very prolonged radiometric decay. The bimodal zircon-age spectrum includes Eburnean (44% of ages between 1727 and 1804 Ma) and mid-Mesoproterozoic clusters (32% of ages between 1310 and 1395 Ma; Fig 9).

North of Namibe, the Bero and Giraul Rivers carry feldspar-rich plutoniclastic-gneissiclastic sand with a moderately rich amphibole-epidote suite derived from Angolan basement. Clinopyroxene and hypersthene in Bero sand are most probably derived from the Cunene igneous complex drained in the headwaters; Giraul sand contains less amphibole, more epidote, and minor garnet. The few detrital-zircon ages obtained are Mesoproterozoic in Bero sand and dominantly between 1.7 and 2.0 Ga in Giraul sand. Additional clinopyroxene may be derived from Cretaceous volcanic rocks exposed in the lower course of both rivers (Alberti *et al.*, 1992).

Feldspar-rich feldspato-quartzose composition characterizes all beach and river sands farther north, with poor to rich epidote-amphibole suites documenting provenance from basement rocks (Fig. 7E). Mainly brown, subrounded augitic clinopyroxene or zircon associated with garnet, titanite, rutile and apatite occur locally (Mariquita and Chapeu Armado beaches), suggesting subordinate supply from basaltic and siliciclastic rocks of the Namibe Basin exposed close to the coast (Strganac *et al.*, 2014; Gindre-Chanu *et al.*, 2016).

Offshore sediments

Walvis Ridge samples (water depths -399 m and -642 m) are medium silts with a little sand fraction dominated by tests of planktonic and subordinately benthic foraminifers. Coarse-silt-sized siliciclastic detritus, glaucony and phosphate grains are all very minor. The sand fraction in samples collected offshore of the Cunene mouth (water depths from -75 m to -173 m), consisting chiefly of green glaucony to brown-greenish glauco-phosphorite grains and including benthic foraminifers, echinoid fragments and phosphate clasts, increases progressively oceanward and consists virtually entirely of ~2ϕ-sized, subangular to subrounded, deep-green glaucony grains at -551 m depth (fig. 7 in Garzanti *et al.*, 2017). Terrigenous siliciclastic detritus decreases progressively seaward in abundance from ~70% to ~3%, and in size from very fine sand to coarse silt. Heavy-mineral concentration in the > 15 μm fraction remains remarkably constant, and similar to that of Skeleton Coast dune sand at any depth (HMC ~7, tHMC ~6). In all six samples, heavy minerals are mostly clinopyroxene (Appendix Table A5), with subordinate epidote and blue-green amphibole, minor garnet, titanite, apatite, hypersthene, zircon, rutile, and rare tourmaline, staurolite and sillimanite. Platy micas are few (2-5%). Vivianite occurs at depths between -110 m and -551 m offshore of the Cunene mouth; celestite and carbonate grains occur in the shallower Walvis Ridge sample.

The feldspatho-quartzose terrigenous fraction of offshore samples, including a few mafic volcanic grains and a heavy-mineral suite as rich in clinopyroxene as in Skeleton Coast sand, indicates dominant provenance from the Orange mouth (Fig. 12). The notably lower abundance of opaque Fe-Ti-Cr oxides and garnet suggests preferential segregation of ultradense minerals in beach placers, although offshore samples have the same amount of low-density amphibole as Skeleton Coast dunes. Epidote shows a regular relative increase oceanward, from 6±2%tHM in Skeleton Coast sands, to 12±2%tHM in shelfal sediments, to 18±3%tHM in deeper-water sediments (correlation coefficient 0.93). This suggests mixing in increasing proportions with an epidote-rich detrital population possibly supplied by local rivers draining the Kaoko belt (e.g., Hoarusib River). Low amphibole and negligible hypersthene contents rule out contributions from the Cunene River even for the sample collected only ~13 km northwest of the Cunene mouth.

ODP Site 1080 samples were collected at ~0.9 m and ~8.1 m below seafloor at the top of a hemipelagic section consisting of moderately bioturbated, olive-gray, diatom-bearing silty clays with varying abundance of nannofossils and foraminifers. Radiolarians, silicoflagellates, plant remains, particulate organic matter, glauconitic peloids, and authigenic pyrite also occur. The Matuyama/Brunhes boundary and the onset of the Jaramillo Subchron occur at ~9.5 m and ~41 m below seafloor, suggesting that the upper Quaternary record is largely missing (Wefer *et al.*, 1998). Estimated ages for the studied samples range between < 0.4 Ma and ~0.7 Ma. The subordinate feldspar-rich feldspatho-quartzose terrigenous fraction yielded moderately rich to rich heavy-mineral assemblages either clinopyroxene-dominated and virtually identical to MARUM samples collected on the Walvis Ridge and offshore of the Cunene mouth, indicating provenance mostly from the Orange River (younger sample), or including clinopyroxene, epidote, amphibole and garnet, and comparing most closely with beach and dune sands of the southernmost Moçamedes Desert, thus revealing subordinate additional supply from the Cunene River (two older samples). Vivianite and celestite occur.

THE ORIGIN OF GARNET AND MAGNETITE PLACERS

This section documents the marked intersample variability (i.e., difference in mineralogical and chemical composition among diverse beach and dune samples) observed in the Moçamedes Desert, and discusses similarities and differences among placer deposits formed along the Atlantic coast from the Namib Erg to Lucira (Fig. 13). Progressive heavy-mineral enrichment in beach or dune sands is caused principally by selective removal of larger low-density grains, which project higher above the bed and hence have smaller pivoting angles and experience greater flow velocities and drag forces than settling-equivalent smaller and denser grains (Komar, 2007). Beach placers consisting mainly of ultradense minerals are formed during major storms, when large volumes of sand are rapidly removed offshore (Silvester, 1984). Being a most abundant transparent ultradense mineral, garnet is commonly dominant in placer lags, but even garnet is removed when hydrodynamic effects are carried to the extreme. Placer deposits are then dominated by similarly widespread but even denser opaque Fe-Ti-Cr oxides, the most common of which is generally magnetite followed by ilmenite (Garzanti *et al.*, 2009).

The grain density of placer sands, containing minor amounts of quartz and feldspars, exceeds the density of the densest rocks known, ranging between 3.5-4.0 g/cm^3 for garnet placers to ~4.5 g/cm^3 for magnetite placers. "Semi-placers", enriched in dense grains to a lesser extent, are characterized by very rich to extremely rich heavy-mineral concentrations and by grain densities typically between 2.8 and 3.0 g/cm^3. Conversely, heavy minerals are notably depleted by hydrodynamic processes in "anti-placers", the grain density of which is thus significantly lower than akin deposits and close to the density of quartz (2.65 g/cm^3). "Neutral" sand is defined by the composition that sand would have ideally everywhere in the absence of such selective-entrainment effects.

Spatial trends in the concentration of garnet and Fe-Ti-Cr oxides

Garnet placers occur commonly on beaches of Namibia, and are widespread along the terminal tract of the Orange littoral cell in southern Angola (Fig. 2). This is particularly surprising when considering that garnet concentration is estimated to be only 0.2±0.1% in Orange River and Coastal Namib sands, and even much less in Cunene sand (~0.02%). An additional source of garnet, associated with staurolite, is represented by medium-grade Damara metasediments drained by the Kuiseb (garnet concentration 0.2%), Swakop (0.5±0.2%), Omaruru (0.2%), Ugab (0.1%) and Huab (0.4%) Rivers. Garnet is in fact observed to increase in abundance from the northern part of the Coastal Namib Erg to the beaches of central Namibia, where it commonly represents the most abundant and even dominant transparent heavy mineral. Garnet concentration rises to 0.8±0.3% in Skeleton Coast dunes, which documents a significant increase relative to the mixture of contributing sources and thus a progressive enrichment in the direction of longshore transport. Concentration of opaque Fe-Ti-Cr oxides is broadly constant along the littoral cell, ranging from 0.8±0.5% in Orange sand to 0.93±0.02% in Skeleton Coast dunes, and not much different in sands of the Cunene (0.8%) and Namibian rivers draining the Damara orogen (1±1% for Kuiseb, 0.5±0.5% for Swakop, 0.2% for Omaruru, 0.9±0.4% for Ugab, and 0.1% for Huab).

In our samples from the Moçamedes Desert, garnet increases further to become the most abundant and locally dominant heavy mineral. Concentrations of both garnet and opaque Fe-Ti-Cr oxides vary over two full orders of magnitude, reaching 17% and 20% of dune sand and three times more in beach placers.

Mineralogy of beach placers and semi-placers

Three deep red to black foreshore sands, two from the Moçamedes Desert and one from Bentiaba beach, were analysed (results given in Appendix Table A4). Heavy-mineral concentration ranges from 95 to 99%, with garnet and opaque Fe-Ti-Cr oxides representing 48% and 42% of the Praia do Navio placer, and 32% and 62% of the Vanesinha placer, respectively. Torquato (1970) reported high concentration of garnet (42%) and opaque Fe-Ti-Cr oxides (21%) from a beach placer at Praia Amelia (~5 km east of Namibe). Zircon, clinopyroxene, staurolite, epidote, rutile, titanite, hypersthene, monazite, and amphibole represent together 6% of the sample, quartz < 2%, and feldspar < 1%. Detrital garnets resulted to be all pyralspites, mostly almandine-pyrope, some almandine, a few spessartine, and several almandine with either spessartine or both pyrope and spessartine molecule. On classical ternary plots, compositions overlap widely those of garnets in Skeleton Coast dunes, confirming common, long-distance provenance from the south (dataset and plots shown in Appendix Table A6 and Figure A1).

Opaque Fe-Ti-Cr oxides make up 89% of the Bentiaba placer (Fig. 3B), where garnet is rare. Zircon and epidote, together with amphibole, monazite, rutile, and titanite represent 7% of the sample. Quartz and feldspar are ≤ 1% each.

Grain density measured with a hydrostatic balance (method described in Garzanti *et al.*, 2012b, results shown in Appendix Table A7) is 4.17±0.05 g/cm^3 for the Praia do Navio garnet-magnetite placer, 4.40±0.01 g/cm^3 for the Vanesinha magnetite-garnet placer, and 4.61±0.04 g/cm^3 for the Bentiaba magnetite placer. In the northern Moçamedes Desert, grain density increases from 2.67±0.01 g/cm^3 in beach sand slightly depleted in heavy minerals (Fig. 2C), to 2.78 g/cm^3 in sand collected on beach berms enriched in heavy minerals (Fig. 2A,B), and to 2.82±0.01 and 3.26±0.01 g/cm^3 in eolian sands collected on dune crests (Fig. 5C,D). North of Namibe, approximately neutral river and beach sands have a grain density of ~2.67 g/cm^3 (Figs. 3C$_1$, 7E, and 7E$_1$), increasing to 2.77±0.03 g/cm^3 in the Inamangando outer berm semi-placer notably enriched in Fe-Ti-Cr oxides (Figs. 3C$_4$ and 7E$_2$).

Geochemistry of beach placers and semi-placers

Beach placers in the Moçamedes Desert and north of Namibe display different patterns of enrichment in chemical elements hosted in dense and ultradense minerals, reflecting different sediment provenance (Fig. 14). Relative to neutral beach sand, Moçamedes beach placers are enriched by up to two orders of magnitude in Zr and Hf, by factors of 40-60 in Ti, Ta, and Mn, of 20-30 in Th, U, V, Fe, and Sn, and of 10-15 in Sc and Co. Cr and LREE are enriched by less than one order in magnitude, whereas enrichment in HREE ramps up with increasing atomic weight from ≤ 10 times for Gd to ~40 times for Lu. The Eu anomaly ranges between 0.23 and 0.32. REE patterns, similar to those displayed by Coastal Namib beach placers (Fig. 14A), reflect the progressive enrichment principally in garnet and subordinately in zircon, epidote, titanite, Fe-Ti-Cr oxides, and apatite (Fig. 14C). Markedly negative loss on ignition reflects strong concentration of magnetite.

The Bentiaba beach placer is enriched by more than two orders of magnitude in Th and LREE, by factors up to 80 in Zr and Hf, up to 50-70 in U, Ti, Nb, and Fe, up to 40-50 in V, Ta, and Cr, up to 30-40 in Mn, up to ~10-15 in Co, Sn, and P, and up to 5-10 in Sc, W, Ni, and Pb. Enrichment in HREE steps down with increasing atomic weight from ~90 times for Gd to ~60 times for Lu (Fig. 14B). The Eu anomaly is 0.21. The REE pattern is controlled principally by monazite and epidote, and subordinately by titanite, Fe-Ti-Cr oxides, and zircon (Fig. 14D). Very markedly negative loss on ignition reflects extreme concentration of magnetite.

The amount of rare ultradense minerals hosting large amounts of specific trace elements (e.g. Zr and Hf in zircon, LREE and Th in monazite) can be calculated independently from chemical data (approach and results illustrated in Appendix A2). Beaches and dunes in the Skeleton Coast and Moçamedes Desert are estimated to contain ~0.04% zircon, more than sands of the Orange River (~0.02%), of Coastal Namib beaches and dunes (0.01-0.03%), and of rivers draining the Damara orogen in central Namibia (~0.02%), supporting progressive northward concentration of ultradense minerals in coastal sediments of the Orange littoral cell. Zircon concentration is estimated to reach ~1.5% in Coastal Namib and Bentiaba placers and ~2.9% in Moçamedes placers, monazite ~0.03% in Coastal Namib placers, ~0.05% in Moçamedes placers, and 0.7% in the Bentiaba placer.

PROVENANCE OF MOÇAMEDES DESERT SAND

Moçamedes Desert sand is largely derived long-distance from the Orange mouth, after an ultralong littoral transport exceeding 1500 km. Sand sources other than the Orange River are present in central Namibia, the most significant of which being the Swakop River, estimated to contribute 20±3% of the sand accumulated in the Skeleton Coast dunefield of northern Namibia (Garzanti *et al.*, 2014). Moçamedes dunes and beaches contain more metamorphic rock fragments, epidote and amphibole, and less clinopyroxene than Skeleton Coast dunes. Additional supply from the permanent Cunene River, not identified previously owing to limited data, is thus significant and it is quantified tentatively here by forward mixing models based on integrated bulk-petrography and heavy-mineral datasets (mathematical approach illustrated in Appendix A1). Problems in the calculation are caused by the great intersample compositional variability of dune and beach sands, by mixing with far travelled wind-blown sand in the terminal tract of the Cunene River, and by potential additional contribution from the Hoarusib River in northern Namibia.

As a first step, a robust estimate of the composition of Moçamedes Desert sand is obtained by averaging the observed composition of our 14 beach and dune samples corrected by using the *provenance* package of Vermeesch *et al.* (2016) to a grain density of 2.70 g/cm^3, close to that estimated for both Skeleton Coast Erg (SRD 2.71±0.02 g/cm^3) and Cunene sands (SRD 2.69). The composition thus obtained was compared mathematically with three contributing end-members, represented by Cunene sand at Epupa Falls, Skeleton Coast Erg sand (proxy for longshore drifting sand), and Hoarusib River sand (also proxy for central and western zones of the Kaoko belt drained by the Cunene River between Epupa Falls and the edge of the Cunene Erg). The simple forward mixing model thus constructed suggests that Moçamedes Desert sand is derived ~74% from longshore drift, ~18% from the Cunene River upstream of Epupa Falls, and ~8% from the Hoarusib River and/or Kaoko belt rocks drained in the terminal tract of the Cunene. Cunene sand at the river mouth is calculated to be derived ~64% from the Cunene upstream of Epupa Falls, ≥ 24% from eolian sand of the Cunene Erg, and ≤ 12% from the Kaoko Belt drained in the terminal tract.

Diverse trials performed with slightly different end members (e.g., determined as the mean, weighted-mean, or median composition of all replicate samples, or of selected replicate samples only), or with a partial set of parameters (e.g., petrographic or heavy minerals only), suggest that long-distance littoral drift contributes between 65% and 80% of Moçamedes sand. If long-distance littoral drift is derived 20±3% from the Swakop and the rest from the Orange, then Moçamedes Desert sand is derived 58±7% from the Orange, 15±3% from the Swakop and other rivers draining the inland branch of the Damara Orogen in central Namibia, 20-25% from the Cunene River upstream of Epupa Falls, and ≤ 5% from the Hoarusib River. Between half and two-thirds of Moçamedes Desert sand is derived ultralong-distance from the Orange River, only between a fifth and a fourth from the Cunene River.

THE END OF THE ORANGE SAND HIGHWAY

Northward littoral drift from the Orange mouth represents the major source of sand along the hyperarid Atlantic coast to as far as southern Angola. Beaches at Curoca mouth and Subida Grande have the same petrographic composition and heavy-mineral suites as Moçamedes Desert sand, indicating that littoral drift continues north of Tombua. Sand supply from the Curoca River, which flows along the northeastern edge of the Moçamedes Desert where it is choked by eolian sand blown from the south, is undetected. The garnet placer reported by Torquato (1970) at Praia Amelia represents the northernmost testimony of the Orange littoral cell, which terminates abruptly at 15°12'S (Fig. 15).

Beach sand collected at Namibe only ~5 km east of Praia Amelia has radically different composition. Abundant angular amphibole and commonly metamictic zircon grains yielding ages not younger than 1.3 Ga reveal dominant local contribution from the Bero River. Feldspar-rich sands with epidote-amphibole heavy-mineral suites and unimodal zircon-age spectra with Eburnean peak all along the coast north of Namibe indicate that sediment is not derived alongshore from the south, but contributed from rivers draining basement rocks exposed in adjacent Angolan highlands. The Orange sand trace is thus suddenly lost at Namibe. This is highlighted by the abrupt change in petrographic and mineralogical signatures (Fig. 9) as well as in age-spectra of detrital zircons, indicating bimodal provenance from crystalline rocks of the Namaqua and Damara belts in the south and from the Paleoproterozoic Angola Block in the north (Fig. 11).

Speculations on travel time and long-term coastal evolution

The average amount of time needed for sand to cover the entire distance from the Orange mouth to Namibe is hard to constrain even roughly. With a constant longshore velocity of 1 mm/s (e.g., Komar, 1977), without any pause or detour, a single sand grain could theoretically complete the Orange sand highway in 57 years only. With a typical alongshore displacement velocity of an accretion/erosion wave, estimated to range between 0.5 and 4 km/a (Inman & Jenkins, 2005), the minimum time required would range between 3600 and 450 years. On the other extreme, a rough extrapolation of the residence time in the ~600 km-long coast of the Namib Erg, assessed from cosmogenic nuclides to be of at least one million years (Vermeesch *et al.*, 2010), would give a figure of at least three million years. A travel time plausibly longer than Milankovian frequencies would involve complex eustatically controlled sand cycling from the littoral to the eolian environment and back, which occurred repeatedly during the Pleistocene (Bluck *et al.*, 2007; Compton & Wiltshire, 2009).

As documented by the Tsondab Sandstone, which underlies most of the modern Namib Erg and represents its Miocene predecessor characterized by impressively similar sedimentological and mineralogical features (Ward, 1988; Besler, 1996; Kocurek *et al.*, 1999), northward littoral sand drift from the Orange mouth was well established by the middle Miocene, and has been maintained for the last 15 Ma at least (Lancaster, 2014). Swell-driven longshore dispersal may have originated much earlier, in Eocene or possibly Late Cretaceous times (Bluck *et al.*, 2007), and might even have persisted since the Albian early opening of the South Atlantic (Quesne *et al.*, 2009).

Coastal dunefields of Namibia and southern Angola cover an area of ~51,000 km^2 overall (Lancaster, 2014), and host a total volume of sand between 1100 and 1600 km^3 (773-1020 km^3 in the Namib Erg; Bullard *et al.*, 2011), more than 90% of which (i.e., 1000-1500 km^3) derived from the Orange River. Let us assume a northward longshore sand flux between 10^5 and 10^6 m^3/a (i.e., 0.27 - 2.7 10^6 t/a), which appears as a reasonable range considering both net longshore transport rates in South Africa (Schoonees, 2000) and long-term total (mud + sand) Orange sediment flux (estimated at 11±2 10^6 t/a from cosmogenic measurements by Vermeesch *et al.*, 2010). If littoral drift had continued regularly for 15 Ma, then the total amount of sand displaced along the littoral highway would range between 1500 and 15,000 km^3. Orange contribution to modern coastal deserts matches the lower figure, whereas the higher one is much too high even if the volumes of sand stored in paleodunes of the Tsondab Sandstone (maximum thickness 220 m; Ward, 1988) is taken into account. The volume loss of Orange-derived sand to the deep sea through time, presumably enhanced during Pleistocene lowstands, may thus amount to several thousands of km^3. A direct evidence that a significant fraction of northward drifting sand is lost in deep waters offshore even during the present highstand stage is given by the mineralogy of sediments deposited recently in the deep sea from the Walvis Ridge to north of the Cunene mouth (Fig. 12).

Considering that Orange suspended load was reduced by a factor of at least 5 after the construction of big dams along its course by the end of the 1970s (Rooseboom & Harmse, 1979; Bremner *et al.*, 1990), and that bedload must have decreased even more drastically, the Orange sand highway is bound to be affected profoundly by human-built infrastructures. How soon and to what extent, and whether and when it will be eventually disrupted, it is however hard to establish. Although the existence and persistence in time of ultralong littoral cells is of great relevance for the accuracy of paleogeographic reconstructions, to the best of our knowledge no similar sediment-routing system has been documented from the geological record so far.

Why and how the Orange sand highway ends

Eolian sand transport on land is effectively hampered and eventually blocked by deep river valleys with perennial flow or where floods are sufficiently frequent to flush eolian sand to the sea (Lancaster, 1982). This occurs at the northern edge of all four coastal dunefields of Namibia and southern Angola. The Namib Erg is terminated by the Kuiseb River, and eolian sand transport finally stopped by the Swakop River. The Skeleton Coast Erg is terminated by the Hoarusib River, and eolian sand transport stopped by the Khumib River. The Cunene Erg is terminated by the Cunene River, and the Moçamedes Erg by the Curoca River. Northward sand drift, however, continues undisturbed in the littoral zone, and where the coast takes an appropriate direction a new linear corridor is formed along which sand is blown from the sea to feed the next dunefield inland.

The cause for the termination of the Orange littoral cell is thus to be found offshore rather than on land. Considering that strong northward longshore currents and littoral drift continue all along the Angolan coast to far north of the Congo mouth (Guilcher *et al.*, 1974; Dinis *et al.*, 2016), the abrupt end of the Orange littoral cell at Namibe cannot be ascribed primarily to a change in atmospheric or oceanic circulation associated with the Angola-Benguela front (Fig. 1). A key factor, instead, is the physiography of the shelf (Bremner & Willis, 1993; Rogers & Rau, 2006).

Huge sediment volumes can be transported both along and across the continental shelf, which represents the interface between terrestrial sediment sources and deep-sea sediment sinks. Detrital supply from large rivers is a major driver of shelf-margin growth (Carvajal *et al.*, 2009). Along orthogonal-rifted segments of passive margins characterized by relative tectonic stability and major long-lived river systems (Potter, 1978; Cox, 1989), the distance between the coast and the shelfbreak may grow larger in time, until a wide stretch of shallow, mildly sloped sea-floors swept by swell waves may limit permanent sediment loss offshore and allow littoral transport over even very long distances (Silvester & Mogridge, 1970). Conversely, along dynamically-uplifted or transform-rifted active or passive continental margins the shelf is generally much narrower, and coastal sediments can be conveyed directly to the deep sea wherever a canyon reaches close to shore (Covault & Fildani, 2014). Abrupt termination of littoral cells at canyon heads, where drifting sand is efficiently funneled away from the shoreline and dragged to the deep sea by turbidity currents, is widely documented (e.g., Patsch & Griggs, 2007). The most likely cause for the termination of the ultralong Orange littoral cell in the Namibe oblique rifted-margin segment (Guiraud *et al.*, 2010) is thus the presence of submarine canyons connected with the Curoca and Bero River mouths (Fig. 4). A river valley is able to terminate a littoral cell only where it connects underwater to a submarine canyon across a narrow shelf, thus representing an effective sediment-trapping trench dug all across the continental margin.

Placer formation at the end of the Orange sand highway

It has been stated that "*sea level changes are the prime factor influencing placer mineral concentration processes and the regional distribution and preservation of placer deposits on the modern shelf*" (Kudrass, 2000 p.9). Placer deposits, however, may form during both transgressive and regressive stages, and the relationships with eustatic fluctuations and shelf physiography are complex (Roy, 1999; Dillenburg *et al.*, 2004; Dinis & Soares, 2007). Exploration of the continental shelf worldwide has documented a decrease in heavy-mineral concentration typically by an order of magnitude with water depth (fig. 6 in Kudrass, 1987), and a partitioning of ultradense minerals in beach placers and of slower-settling "more mobile" minerals such as amphiboles or micas offshore (Cascalho & Fradique, 2007). If the littoral zone is sufficiently shallow and wide, then the anti-placer sand fraction selectively entrained seaward and deposited to build an offshore bar during storm events can be dragged again landward by swell waves (Silvester, 1984). The original composition of beach sand is thus restored. Permanent enrichment in ultradense minerals in coastal sediments requires net sediment removal and deposition by storm-surge or turbidity currents in the deep sea beyond the reach of swell waves. Shelf bathymetry and width thus exert a fundamental control not only on the sediment budget of coastal areas but also on the partitioning of detrital minerals between the coast and the deep sea.

In southwestern Africa, the width of the continental shelf reaches 180-200 km offshore of the Orange mouth, ranges between 150 and 100 km offshore Namibia as far as the Walvis Ridge, and it is reduced to 40-45 km in the north as far as Baia dos Tigres. Farther north it decreases rapidly to ~10 km offshore of the northern Moçamedes Desert, and to a few km at most from Tombua to Namibe, where the -150 m isobath lies within 1 km from the coast at the head of the Curoca and

Bero canyons (Fig. 15). Along the coast of Namibia, where the shelf is wide, only subtle trends in mineralogical composition are observed. Gradual loss of platy amphibole relative to equant ultradense garnet (fig.10 in Garzanti *et al.*, 2015b) suggests that a fraction of the sand enriched in slower-settling minerals has been lost to the deep sea along the Orange littoral cell, possibly largely during Pleistocene lowstands. Sediments collected offshore of the Cunene mouth are depleted in ultradense garnet and Fe-Ti-Cr oxides by an order of magnitude, but heavy-mineral concentration remains remarkably constant after correcting for mixing with intrabasinal calcareous, glaucony, and phosphate grains. The order-of-magnitude decrease in heavy minerals in deep-water sediments sampled seaward of the shelf edge is thus ascribed to mixing with intrabasinal grains rather than to hydraulic-sorting effects.

Along the coastal stretch north of Baia dos Tigres, where a well defined scarp connects the continental slope with the abyssal plain, beach and dune sands become markedly enriched in garnet and Fe-Ti-Cr oxides (Fig. 2A,B). The sharp boundary between cream-yellow dunes and dark-red dunes rich in ultradense minerals, running NNE/SSW and intersecting the coast at ~16°23'S as clearly seen in Fig. 5, suggests an abrupt northward decrease in sand availability (Courrech du Pont *et al.*, 2014). Yellow dunes in the southeast are in fact much larger, predominantly transverse, and reach elevations increasing from some tens of meters near the coast to 250-280 m inland, whereas red parabolic dunes to the north occur in a low elevation area with wetlands and are mostly < 10 m-high, indicating limited sand supply (Reffet *et al.*, 2010; Gao *et al.*, 2015). Along the low-altitude, sub-rectilinear costal stretch north of Baia dos Tigres, coarser-grained low-density minerals are selectively entrained offshore during storms and lost in deep waters beyond the narrow shelf, leaving coastal sands strongly depleted in lighter and less dense quartz and feldspars and relatively enriched in darker ultradense minerals (Fig. 5C,D). The formation of garnet-magnetite foreshore placers implies that most of the sand (≥ 98% and ≥ 99% for the Praia do Navio and Vanesinha placers, respectively) has been removed temporarily from the beach and parked offshore. The comparison with the average mineralogy of Moçamedes Desert sand suggests that between half and four/fifths of longshore-drifting sand has been transferred permanently to the deep ocean.

Irreversible sand loss is accentuated in the coastal stretch between Tombua and Namibe (Fig. 2D,E), where the bulk of drifting sand is captured by the Curoca and Bero canyons and the ~1800 km-long Orange sand littoral highway eventually comes to a sudden end (Fig. 15). No major canyon is apparently connected with the Cunene mouth (Fig. 4), possibly because the river used to flow southward to the Etosha paleolake and its lower course is recent, and/or because the mouth is choked by longshore drifting sand.

Along the Atlantic coast of southern Africa there is hardly a place where the shelf is as narrow as in the oblique rifted-margin segment between Namibe and Lucira, where a nearshore positive gravity anomaly suggests the presence of underplated basaltic magma or denudated mantle associated with Moho uplift (Guiraud *et al.*, 2010). Along this coastal stretch, sediment supply is limited because climate is dry and the adjacent Bié-Huila dome is drained by the Cunene River to the south and by the Cuanza and other rivers feeding the Benguela and Cuanza basins to the north. The outer berm commonly undergoes erosion, it is consequently enriched in heavy minerals (Fig. 3C), and foreshore magnetite placers are formed (Fig. 3B), which confirms the close relationship among sediment supply, shelf width, and occurrence of placer deposits. The observed enrichment in Fe-Ti-Cr oxides (Fig. 7E_2) indicates that more than half of the sand originally deposited on the outer berm at the Inamangando river mouth has been entrained temporarily or permanently offshore.

CONCLUSIONS

In the Khoekhoe language used by Nama people, the word Namib designates the "vast place of nothingness" facing the Atlantic Ocean in southwestern Africa. All along this desert stretch of coastal land, from southern Namibia to Namibe in southern Angola, sand derived from as far as basaltic Lesotho highlands via the Orange River is transported for ~1800 km under the persistent action of swell-driven waves. Orange sand, making up 99% of the Coastal Namib Erg and ~80% of the Skeleton Coast Erg, is still predominant in beaches and dunes of the Moçamedes Erg, where contribution from the perennial Cunene River draining the Kalahari paleodesert in the upper course and up to high-grade metamorphic and plutonic rocks in the lower course does not exceed 25%. North of Baia dos Tigres, the continental shelf becomes so narrow that coarser lower-density minerals selectively entrained during higher-energy events are lost offshore, and beach and dune sands onshore are consequently enriched in ultradense garnet and Fe-Ti-Cr oxides. The longest submarine sand highway documented on Earth so far extends for a few tens of kilometers north of the Curoca River and terminates at Namibe, where sand composition and U-Pb age spectra of detrital zircons change abruptly, documenting local fluvial supply from Paleoproterozoic basement exposed in adjacent highlands. The mineralogy and geochemistry of placer lags also changes and their REE patterns, influenced by the concentration of garnet all along the Orange cell, here largely reflect the concentration of monazite.

In southwestern Africa, eolian sand transport on land is blocked repeatedly by river valleys cutting perpendicularly toward the coast, as seen at the northern edges of all four Namib, Skeleton Coast, Cunene, and Moçamedes Ergs. Longshore transport is however unaffected, and continues in shallow waters offshore. Littoral sand drift ends only where the Curoca and Bero river valleys are associated with the head of submarine canyons reaching close enough to shore to form effective sediment-trapping trenches extending all across the narrow rifted margin. Large dams built along the course of the Orange River, with consequent drastic reduction in bedload transport, is bound to affect a sediment conveyor belt established since the Miocene at least and perhaps even since the Cretaceous initial opening of the South Atlantic, and to modify the sediment budget of the Atlantic coast to as far north as southern Angola.

Longshore transport of large sediment volumes in the shallow sea, from the mouth of big rivers over distances of a thousand kilometers and more, occurs on our planet today, and has occurred with all likelihood in the past as well. And yet to the best of our knowledge no similar sediment-routing system has been documented from the geological record so far. The major implications for a successful reconstruction of source-to-sink relationships and continental-scale paleogeographic scenarios based on provenance studies of ancient sedimentary successions, which is of interest not only in academic research but for the identification and quality assessment of hydrocarbon reservoirs as well, remain to be investigated.

ACKNOWLEDGMENTS

Field work was made possible by the logistic support of the University of Katyavala Bwila, Instituto Superior Politécnico da Tundavala, and by the kind help by Manuel Bandeira, Silvano Levy, Margarida Ventura, and Carlos Ribeiro, which we acknowledge warmly. We thank heartily Afonso Sampaio, Armanda Trindade, Edson Baptista, Alcides Pereira, Luciana Ciceri, Fernand Vermeesch, and Dany Kerckhove for collecting additional sand samples from the Cunene River and the Moçamedes Desert, and Claudia Pasquero and Elisa Malinverno for discussion. Laura Borromeo, Francesco Crotti, and Massimiliano Stucchi point-counted, grain-counted, and Raman-counted beach placers, and contributed to the analysis of Raman spectra of detrital garnets and Fe-Ti-Cr oxides. Danilo Controversio, Matteo Sala, and Ethan Petrou helped greatly in grain-density and geochronological analyses. Careful constructive reviews and useful advice kindly provided by Reviewers Michel Guiraud and Gareth Roberts, and by Editors Nick Lancaster and Nigel Mountney, were received gratefully.

SUPPLEMENTARY MATERIAL

Supplementary data associated with this article can be found in the online version, at http://dx.doi.____________. These include information on sampling sites (Table A1) and the complete datasets on bulk-sand petrography (Table A2), heavy minerals (Table A3), placer mineralogy including determination of opaque Fe-Ti-Cr oxides (Table A4), pyroxene grains (Table A5), and garnet grains (Table A6), grain-density (Table A7), bulk-sand geochemistry (Table A8), and zircon-geochronology (Appendix B). The Google-Earth map of sampling sites *Mocamedes.kmz*.is also provided. Table captions are contained in Appendix A, which illustrates the approach followed in the calculation of provenance budgets (A1) and of zircon and monazite concentration based on chemical data (A2).

FIGURE CAPTIONS

Figure 1. Oceanography and sand transport along the west coast of southern Africa. **A)** The 1800 km-long Orange cell of littoral sand drift. Shelf width decreases north of Walvis Ridge and finally tapers out to a few km north of Tombua (Fig. 4). Coastal dunefields: N = Namib; S = Skeleton Coast; C = Cunene; M = Moçamedes. Yellow and green arrows indicate subordinate sediment contribution from the Swakop and Cunene Rivers, respectively. Location of offshore samples is indicated. **B**) Oceanographic features of the Benguela Current large marine ecosystem (after Cochrane *et al.*, 2009). Shelf topography is of particular significance for nearshore circulation and fisheries. **C**) Net sediment transport around world coasts and paths of westerly swell generated in the southern storm belt (after Silvester, 1962 and Davies, 1972). Dotted lines delimit major changes in trends.

Figure 2. Beaches and beach placers in the terminal tract of the Orange littoral cell. Northern Moçamedes Desert: **A, B**) foreshore and backshore sands enriched strongly in garnet and Fe-Ti-Cr oxides at Vanesinha; **C**) prograding beach sand in the process of burying the Vanesa shipwreck south of Tombua; white arrow indicates small erosion scarp at foreshore top. Subida Grande: (**D**) foreshore laminae enriched strongly in Fe-Ti-Cr oxides and garnet in the background; **E**) small backshore coppice dunes (*nabkhah*) enriched patchily in garnet and Fe-Ti-Cr oxides. Localities indicated in Figures 4 and 5.

Figure 3. Beaches and beach placers north of Namibe. **A**) Beach in equilibrium at Baia das Salinas. **B**) Foreshore laminae locally enriched strongly in Fe-Ti-Cr oxides at Bentiaba. **C**) Composite beach at Inamangando (view looking southwest): **C_1**) high inner berm of white sand with the same mineralogy as river sand (Figs. $7E_1$); **C_2**) parallel laminae enriched strongly in Fe-Ti-Cr oxides characterize erosion scarp at foreshore top (**C_3**); **C_4**) low outer berm of darker sand enriched notably

in Fe-Ti-Cr oxides (Fig. 7E$_2$); **C$_5$**) Google Earth image of the composite beach at the Inamangando River mouth, showing lateral continuity in space and persistence in time of the white high inner berm and heavy-mineral-enriched creamy orange low outer berm (boundary indicated by black dotted line). Localities indicated in Figure 4.

Figure 4. Topography of the southern Angola continental margin, showing bathymetry and sample locations. The shelf, still relatively wide offshore of the southern Moçamedes Desert, tapers off at Tombua. The Curoca and Bero mouths are associated with a deep canyon reaching close to shore (Fig. 15). A field of coppice dunes (Fig. 2E) occurs between Subida Grande and Namibe, but farther north the shelfbreak comes even closer to the coast and dunefields disappear. BdS= Baia das Salinas.

Figure 5. Google Earth images of selected sampling sites in the Moçamedes Desert. Changes in dune color largely reflect different hydrodynamic concentration of ultradense garnet and Fe-Ti-Cr oxides, which increases markedly and rather abruptly in the northern part of the desert (north of white dotted line), where shelf width decreases rapidly offshore (Fig. 4). **A)** Small field of yellow barchan dunes south of Tombua Bay, which is delimited by a sand spit. Wave refraction at the point of coastal re-entrant fosters accumulation of drifting sand and incipient formation of a new spit at Ponta do Enfião (fig. 8 in Guilcher *et al.*, 1973); **B)** Deflation of ochre sand in the backshore of Vanesa beach (note small linear dunes formed in the lee of shrubs; arrow points at shipwreck seen in Fig. 2C); **C)** Deflation of dark red sand in the backshore of Vanesinha beach (Fig. 2A,B) with composite red barchan dunes inland; **D)** Coalescent red barchan dunes at Praia do Navio; **E)** Composite yellow transverse dunes at Baia dos Tigres, a toponym seemingly chosen by sailors because concentration of red garnet and black Fe-Ti-Cr oxides makes beaches and dunes look like tiger stripes from the sea; **F)** The Cunene River separates sharply the Cunene Erg in the south from

a deflation area in the north. The direction of swell waves is constantly from the southwest. Blue bar for scale = 500 m.

Figure 6. Petrographic signatures in the Cunene River system. **A**) Pure quartzose recycled sand supplied to the upper course (q = quartz). **B)** Quartzo-feldspathic plutoniclastic sand supplied to the lower course (p = plagioclase; c = clinopyroxene). **C**) Plagioclase-rich feldspatho-quartzose trunk-river sand in the lower course upstream of the coastal Cunene dunefield. **D)** Litho-feldspatho-quartzose metamorphiclastic sand supplied in the terminal tract (a = amphibole). All photos with crossed polars; blue bar for scale = 250 µm.

Figure 7. Changes in sand composition in southern Angola. **A**) River sand at Cunene mouth reveals extensive mixing with dune sand fed from northward littoral drift (q = quartz; a = amphibole; h = hypersthene). **B**) Beach sand at Cunene mouth is mainly derived ultralong-distance from the Orange River. Orange-derived small rounded clinopyroxene (c) contrasts with Cunene-derived oversized angular orthopyroxene (h). **C**) Small rounded clinopyroxene grains and basaltic rock fragments (B) derived from as far as Lesotho highlands at the end of the Orange littoral cell. **D**) Feldspar-rich sand with granitoid rock fragments (G) derived from Angolan basement is supplied via the Bero River to the Namibe beach. **E**) Feldspar-rich feldspatho-quartzose Inamangando River sand; **E_1**) sand with identical composition deposited on the high inner berm at the Inamangando mouth; **E_2**) marked enrichment in opaque and transparent heavy-minerals in the low outer berm. All photos but **E_2** with crossed polars; blue bar for scale = 250 µm.

Figure 8. Sketch geological map showing major tectonic domains and river drainages in southern Africa (compiled after Schlüter, 2008 and other sources cited in text).

Figure 9. Petrography and heavy minerals in sands of southern Angola. Composition of Moçamedes Desert sand is close to Skeleton Coast sand with additional contribution from the

Cunene River. Composition of Cunene sand changes progressively from the upper course largely draining fossil Kalahari dunes to the lower course draining the Cunene igneous complex and Epupa basement before cutting across the coastal dunefield. Very extensive mixing with coastal eolian sand occurs in the final tract of the Curoca River. The Orange littoral cell terminates at Namibe, and beach sand to the north is supplied by local rivers draining Angolan basement with minor recycling of Cretaceous to Miocene strata exposed near the coast. Q = quartz; F = feldspar (KF = K-feldspar; P = plagioclase); L = lithic fragments (Lm = metamorphic; Lv = volcanic; Ls = sedimentary; Lc = carbonate; Lsm = sedimentary + low-rank metasedimentary; Lvm = volcanic + low-rank metavolcanic; Lm* = medium/high-rank metamorphic); HM = heavy minerals; ZTR = zircon + tourmaline + rutile. Both multivariate observations (points) and variables (rays) are displayed in the compositional biplots (Gabriel, 1971). The length of each ray is proportional to the variance of the corresponding element in the data set. If the angle between two rays is close to 0°, 90°, or 180°, then the corresponding elements are directly correlated, uncorrelated, or inversely correlated, respectively.

Figure 10. Downstream changes in U-Pb age spectra of detrital zircons in sands of the Cunene River (age vs. frequencies plotted as Kernel Density Estimates using the *provenance* package of Vermeesch *et al.*, 2016). Paleoproterozoic to Neoarchean zircons are most abundant in the mildly sloped upper course draining fossil Kalahari dunes. Mid-Mesoproterozoic zircons become dominant in the much steeper youthful lower course, where erosion is focused and the river is incising rapidly into the Cunene igneous complex. Damara and Namaqua age peaks appear at the mouth, reflecting extensive mixing with windblown sand mostly derived ultralong-distance from the Orange River.

Figure 11. U-Pb age spectra of detrital zircons in beach, dune and river sands from northern Namibia to southern Angola. The northern termination of the Orange littoral cell at 15°12'S is marked by the abrupt transition from bimodal spectra dominated by Damaran and Namaqua ages

typical of Orange River and coastal Namibia sands to unimodal spectra dominated by Eburnean ages, reflecting provenance of most zircon grains from Paleoproterozoic crystalline rocks of the Angola Block (age vs. frequencies plotted as Kernel Density Estimates using software package *provenance*; Vermeesch *et al.*, 2016). Age spectra of detrital zircons carried by the Cunene and Curoca Rivers at the mouth indicate that, rather than derived from their upstream reaches, they were mainly supplied long-distance from the Orange River and blown from the coast to choke the river valley inland. Nonetheless, significant zircon contribution from the Cunene River upstream of the coastal erg is documented by mid-Mesoproterozoic and late Paleoproterozoic peaks, which are notably larger in Moçamedes beaches and dunes than in Skeleton Coast dunes. Zircon contribution from the Curoca River upstream of the coastal erg is not evident.

Figure 12. Heavy minerals in recent sediments sampled from the Walvis Ridge to offshore of Baia dos Tigres. **A**) Offshore suites compare closely to either Skeleton Coast or Moçamedes Desert sands and differ drastically from those of all river sands from Namibia to Angola, documenting long-distance provenance mostly from the Orange mouth. **B**) Offshore suites tend to be depleted in ultradense minerals (garnet, opaque Fe-Ti-Cr oxides), preferentially retained in coastal sediments. ZTR = zircon + tourmaline + rutile; tHMC = transparent heavy-mineral concentration. In the compositional biplot (Gabriel, 1971), the angle between two rays is close to 0°, 90°, or 180° if the corresponding variables are directly correlated, uncorrelated, or inversely correlated, respectively.

Figure 13. Intersample mineralogical variability of beach and dune sands is controlled by both size-density sorting during selective entrainment (1st principal component) and provenance (2nd principal component). Low-density quartz, feldspars and rock fragments all correlate more and more negatively with denser and denser minerals. Moçamedes sand is richer in garnet, staurolite and pyroxenes, rivers and beaches north of Namibe in epidote and amphibole. HMC = Heavy Mineral Concentration. In the compositional biplot (Gabriel, 1971), the angle between two rays is close to

0°, 90°, or 180° if the corresponding variables are directly correlated, uncorrelated, or inversely correlated, respectively.

Figure 14. Different patterns of intersample chemical variability in coastal sands of southern Angola (elements arranged following the periodic table group by group). In beach placers formed by selective-entrainment processes, Na, K, Rb, Ba, and Si hosted in low-density tectosilicates are depleted progressively, whereas Y, REE, Th, U, Ti, Zr, Hf, V, Nb, Ta, Cr, Mn, Fe, Co, and P hosted in dense and ultradense minerals are enriched, and the Eu anomaly is strongly negative. **A**) Moçamedes and Skeleton Coast sands have similar composition, indicating common long-distance provenance mainly from the Orange River. Moçamedes placers show the same pattern as Coastal Namib placers, with progressive increase in Sc, Y, HREE, and Mn reflecting garnet enrichment (concentrations normalized to averaged analyses of 19 Coastal Namib beach and dune sands after Garzanti *et al.*, 2015b). **B**) Beach placers and semi-placers north of the Orange cell are enriched in LREE and especially Th, indicating monazite concentration, scarcity of garnet, and local provenance from Angolan basement rocks (concentrations normalized to averaged analyses of 8 beach and river sands collected between Namibe and Lucira). Chondrite-normalized REE patterns are controlled principally by the concentration of garnet in Coastal Namib and Moçamedes placer sands (**C**) and by concentration of monazite in placer sand derived from Angolan basement (**D**). REE patterns of heavy minerals after Garzanti *et al.* (2011).

Figure 15. The Orange littoral sand highway terminates abruptly just east of Praia Amelia, where garnet placers occur (Torquato, 1970). Sand dragged by swell waves from the south feeds the subaqueous spit in front of Praia Amelia, but it is funnelled next in the submarine canyon connected to the Bero mouth. The beach in Namibe Bay is supplied by the Bero River.

REFERENCES

Al-Hajri, Y., White, N. and **Fishwick, S.** (2009) Scales of transient convective support beneath Africa. Geology, 37, 883-887.

Alberti, A., Piccirillo, E.M., Bellieni, G., Civetta, L., Comin-Chiaramonti, P. and **Morais, E.A.A.** (1992) Mesozoic acid volcanics from southern Angola: petrology, Sr-Nd isotope characteristics and correlation with acid stratoid volcanic suites of the Paranà basin (southeastern Brazil). European Journal of Mineralogy, 4, 597-604.

Allison, M.A. and **Lee, M.T.** (2004) Sediment exchange between Amazon mudbanks and shore-fringing mangroves in French Guiana. Marine Geology, 208, 169-190.

Andò, S., Vignola, P. and **Garzanti, E.** (2011) Raman counting: a new method to determine provenance of silt Rendiconti Lincei Scienze Fisiche e Naturali, 22, 327-347.

Andò, S. and **Garzanti, E.** (2014) Raman spectroscopy in heavy-mineral studies. Geological Society London, Special Publications, 386, 395-412.

Becker, T., Schreiber, U., Kampunzu, A.B. and **Armstrong, R.** (2006) Mesoproterozoic rocks of Namibia and their plate tectonic setting. Journal of African Earth Sciences, 46, 112-140.

Besler, H. (1996) The Tsondab Sandstone in Namibia and its significance for the Namib erg. South African Journal of Geology, 99, 77-87.

Bluck, B.J.,Ward, J.D.,Cartwright, J. and **Swart, R.** (2007) The Orange River, southern Africa: an extreme example of a wave-dominated sediment dispersal system in the South Atlantic Ocean. Journal of the Geological Society, London 164, 341-351.

Boyd, R., Ruming, K., Goodwin, I., Sandstrom, M. and **Schröder-Adams, C.** (2008) Highstand transport of coastal sand to the deep ocean: a case study from Fraser Island, southeast Australia. Geology, 36, 15-18.

Bremner, J.M. and **Willis J.P.** (1993) Mineralogy and geochemistry of the clay fraction of sediments from the Namibian continental margin and the adjacent hinterland. Marine Geology, 115, 85-116.

Bremner, J.M., Rogers, J. and **Willis, J.P.** (1990) Sedimentological aspects of the 1988 Orange River floods. Transactions of the Royal Society of South Africa, 47, 247-294.

Bullard, J.E., White, K. and **Livingstone, I.** (2011) Morphometric analysis of aeolian bedforms in the Namib Sand Sea using ASTER data. Earth Surface Processes and Landforms, 36, 1534-1549.

Calliari, L.J. and **Toldo, E.E.** (2016) Ocean beaches of Rio Grande do Sul. In: Short, A.D. and Klein, A.H.D.F. (Eds.), Brazilian Beach Systems. Springer, Switzerland, Coastal Research Library, 17, pp. 507-541.

Carvajal, C., Steel, R. and **Petter, A.** (2009) Sediment supply: the main driver of shelf-margin growth. Earth-Science Reviews, 96, 221-248.

Cascalho, J. and **Fradique, C.** (2007) The sources and hydraulic sorting of heavy minerals on the northern Portuguese continental margin. In: Mange, M.A. and Wright, D.T. (Eds.), Heavy minerals in use. Elsevier, Amsterdam, Developments in Sedimentology Series, 58, pp. 75-110.

Cochrane, K.L., Augustyn, C.J., Fairweather, T., Japp, D., Kilongo, K., Iitembu, J., Moroff, N., Roux, J.P., Shannon, L., Van Zyl, B. and **Vaz Velho, F.** (2009) Benguela Current Large Marine Ecosystem—Governance and management for an ecosystem approach to fisheries in the region. Coastal Management, 37, 235-254.

Compton, J.S. and **Wiltshire, J.G.** (2009) Terrigenous sediment export from the western margin of South Africa on glacial to interglacial cycles. Marine Geology, 266, 212-222.

Corbett, I. (1993) The modern and ancient pattern of sandflow through the southern Namib deflation basin. International Association of Sedimentology, Special Publication 16, 45-60.1993

Courrech du Pont, S., Narteau, C. and **Gao, X.** (2014) Two modes for dune orientation. Geology, 42, 743-746.

Covault, J.A. and **Fildani, A.** (2014) Continental shelves as sediment capacitors or conveyors: source-to-sink insights from the tectonically active Oceanside shelf, southern California, USA. In: Chiocci, F.L. and Chivas, A.R. (Eds), Continental shelves of the world: their evolution during the last glacio-eustatic cycle. Geological Society London, Memoir 41, 315-326.

Cox, K.G. (1989) The role of mantle plumes in the development of continental drainage patterns. Nature, 342, 873-877.

Davies, J.L. (1972) Geographical variation in coastal development. Oliver and Boyd, Edinburgh, 204 p.

De Carvalho, H., Tassinari, C., Alves, P.H., Guimarães, F. and **Simões, M.C.** (2000) Geochronological review of the Precambrian in western Angola: links with Brazil. Journal of African Earth Sciences, 31, 383-402.

Dickinson, W.R. (1988) Provenance and sediment dispersal in relation to paleotectonics and paleogeography of sedimentary basins. In: Kleinspehn, K.L. and Paola, C. (Eds.), New perspectives in basin analysis. New York, Springer, pp. 3-25.

Dillenburg, S.R., Tomazelli, L.J., Barboza, E.G. (2004) Barrier evolution and placer formation at Bujuru southern Brazil. Marine Geology, 203, 43-56.

Dinis, P.A. and **Soares, A.F.** (2007) Stable and ultrastable heavy minerals of alluvial to nearshore marine sediments from Central Portugal: facies related trends. Sedimentary Geology, 201, 1-20.

Dinis, P., Huvi, J., Cascalho, J., Garzanti, E., Vermeesch, P. and **Callapez, P. (**2016) Sand-spits systems from Benguela region (SW Angola). An analysis of sediment sources and dispersal from textural and compositional data. Journal of African Earth Sciences, 117, 171-182.

dos Santos, V.F., Short, A.D. and **Mendes, A.C.** (2016) Beaches of the Amazon Coast: Amapá and West Pará. In: Short, A.D. and Klein, A.H.D.F. (Eds.), Brazilian Beach Systems. Springer, Switzerland, Coastal Research Library, 17, pp. 67-93.

Gabriel, K.R. (1971) The biplot graphic display of matrices with application to principal component analysis. Biometrika, 58, 453-467.

Galehouse, J.S. (1971) Point counting. In: Carver, R.E. (Ed.), Procedures in Sedimentary Petrology. Wiley, New York, pp. 385-407.

Gao, X., Narteau, C. and **Rozier, O.** (2015) Development and steady states of transverse dunes: a numerical analysis of dune pattern coarsening and giant dunes. Journal of Geophysical Research: Earth Surface, 120, 2200-2219.

Garzanti, E. (2016) From static to dynamic provenance analysis – Sedimentary petrology upgraded. Sedimentary Geology, 336, 3-13.

Garzanti, E. and **Andò, S.** (2007) Heavy-mineral concentration in modern sands: implications for provenance interpretation. In: Mange, M.A. and Wright, D.T. (Eds.), Heavy minerals in use. Elsevier, Amsterdam, Developments in Sedimentology Series, 58, pp. 517-545.

Garzanti, E. and **Vezzoli, G.** (2003) A classification of metamorphic grains in sands based on their composition and grade. Journal of Sedimentary Research, 73, 830-837.

Garzanti, E., Andò, S. and **Vezzoli, G.** (2009) Grain-size dependence of sediment composition and environmental bias in provenance studies. Earth and Planetary Science Letters, 277, 422-432.

Garzanti, E., Andò, S., France-Lanord, C., Galy, V., Censi, P. and **Vignola, P.** (2011) Mineralogical and chemical variability of fluvial sediments. 2. Suspended-load silt (Ganga-Brahmaputra, Bangladesh). Earth and Planetary Science Letters, 302, 107-120.

Garzanti, E., Andò, S., Vezzoli, G., Lustrino, M., Boni, M. and **Vermeesch, P.** (2012a) Petrology of the Namib sand sea: long-distance transport and compositional variability in the wind-displaced Orange Delta. Earth-Science Reviews, 11, 173-189.

Garzanti, E., Resentini, A., Vezzoli, G., Andò, S., Malusà, M. and **Padoan, M.** (2012b) Forward compositional modelling of Alpine orogenic sediments. Sedimentary Geology, 280, 149-164.

Garzanti, E., Vermeesch, P., Andò, S., Lustrino, M., Padoan, M. and **Vezzoli, G.** (2014) Ultra-long distance littoral transport of Orange sand and provenance of the Skeleton Coast Erg (Namibia). Marine Geology, 357, 25-36.

Garzanti, E., Andó, S., Padoan, M., Vezzoli, G. and **El Kammar, A.** (2015a) The modern Nile sediment system: processes and products. Quaternary Science Reviews, 130, 9-56.

Garzanti, E., Resentini, A., Andò, S., Vezzoli, G. and **Vermeesch, P.** (2015b) Physical controls on sand composition and relative durability of detrital minerals during long-distance littoral and eolian transport (coastal Namibia). Sedimentology, 62, 971-996.

Garzanti, E., Dinis, P., Vermeesch, P., Andò, S., Hahn, A., Huvi, J., Limonta, M., Padoan, M., Resentini, A., Rittner, M. and **Vezzoli, G.** (2017) Dynamic uplift, recycling and weathering control on the petrology of subequatorial passive-margin sands (Angola). Sedimentary Geology, in review.

Gindre-Chanu, L., Perri E., Sharp, I.R., Peacock, D.C.P., Swart, R., Poulsen R., Ferreira, H. and **Machado, V.** (2016) Origin and diagenetic evolution of gypsum and microbialitic carbonates in the Late Sag of the Namibe Basin (SW Angola). Sedimentary Geology, 342, 133-153

Goudie, A. and **Viles, H.** (2015) The North East Kunene Region: The Kunene River, Sand Sea and Yardangs. In: Landscapes and Landforms of Namibia. Springer Netherlands, pp. 55-59.

Gray, D.R., Foster, D.A., Meert, J.G., Goscombe, B.D., Armstrong, R., Trouw, R.A.J. and **Passchier, C.W.** (2008) A Damara Orogen perspective on the assembly of southwestern Gondwana. In: Pankhurst, R.J., Trouw, R.A.J., Brito Neves, B.B. and De Wit, M.J. (Eds.), West Gondwana: pre-Cenozoic correlations across the South Atlantic region. Geological Society of London, Special Publication 294, 257-278.

Griffin, W.L., Powell, W.J., Pearson, N.J. and **O'Reilly, S.Y.** (2008) GLITTER: data reduction software for laser ablation ICP-MS. Laser Ablation-ICP-MS in the earth sciences. Mineralogical association of Canada short course series, 40, 204-207

Guilcher, A. (2010) Angola. In: Bird, E.C.F. (Ed.), Encyclopedia of the world's coastal landforms. Springer, Dordrecht, The Netherlands, pp. 963-967.

Guilcher, A., Medeiros, C.A., Matos, J.E. and **Oliveira, J.T.** (1974) Les restingas (fléches littorales) d'Angola, spécialment celles du sud et du centre. Finisterra, 9, 117-211.

Guiraud, M., Buta-Neto, A. and **Quesne, D.** (2010) Segmentation and differential post-rift uplift at the Angola margin as recorded by the transform-rifted Benguela and oblique-to-orthogonal-rifted Kwanza basins. Marine and Petroleum Geology, 27, 1040-1068.

Haddon, I.G. and **McCarthy, T.S.** (2005) The Mesozoic–Cenozoic interior sag basins of Central Africa: the Late-Cretaceous–Cenozoic Kalahari and Okavango basins. Journal of African Earth Sciences, 43, 316-333.

Hardman-Mountford, N.J., Richardson, A.J., Agenbag, J.J., Hagen, E., Nykjaer, L., Shillington, F.A. and **Villacastin, C.** (2003) Ocean climate of the South East Atlantic observed from satellite data and wind models. Prog. Oceanogr., 59, 181-221.

Hay, W.W. (1998) Detrital sediment fluxes from continents to oceans. Chemical Geology, 145, 287-323.

Ingersoll, R.V., Bullard, T.F., Ford, R.L., Grimm, J.P., Pickle, J.D. and **Sares, S.W.** (1984) The effect of grain size on detrital modes: a test of the Gazzi-Dickinson point-counting method. Journal of Sedimentary Petrology, 54, 103-116.

Ingersoll, R.V., Dickinson, W.R. and **Graham, S.A.** (2003) Remnant–ocean submarine fans: largest sedimentary systems on Earth. In: Chan, M.A. and Archer, A.W. (Eds.), Extreme depositional environments: mega end members in geologic time. Geological Society of America, Special Paper 370, pp. 191-208.

Inman, D.L. and **Jenkins, S.A.** (1984) The Nile littoral cell and man's impact on the coastal zone of the southeastern Mediterranean. Scripps Institution of Oceanography, Reference Series, 31, 1-43.

Inman, D.L. and **Jenkins, S.A.** (2005) Accretion and erosion waves on beaches. In: Encyclopedia of Coastal Science, Schwartz, M., (Ed.), Kluwer, Dordrecht, The Netherlands, 11 p.

Jacobson, P.J., Jacobson, K.M. and **Seely, M.K.** (1995) Ephemeral rivers and their catchments: sustaining people and development in western Namibia. Desert Research Foundation of Namibia, Windhoek, 160 pp.

Kaminsky, G.M., Ruggiero, P., Buijsman, M.C., McCandless, D. and **Gelfenbaum, G.** (2010) Historical evolution of the Columbia River littoral cell. Marine Geology, 273, 96-126.

Kirst, G.J., Schneider, R.R., Muller, P.J., von Storch, I. and **Wefer, G.** (1999) Late Quaternary Temperature Variability in the Benguela Current System derived from alkenones. Quaternary Research, 52, 92-103.

Kocurek, G., Lancaster, N., Carr, M. and **Frank, A.** (1999) Tertiary Tsondab Sandstone Formation: preliminary bedform reconstruction and comparison to modern Namib sand sea dunes. Journal of African Earth Sciences, 29, 629-642.

Komar, P.D. (1977) Selective longshore transport rates of different grain-size fractions within a beach. Journal of Sedimentary Research, 47, 1444-1453.

Komar, P.D. (2007) The entrainment, transport and sorting of heavy minerals by waves and currents In: Mange, M.A. and Wright, D.T. (Eds.), Heavy minerals in use. Elsevier, Amsterdam, Developments in Sedimentology Series, 58, pp. 3-48.

Kudrass, H.R. (1987) Sedimentary models to estimate the heavy-mineral potential of shelf sediments. In: Teleki, P.G., Dobson, M.R., Moore, J.R. and von Stackelberg, U. (Eds.), Marine minerals: advances in research and resource assessment. Springer, The Netherlands, pp. 39-56.

Kudrass, H.R. (2000) Marine placer deposits and sea-level changes. In: Cronan, D.S. (Ed.), Handbook of marine mineral deposits. CRC Press, Boca Raton, Florida, pp. 3-26.

Jury, M. (2010) Climate and weather factors modulating river flows in southern Angola. International Journal of Climatology, 30, 901-908.

Lancaster, N. (1982) Dunes on the Skeleton Coast, Namibia (South West Africa): geomorphology and grain size relationships. Earth Surface Processes and Landforms, 7, 575-587.

Lancaster, N. (2014) Dune systems of the Namib Desert – a spatial and temporal perspective. Transactions of the Royal Society of South Africa, 69, 133-137.

Lass, H.U., Schmidt, M., Mohrholz, V. and **Nausch, G.** (2000) Hydrographic and current measurements in the area of the Angola-Benguela Front. Journal of Physical Oceanography, 30, 2589-2609.

Manhique, A.J., Reason, C.J.C., Silinto, B., Zucula, J., Raiva, I., Congolo, F. and **Mavume, A.F.** (2015) Extreme rainfall and floods in southern Africa in January 2013 and associated circulation patterns. Natural Hazards, 77, 679-691.

Meeuwis, J.M. and **Lutjeharms, J.R.E.** (1990) Surface thermal characteristics of the Angola-Benguela front. South African Journal of Marine Science, 9, 261-279.

Milliman. J.D. and **Farnsworth, K.L.** (2011) River discharge to the coastal ocean. A global synthesis. Cambridge University Press, New York, 384 p.

Patsch, K. and **Griggs, G.** (2007) Development of sand budgets for California's major littoral cells. Institute of Marine Sciences, University of California, Santa Cruz, 115 p..

Peel, M.C., Finlayson, B.L. and **McMahon, T.A.** (2007) Updated world map of the Koppen-Geiger climate classification. Hydro. Earth Syst. Sci., 11, 1633-1644.

Potter, P.E. (1978) Significance and origin of big rivers. The Journal of Geology, 86, 13-33.

Quesne, D., Buta-Neto, A., Benard, D. and **Guiraud, M.** (2009) Distribuition of Albian clastic deposits in the Benguela basin (Angola): evidence of a Benguela paleocorrent? Bulletin de la Société Géologique de France, 180, 117-129.

Reffet, E., Courrech du Pont, S., Hersen, P. and **Douady, S.** (2010) Formation and stability of transverse and longitudinal sand dunes. Geology, 38, 491-494.

Rogers, J. (1977) Sedimentation on the continental margin off the Orange River and the Namib desert. Geology Survey/University of Cape Town Marine Geosciences Group Bulletin, 7, 1-162.

Rogers, J. and **Bremner, J.M.** (1991) The Benguela ecosystem. VII: Marine-geological aspects. In: Barnes, M. (Ed.), Oceanography and marine biology. Aberdeen University Press, Oceanography and Marine Biology - An Annual Review, 29, 1-85.

Rogers, J. and **Rau, A.J.** (2006) Superficial sediments of the wave-dominated Orange River delta and the adjacent continental margin off southwestern Africa. African Journal of Marine Sciences, 28, 511-524.

Rooseboom, A. and **Harmse, H.J. von M.** (1979) Changes in sediment load of the Orange River during the period 1929–1969. Hydrology of Areas of Low Precipitation, International Association of Hydrological Sciences Publication 128, pp. 459-479.

Rouault, M., Illig, S., Bartholomae, C., Reason, C.J.C. and **Bentamy, A.** (2007) Propagation and origin of warm anomalies in the Angola Benguela upwelling system in 2001. Journal of Marine Systems, 68, 473-488.

Roy, P.S. (1999) Heavy mineral beach placers in southeastern Australia; their nature and genesis. Economic Geology, 94, 567-588.

Ruggiero, P., Kaminsky, G.M., Gelfenbaum, G. and **Voigt, B.** (2005) Seasonal to interannual morphodynamics along a high-energy dissipative littoral cell. Journal of Coastal Research, 21, 553-578.

Schoonees, J.S. (2000) Annual variation in the net longshore sediment transport rate. Coastal Engineering, 40, 141-160.

Schlüter, T. (2008) Geological Atlas of Africa. Springer, Heidelberg, 307 p.

Schulz, H.D., Beese, D., Breitzke, M., Brück, L., Brügger, B., Dahmke, A., Dehning, K., Diekamp, V., Dünner, B., Ehrhardt, I., Gerlach, H., Giese, M., Glud, R., Gumprecht, R., Gundersen, J., Henning, R., Hinrichs, S., Petermann, H., Richter, M., Sagemann, J., Schmidt, W., Schneider, R., Scholz, M., Segl, M., Werner, U. and **Zabel, M**. (1992) Bericht und erste Ergebnisse über die Meteor-Fahrt M20/2, Abidjan-Dakar, 27.12.1991-3.2.1992. Berichte aus dem Fachbereich Geowissenschaften der Universität Bremen, 025. Department of Geosciences, Bremen University.

Scott, R.A., Smyth, H.R., Morton, A.C. and **Richardson, N.** (2014) Sediment Provenance Studies in Hydrocarbon Exploration and Production. Geological Society London, Special Publications, 386, 420 p.

Shannon, L.V. and **Nelson, G.** (1996) The Benguela: large scale features and processes and system variability. In: Wefer, W.H.B.G., Siedler, G. and Webb, D. (Eds.), The South Atlantic: present and past circulation. Springer, Berlin, pp. 163-210.

Shannon, L.V., Boyd, A.J., Brundrit, G.B. and **Taunton-Clark, J.** (1986) On the existence of an El Niño-type phenomenon in the Benguela system. Journal of Marine Research, 44, 495-520.

Shaw, A. and **Goudie, A.S.** (2002) Geomorphological evidence for the extension of the Mega-Kalahari into south-central Angola. South African Geographical Journal, 84, 182-194.

Silvester, R. (1962) Sediment movement around the coastlines of the world. Proceedings of the Institution of Civil Engineers, Paper 14, 289-315.

Silvester, R. (1984) Fluctuations in littoral drift. American Society of Civil Engineers, Proceedings of the 19th Conference on Coastal Engineering, Houston, Texas, chapter 88, 1291-1305.

Silvester, R. and **Mogridge, G.R.** (1970) Reach of waves to the bed of the continental shelf. American Society of Civil Engineers, Proceedings of 12th Conference on Coastal Engineering, Washington, D.C., chapter 40, 651-667.

Spaggiari, R.I., Bluck, B.J. and **Ward, J.D.** (2006) Characteristics of diamondiferous Plio-Pleistocene littoral deposits within the palaeo-Orange River mouth, Namibia. Ore Geology Reviews, 28, 475-492.

Strganac, C., Salminen, J., Jacobs, L.L., Polcyn, M.J., Ferguson, K.M., Mateus, O., Schulp, A.S., Morais, M.L., Tavares; T. da S. and **Gonçalves, A.O.** (2014) Carbon isotope stratigraphy, magnetostratigraphy, and 40Ar/39Ar age of the Cretaceous South Atlantic coast, Namibe Basin, Angola. Journal of African Earth Sciences, 99, 452-462.

Torquato, J.R. (1970) Origin and evolution of the Moçamedes desert (Angola). Boletim do Instituo de Investigaçao cientifica de Angola, 7, 29-38.

Ward, J.D. (1988) Eolian, fluvial and pan (playa) facies of the Tertiary Tsondab Sandstone Formation in the central Namib desert, Namibia. Sedimentary Geology, 55, 143-162.

Vermeesch, P., Fenton, C.R., Kober, F., Wiggs, G.F.S., Bristow, C.S. and **Xu, S.** (2010) Sand residence times of one million years in the Namib Sand Sea from cosmogenic nuclides. Nature Geosciences, 3, 862-865.

Vermeesch, P., Resentini, A. and **Garzanti, E.** (2016) An R package for statistical provenance analysis. Sedimentary Geology, 336, 14-25.

Vermeesch, P., Rittner, M. and **Garzanti, E.** (2017) QEMSCAN+LA-ICP-MS: a ‘big data’ generator for sedimentary provenance analysis. Geophysical Research Abstracts, EGU General Assembly, 19, EGU2017-17171-1.

Wefer, G., Bleil, U., Müller, P.J., Schulz, H.D., Berger, W.H., Brathauer, U., Brück, L., Dahmke, A., Dehning, K., Durate-Morais, M.L., Fürsich, F., Hinrichs, S., Klockgeter, K., Kölling, A., Kothe, C., Makaya, J.F., Oberhänsli, H., Oschmann, W., Posny, J., Rostek, F., Schmidt, H., Schneider, R.R., Segl, M., Sobiesiak, M., Soltwedel, T. and **Spieß, V**. (1988) Bericht über die Meteor-Fahrt M6-6, Libreville - Las Palmas, 18.2.1988 - 23.3.1988. Berichte aus dem Fachbereich Geowissenschaften der Universität Bremen, 003. Department of Geosciences, Bremen University.

Wefer, G., Berger, W.H., Richter, C. and Shipboard Scientific Party (1998) Proceedings of the Ocean Drilling Program, Initial Reports, Vol. 175, 8. Site 1080, 201-221.

Zuffa, G.G., Normark, W.R., Serra, F. and **Brunner, C.A.** (2000) Turbidite megabeds in an oceanic rift valley recording Jökulhlaups of Late Pleistocene glacial lakes of the western United States. The Journal of Geology, 108, 253-274.

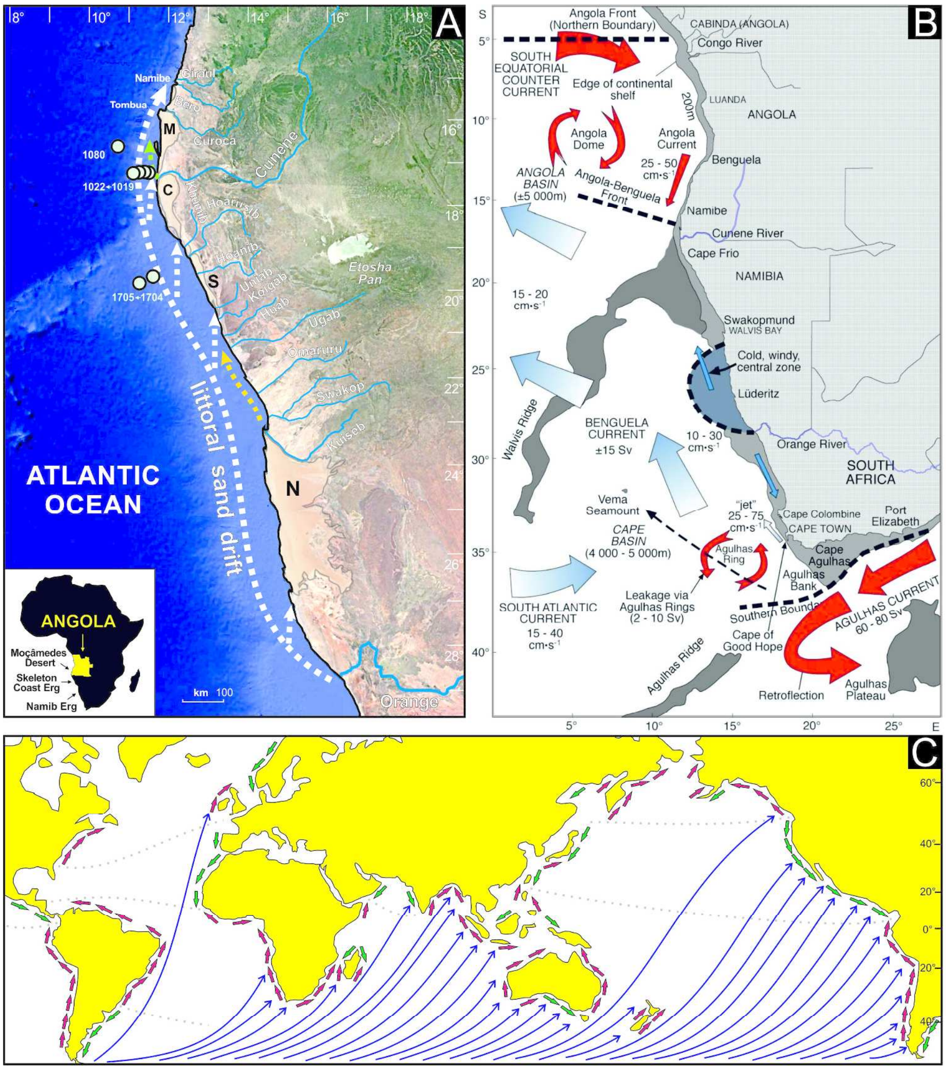

Figure 1 Moçamedes

Figure 1. Oceanography and sand transport along the west coast of southern Africa. A) The 1800 km-long Orange cell of littoral sand drift. Shelf width decreases north of Walvis Ridge and finally tapers out to a few km north of Tombua (Fig. 4). Coastal dunefields: N = Namib; S = Skeleton Coast; C = Cunene; M = Moçamedes. Yellow and green arrows indicate subordinate sediment contribution from the Swakop and Cunene Rivers, respectively. Location of offshore samples is indicated. B) Oceanographic features of the Benguela Current large marine ecosystem (after Cochrane et al., 2009). Shelf topography is of particular significance for nearshore circulation and fisheries. C) Net sediment transport around world coasts and paths of westerly swell generated in the southern storm belt (after Silvester, 1962 and Davies, 1972). Dotted lines delimit major changes in trends.
Fig. 1
236x269mm (300 x 300 DPI)

Figure 2 Moçamedes

Figure 2. Beaches and beach placers in the terminal tract of the Orange littoral cell. Northern Moçamedes Desert: A, B) foreshore and backshore sands enriched strongly in garnet and Fe-Ti-Cr oxides at Vanesinha; C) prograding beach sand in the process of burying the Vanesa shipwreck south of Tombua; white arrow indicates small erosion scarp at foreshore top. Subida Grande: (D) foreshore laminae enriched strongly in Fe-Ti-Cr oxides and garnet in the background; E) small backshore coppice dunes (nabkhah) enriched patchily in garnet and Fe-Ti-Cr oxides. Localities indicated in Figures 4 and 5.

Fig. 2
159x197mm (300 x 300 DPI)

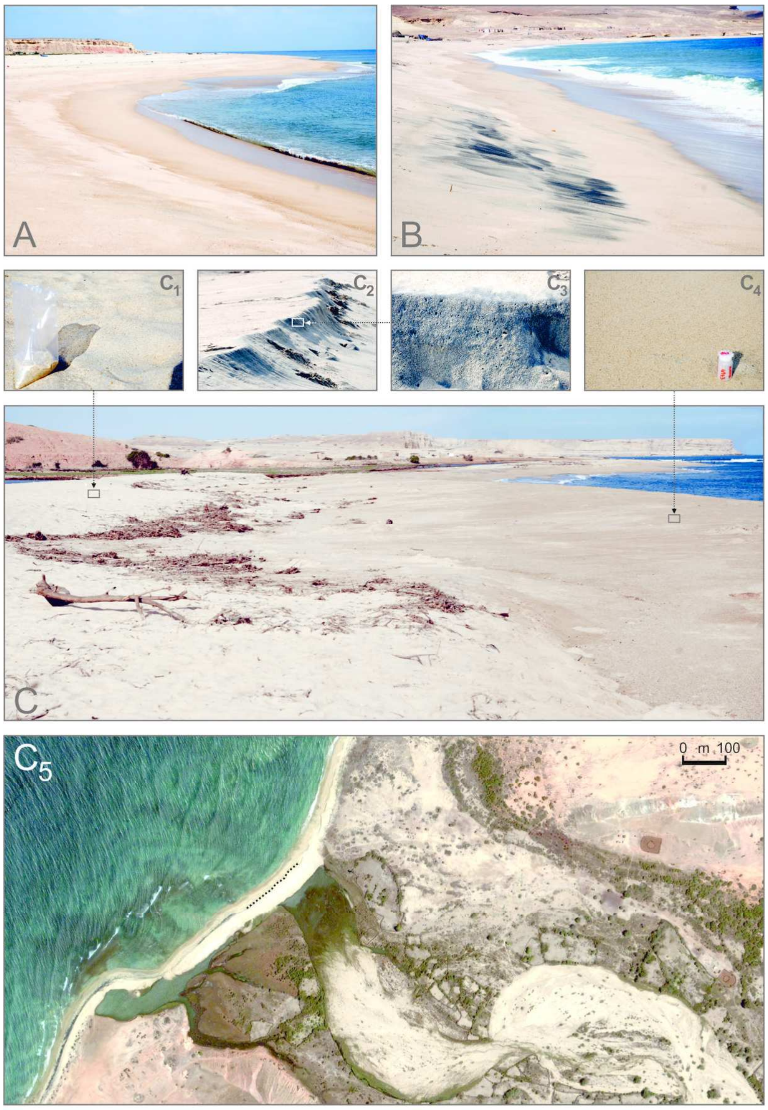

Figure 3 Moçamedes

Figure 3. Beaches and beach placers north of Namibe. A) Beach in equilibrium at Baia das Salinas. B) Foreshore laminae locally enriched strongly in Fe-Ti-Cr oxides at Bentiaba. C) Composite beach at Inamangando (view looking southwest): C1) high inner berm of white sand with the same mineralogy as river sand (Figs. 7E1); C2) parallel laminae enriched strongly in Fe-Ti-Cr oxides characterize erosion scarp at foreshore top (C3); C4) low outer berm of darker sand enriched notably in Fe-Ti-Cr oxides (Fig. 7E2); C5) Google Earth image of the composite beach at the Inamangando River mouth, showing lateral continuity in space and persistence in time of the white high inner berm and heavy-mineral-enriched creamy orange low outer berm (boundary indicated by black dotted line). Localities indicated in Figure 4.

Fig. 3

136x208mm (300 x 300 DPI)

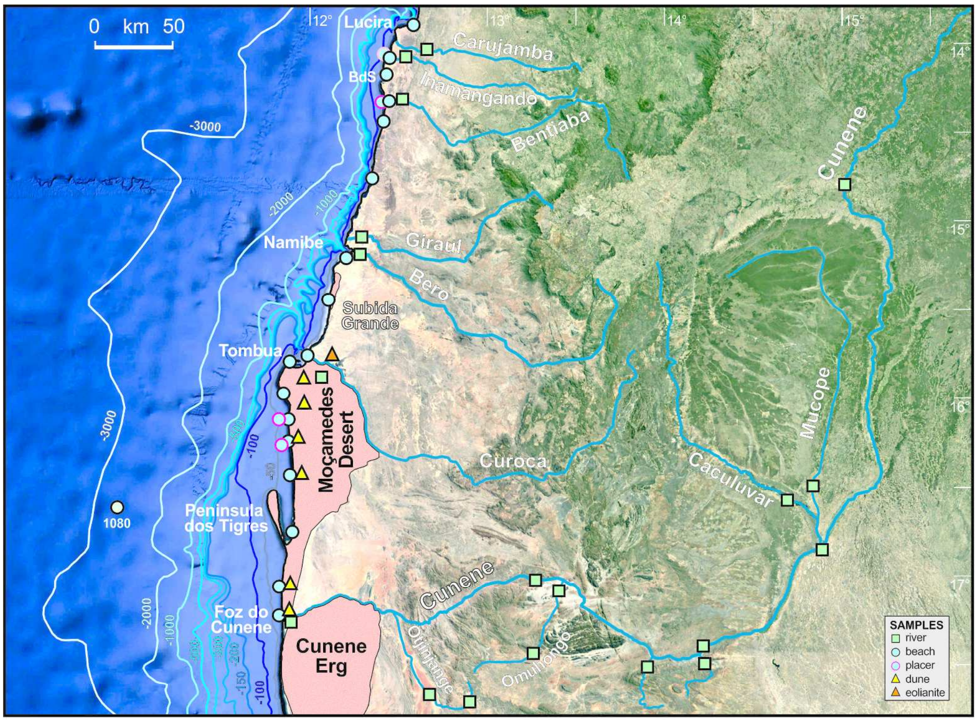

Figure 4 Moçamedes

Figure 4. Topography of the southern Angola continental margin, showing bathymetry and sample locations. The shelf, still relatively wide offshore of the southern Moçamedes Desert, tapers off at Tombua. The Curoca and Bero mouths are associated with a deep canyon reaching close to shore (Fig. 15). A field of coppice dunes (Fig. 2E) occurs between Subida Grande and Namibe, but farther north the shelfbreak comes even closer to the coast and dunefields disappear. BdS= Baia das Salinas.

Fig. 4
242x193mm (300 x 300 DPI)

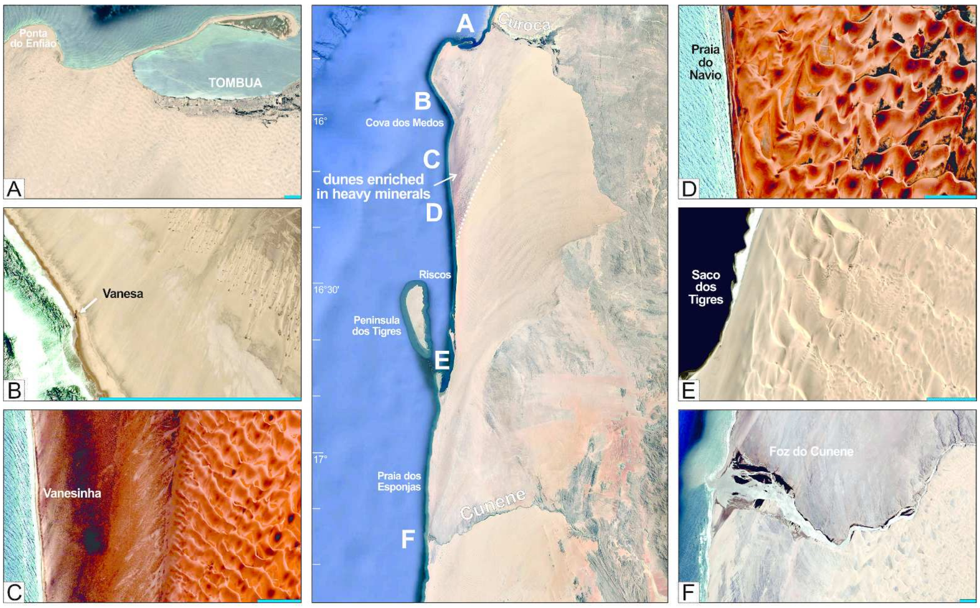

Figure 5 Moçamedes

Figure 5. Google Earth images of selected sampling sites in the Moçamedes Desert. Changes in dune color largely reflect different hydrodynamic concentration of ultradense garnet and Fe-Ti-Cr oxides, which increases markedly and rather abruptly in the northern part of the desert (north of white dotted line), where shelf width decreases rapidly offshore (Fig. 4). A) Small field of yellow barchan dunes south of Tombua Bay, which is delimited by a sand spit. Wave refraction at the point of coastal re-entrant fosters accumulation of drifting sand and incipient formation of a new spit at Ponta do Enfião (fig. 8 in Guilcher et al., 1973); B) Deflation of ochre sand in the backshore of Vanesa beach (note small linear dunes formed in the lee of shrubs; arrow points at shipwreck seen in Fig. 2C); C) Deflation of dark red sand in the backshore of Vanesinha beach (Fig. 2A,B) with composite red barchan dunes inland; D) Coalescent red barchan dunes at Praia do Navio; E) Composite yellow transverse dunes at Baia dos Tigres, a toponym seemingly chosen by sailors because concentration of red garnet and black Fe-Ti-Cr oxides makes beaches and dunes look like tiger stripes from the sea; F) The Cunene River separates sharply the Cunene Erg in the south from a deflation area in the north. The direction of swell waves is constantly from the southwest. Blue bar for scale = 500 m.

Fig. 5

327x216mm (300 x 300 DPI)

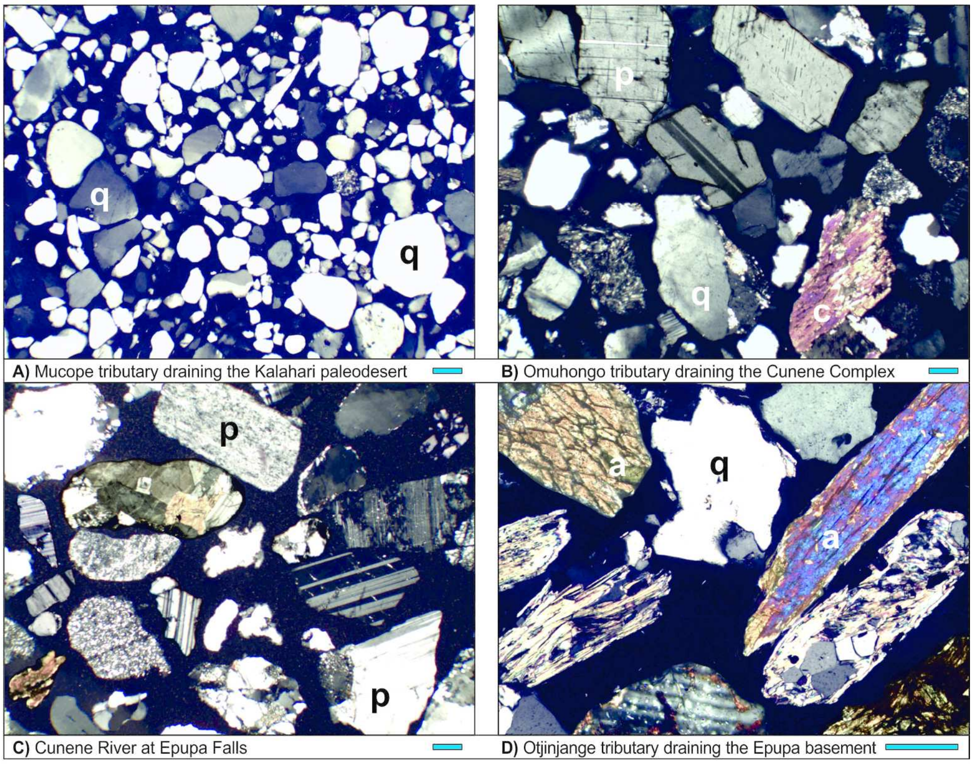

Figure 6 Moçamedes

Figure 6. Petrographic signatures in the Cunene River system. A) Pure quartzose recycled sand supplied to the upper course (q = quartz). B) Quartzo-feldspathic plutoniclastic sand supplied to the lower course (p = plagioclase; c = clinopyroxene). C) Plagioclase-rich feldspatho-quartzose trunk-river sand in the lower course upstream of the coastal Cunene dunefield. D) Litho-feldspatho-quartzose metamorphiclastic sand supplied in the terminal tract (a = amphibole). All photos with crossed polars; blue bar for scale = 250 μm.
Fig. 6
186x157mm (300 x 300 DPI)

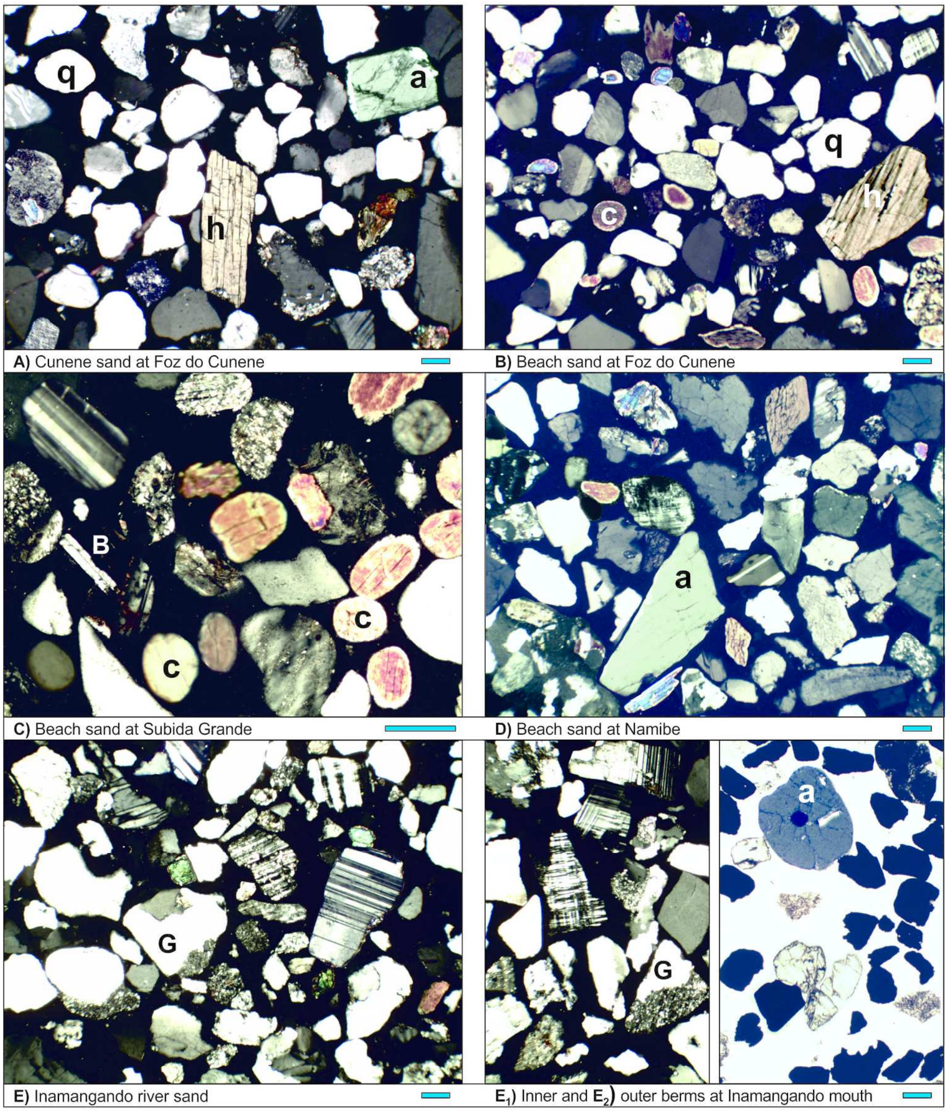

Figure 7 Moçamedes

Figure 7. Changes in sand composition in southern Angola. A) River sand at Cunene mouth reveals extensive mixing with dune sand fed from northward littoral drift (q = quartz; a = amphibole; h = hypersthene). B) Beach sand at Cunene mouth is mainly derived ultralong-distance from the Orange River. Orange-derived small rounded clinopyroxene (c) contrasts with Cunene-derived oversized angular orthopyroxene (h). C) Small rounded clinopyroxene grains and basaltic rock fragments (B) derived from as far as Lesotho highlands at the end of the Orange littoral cell. D) Feldspar-rich sand with granitoid rock fragments (G) derived from Angolan basement is supplied via the Bero River to the Namibe beach. E) Feldspar-rich feldspatho-quartzose Inamangando River sand; E1) sand with identical composition deposited on the high inner berm at the Inamangando mouth; E2) marked enrichment in opaque and transparent heavy-minerals in the low outer berm. All photos but E2 with crossed polars; blue bar for scale = 250 μm.
Fig. 7
184x228mm (300 x 300 DPI)

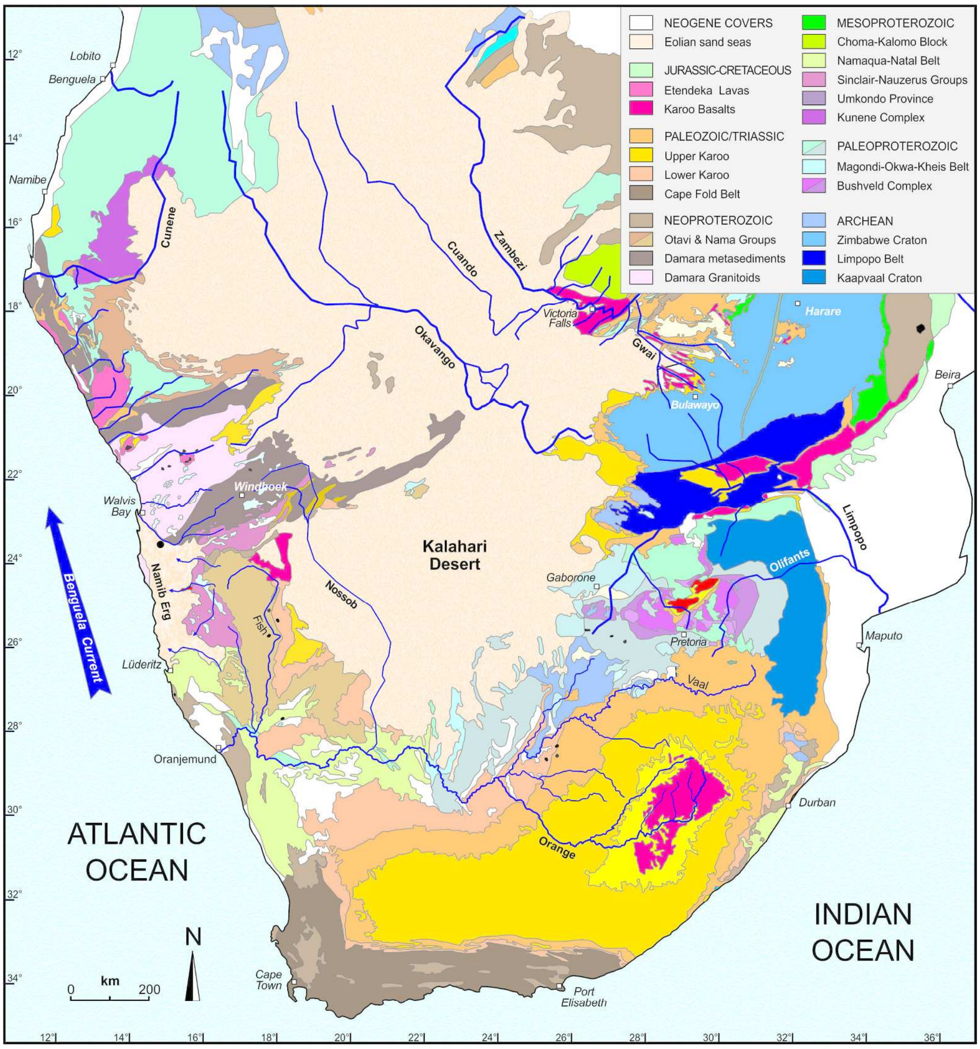

Figure 8 Moçamedes

Figure 8. Sketch geological map showing major tectonic domains and river drainages in southern Africa (compiled after Schlüter, 2008 and other sources cited in text).
Fig. 8
211x238mm (300 x 300 DPI)

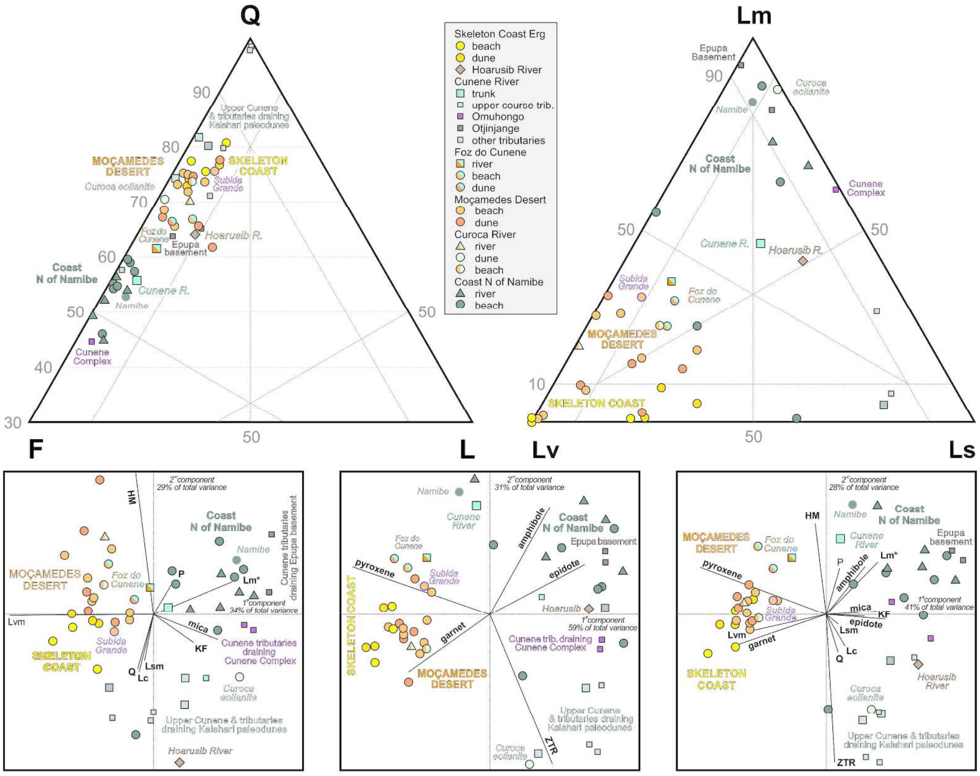

Figure 9 Moçamedes

Figure 9. Petrography and heavy minerals in sands of southern Angola. Composition of Moçamedes Desert sand is close to Skeleton Coast sand with additional contribution from the Cunene River. Composition of Cunene sand changes progressively from the upper course largely draining fossil Kalahari dunes to the lower course draining the Cunene igneous complex and Epupa basement before cutting across the coastal dunefield. Very extensive mixing with coastal eolian sand occurs in the final tract of the Curoca River. The Orange littoral cell terminates at Namibe, and beach sand to the north is supplied by local rivers draining Angolan basement with minor recycling of Cretaceous to Miocene strata exposed near the coast. Q = quartz; F = feldspar (KF = K-feldspar; P = plagioclase); L = lithic fragments (Lm = metamorphic; Lv = volcanic; Ls = sedimentary; Lc = carbonate; Lsm = sedimentary + low-rank metasedimentary; Lvm = volcanic + low-rank metavolcanic; Lm* = medium/high-rank metamorphic); HM = heavy minerals; ZTR = zircon + tourmaline + rutile. Both multivariate observations (points) and variables (rays) are displayed in the compositional biplots (Gabriel, 1971). The length of each ray is proportional to the variance of the corresponding element in the data set. If the angle between two rays is close to 0°, 90°, or 180°, then the corresponding elements are directly correlated, uncorrelated, or inversely correlated, respectively.

Fig. 9

260x216mm (300 x 300 DPI)

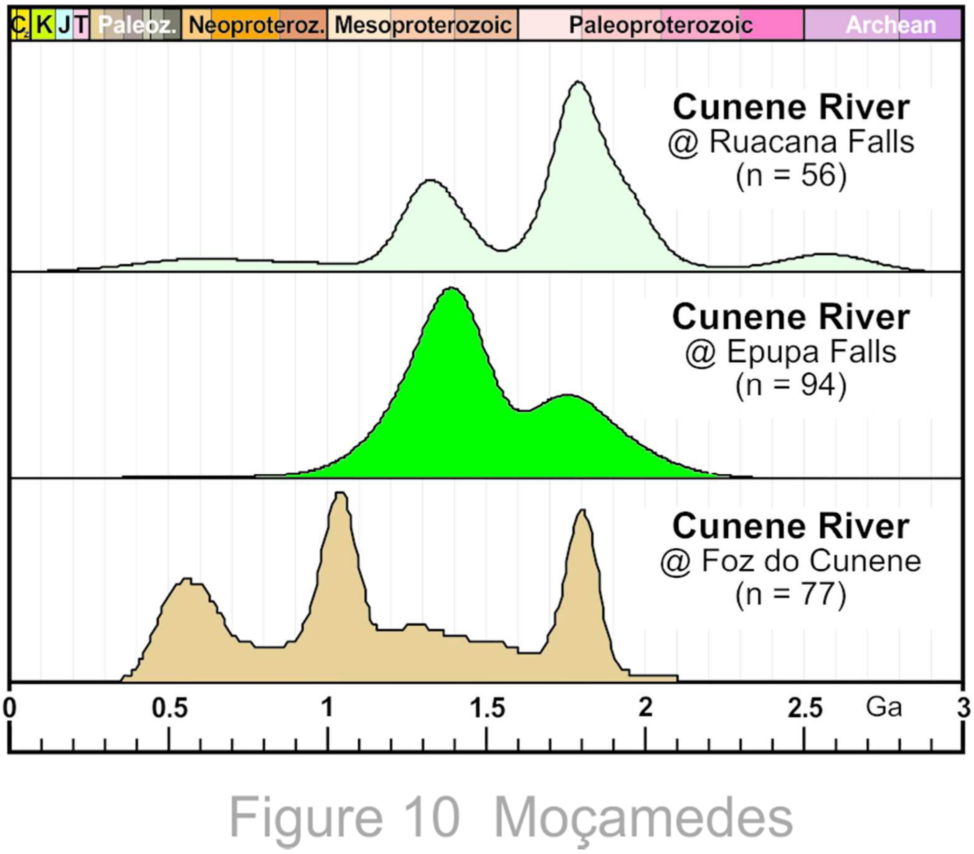

Figure 10. Downstream changes in U-Pb age spectra of detrital zircons in sands of the Cunene River (age vs. frequencies plotted as Kernel Density Estimates using the provenance package of Vermeesch et al., 2016). Paleoproterozoic to Neoarchean zircons are most abundant in the mildly sloped upper course draining fossil Kalahari dunes. Mid-Mesoproterozoic zircons become dominant in the much steeper youthful lower course, where erosion is focused and the river is incising rapidly into the Cunene igneous complex. Damara and Namaqua age peaks appear at the mouth, reflecting extensive mixing with windblown sand mostly derived ultralong-distance from the Orange River.

Fig. 10

74x64mm (300 x 300 DPI)

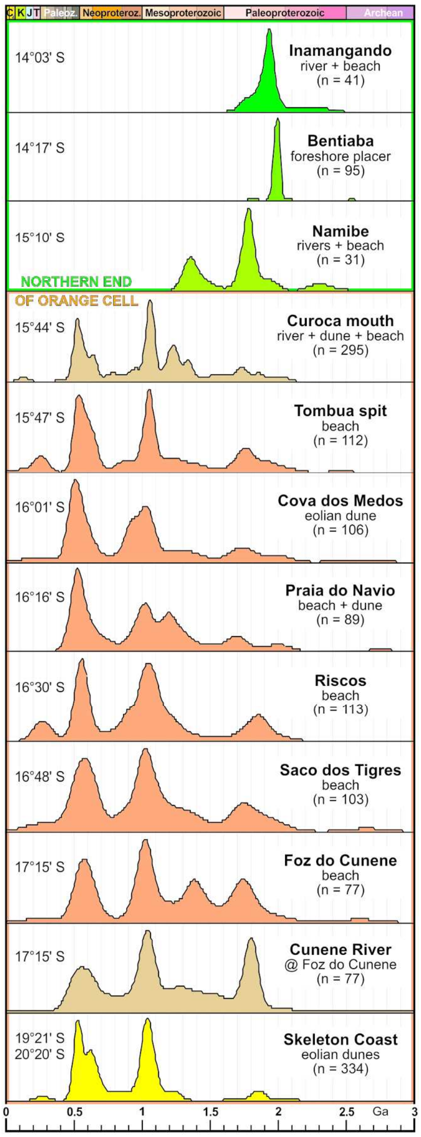

Figure 11 Moçamedes

Figure 11. U-Pb age spectra of detrital zircons in beach, dune and river sands from northern Namibia to southern Angola. The northern termination of the Orange littoral cell at 15°12'S is marked by the abrupt transition from bimodal spectra dominated by Damaran and Namaqua ages typical of Orange River and coastal Namibia sands to unimodal spectra dominated by Eburnean ages, reflecting provenance of most zircon grains from Paleoproterozoic crystalline rocks of the Angola Block (age vs. frequencies plotted as Kernel Density Estimates using software package provenance; Vermeesch et al., 2016). Age spectra of detrital zircons carried by the Cunene and Curoca Rivers at the mouth indicate that, rather than derived from their upstream reaches, they were mainly supplied long-distance from the Orange River and blown from the coast to choke the river valley inland. Nonetheless, significant zircon contribution from the Cunene River upstream of the coastal erg is documented by mid-Mesoproterozoic and late Paleoproterozoic peaks, which are notably larger in Moçamedes beaches and dunes than in Skeleton Coast dunes. Zircon contribution from the Curoca River upstream of the coastal erg is not evident.

Fig. 11

74x208mm (300 x 300 DPI)

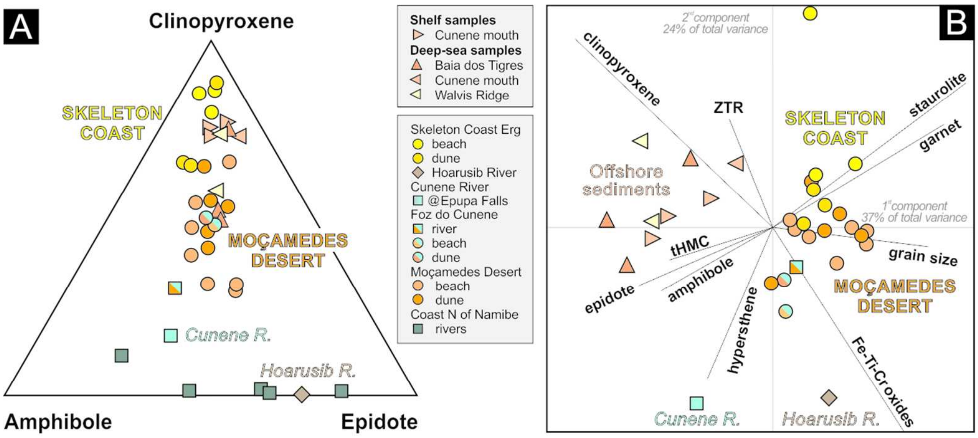

Figure 12 Moçamedes

Figure 12. Heavy minerals in recent sediments sampled from the Walvis Ridge to offshore of Baia dos Tigres. A) Offshore suites compare closely to either Skeleton Coast or Moçamedes Desert sands and differ drastically from those of all river sands from Namibia to Angola, documenting long-distance provenance mostly from the Orange mouth. B) Offshore suites tend to be depleted in ultradense minerals (garnet, opaque Fe-Ti-Cr oxides), preferentially retained in coastal sediments. ZTR = zircon + tourmaline + rutile; tHMC = transparent heavy-mineral concentration. In the compositional biplot (Gabriel, 1971), the angle between two rays is close to 0°, 90°, or 180° if the corresponding variables are directly correlated, uncorrelated, or inversely correlated, respectively.

Fig. 12
114x55mm (300 x 300 DPI)

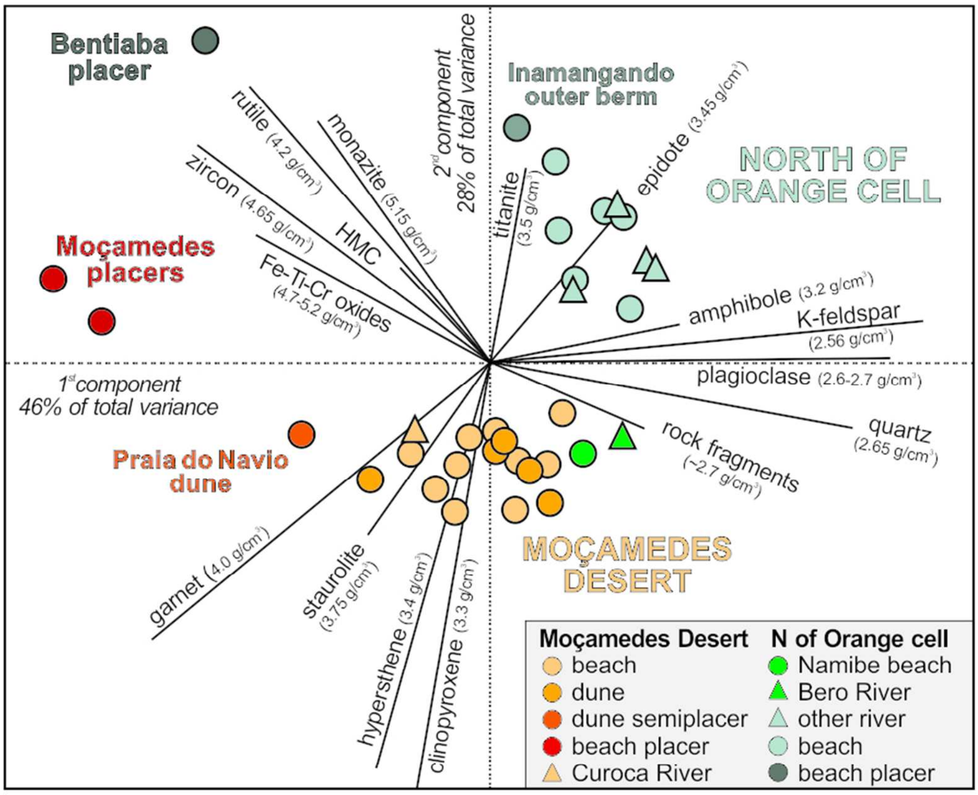

Figure 13 Moçamedes

Figure 13. Intersample mineralogical variability of beach and dune sands is controlled by both size-density sorting during selective entrainment (1st principal component) and provenance (2nd principal component). Low-density quartz, feldspars and rock fragments all correlate more and more negatively with denser and denser minerals. Moçamedes sand is richer in garnet, staurolite and pyroxenes, rivers and beaches north of Namibe in epidote and amphibole. HMC = Heavy Mineral Concentration. In the compositional biplot (Gabriel, 1971), the angle between two rays is close to 0°, 90°, or 180° if the corresponding variables are directly correlated, uncorrelated, or inversely correlated, respectively.

Fig. 13

75x66mm (300 x 300 DPI)

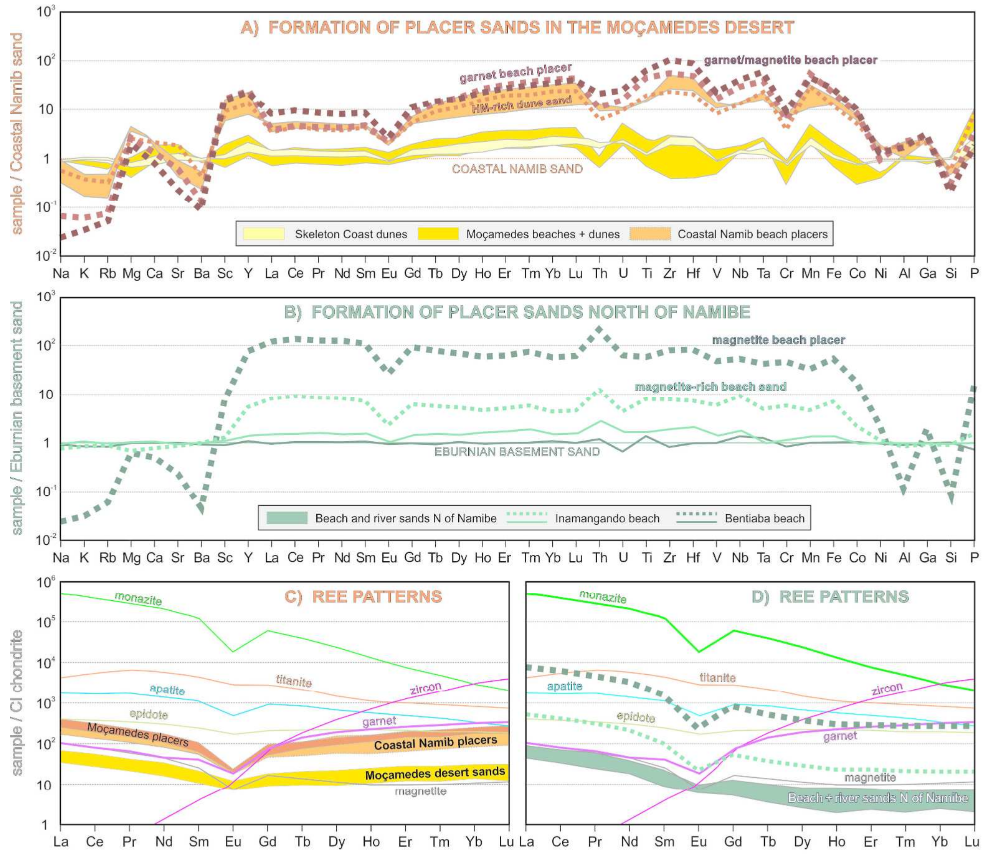

Figure 14 Moçamedes

Figure 14. Different patterns of intersample chemical variability in coastal sands of southern Angola (elements arranged following the periodic table group by group). In beach placers formed by selective-entrainment processes, Na, K, Rb, Ba, and Si hosted in low-density tectosilicates are depleted progressively, whereas Y, REE, Th, U, Ti, Zr, Hf, V, Nb, Ta, Cr, Mn, Fe, Co, and P hosted in dense and ultradense minerals are enriched, and the Eu anomaly is strongly negative. A) Moçamedes and Skeleton Coast sands have similar composition, indicating common long-distance provenance mainly from the Orange River. Moçamedes placers show the same pattern as Coastal Namib placers, with progressive increase in Sc, Y, HREE, and Mn reflecting garnet enrichment (concentrations normalized to averaged analyses of 19 Coastal Namib beach and dune sands after Garzanti et al., 2015b). B) Beach placers and semi-placers north of the Orange cell are enriched in LREE and especially Th, indicating monazite concentration, scarcity of garnet, and local provenance from Angolan basement rocks (concentrations normalized to averaged analyses of 8 beach and river sands collected between Namibe and Lucira). Chondrite-normalized REE patterns are controlled principally by the concentration of garnet in Coastal Namib and Moçamedes placer sands (C) and by concentration of monazite in placer sand derived from Angolan basement (D). REE patterns of heavy minerals after Garzanti et al. (2011).

Fig. 14

239x217mm (300 x 300 DPI)

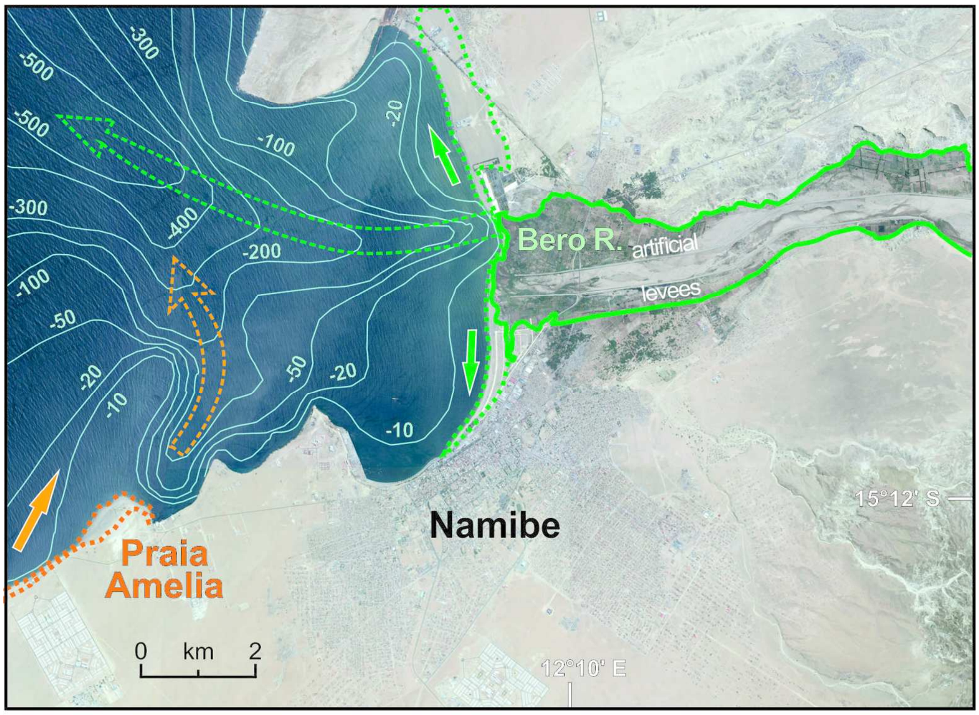

Figure 15 Moçamedes

Figure 15. The Orange littoral sand highway terminates abruptly just east of Praia Amelia, where garnet placers occur (Torquato, 1970). Sand dragged by swell waves from the south feeds the subaqueous spit in front of Praia Amelia, but it is funnelled next in the submarine canyon connected to the Bero mouth. The beach in Namibe Bay is supplied by the Bero River.
Fig. 15
150x120mm (300 x 300 DPI)

APPENDIX

" Sedimentary processes controlling ultralong cells of littoral transport : placer formation and termination of the Orange sand highway in southern Angola"

by Garzanti E., Dinis P., Vermeesch P., Andò S., Hahn A., Huvi J., Limonta M., Padoan, M., Resentini, A., Rittner M., Vezzoli, G.

A1 - Forward compositional modelling

Terrigenous sediments are complex mixtures of single detrital minerals and rock fragments supplied in various proportions by numerous different end-member sources (e.g., rivers) to successive segments of a sediment-routing system. If the compositional signature of detritus in each end-member source is known accurately, then the relative contributions from each source to the total sediment load can be quantified mathematically with forward mixing models (Draper and Smith 1981; Weltje, 1997). Several assumptions are made to derive a forward model from a series of compositions (Weltje and Prins 2003): 1) the order of the compositional variables or categories is irrelevant (permutation invariance); 2) the observed compositional variation reflects linear mixing or an analogous process with a superposed measurement error; 3) end-member compositions are fixed; 4) end-member compositions are as close as possible to observed compositions.

1. Compositional data

Geological data are often presented in percentages that represent relative contributions of the single variables to a whole (i.e. closed data; Chayes, 1971). This means that the relevant information is contained only in the ratios between variables of the data (i.e., compositions; Pawlowsky-Glahn and Egozcue, 2006). Compositional data are by definition vectors in which each variable (component) is positive, and all components sum to a constant c, which is usually chosen as 1 or 100.

The sample space for compositional data with D variables is not the real space R^D, but the simplex S^D (Aitchison, 1986)

$$(1) \qquad S^D = \left\{ x = [x_1, x_2, \ldots\ldots, x_D]; \qquad x_i > 0; \qquad i = 1,2,\ldots\ldots,D; \qquad \sum_{i=1}^{D} x_i = c \right\}.$$

Pearson (1897) first highlighted problems that arise with the analysis of such compositional datasets. The obvious and natural properties of compositional data are in fact in contradiction with most methods of standard multivariate statistics. Principal-component analysis, for instance, may lead to questionable results if directly applied to compositional data. In order to perform standard statistics, a family of logratio transformations from the simplex to the standard Euclidean space were introduced (Aitchison, 1986; Egozcue et al., 2003; Buccianti et al., 2006).

2. The mixing model

The forward mixing model (regression model) stipulates a linear relationship between a dependent variable (also called a response variable) and a set of explanatory variables (also called independent variables, or covariates). The relationship is stochastic, in the sense that the model is not exact, but subject to random variation, as expressed in an error term (also called disturbance term).

Let y be the row vector of compositional data with D columns representing variables, X a matrix of end-member compositions with n rows representing observations and D columns representing variables, and β a row vector of coefficients with $q = n$ columns representing the proportional contribution of the end members to the observation. In matrix notation, a forward mixing model can be expressed as

(2) $$y = \beta X + e.$$

The row vector y consists of a non-negative linear combination β of q end-member compositions, and e is the row vector of errors with D columns representing variables.

In order to solve the linear-regression problem, we must determine an estimation of the row vector β describing a functional linear relation b between a matrix of end-member compositions X and an output row vector y. The solution of equation (2) consists in the calculation of the row vector of coefficients b such that

(3) $$\hat{y} = bX,$$

where $\hat{y}$ is a row vector of calculated compositional data with D columns representing variables. This equation represents a forward mixing model (or "perfect mixing"). The model parameters are subject to the following non-negativity and constant-sum constraints

(4) $$\sum_{k=1}^{q} b_k = 1, \qquad b_k \geq 0,$$

(5) $$\sum_{j=1}^{D} x_{kj} = 1, \qquad x_{kj} \geq 0.$$

It follows from equations (4) and (5) that

(6) $$\sum_{j=1}^{D} \hat{y}_j = c, \qquad \hat{y}_j \geq 0,$$

and thus

(7) $$\sum_{j=1}^{D} e_j = 0.$$

The goodness of fit of the forward mixing model can be assessed by the coefficient of multiple correlation *R*

(8) $$R = \sqrt{1-(RSS/TSS)},$$

where *RSS* is the residual sum of squares

(9) $$RSS = \sum_i (y_i - \hat{y}_i)^2,$$

and *TSS* is the total sum of squares

(10) $$TSS = \sum_i (y_i - \bar{y})^2.$$

The coefficient *R* departs from a decomposition of the total sum of squares into the "explained" sum of squares (the sum of squares of predicted values, in deviations from the mean) and the residual sum of squares. *R* is a measure of the extent to which the total variation of the dependent variable is explained by the forward model. The *R* statistic takes on a value between 0 and 1. A value of *R* close to 1, suggesting that the model explains well the variation in the dependent variable, is obviously important if one wishes to use the model for predictive or forecasting purposes. In provenance studies, the coefficient of multiple correlation *R* measures the similarity between theoretical detrital modes of sediments supplied by different combinations of diverse end-members sources and the observed detrital mode of one trunk-river sediment or sedimentary rock in the basin.

A2 - Calculation of zircon and monazite concentration

Chemical data allow us to assess precisely the amount of rare ultradense minerals hosting large amounts of specific trace elements such as zircon or monazite. Assuming that zircon contains ~60% ZrO_2 and that its contribution to bulk-sample Zr increases from ≤ 60% in heavy-mineral-depleted sands to ≤ 100% in placer deposits (Garzanti et al., 2010), beaches and dunes in the Skeleton Coast and Moçamedes Desert are calculated to contain ~0.04% zircon. This value appears to be somewhat higher than the zircon concentration estimated for Orange River (~0.02%), Coastal Namib dune (~0.03%) and beach sands (~0.01%), as well as for sands of rivers draining the Damara orogen in central Namibia (~0.02%), which supports progressive concentration of ultradense minerals in coastal sediments along the littoral cell.

Similar calculations can be made for monazite, based on assumed concentrations of LREE and Th in monazite and monazite contributions for these elements in the bulk sample. Beaches and dunes in both Skeleton Coast and Moçamedes Desert are thus calculated to contain ~0.003% monazite, a value intermediate between those calculated for Coastal Namib dune and beach sands (~0.002%) and for the Orange River and Namibian rivers draining the Damara orogen (~0.004%).

In the Praia do Navio dune semi-placer, zircon concentration is estimated to be ~0.64% (1.8% based on point counting), a full order of magnitude more than in neutral sand. Monazite, undetected optically, is estimated to represent 0.014% of the bulk sample based on chemical data. In Coastal Namib beach placers, zircon is estimated to reach ~1.4% and monazite ~0.03%. In the Vanesinha and Praia do Navio beach placers, zircon concentration is assessed at ~2.8% and ~1.5% (2.0±0.3% and 1.0±1.0% based on point and grain counting), and monazite concentration at ~0.05% and ~0.02% (0.3±0.3% for both beach placers based on point and grain counting).

In river and beach sands north of Namibe, equivalent values for zircon concentration are estimated from chemical data and point counting (~0.02%). Zircon concentration is estimated to be ~0.15% in the Inamangando outer berm semi-placer (0.29% based on point counting) and ~1.5 in the Bentiaba placer (2.8±0.5% based on point and grain counting). Monazite is estimated to represent ~0.004% of river and beach sands, where it was undetected optically, one order of magnitude more in the Inamangando outer berm semi-placer (~0.04%), and another order of magnitude more in the Bentiaba placer (0.68% versus 0.64% based on point and grain counting).

TABLE AND FIGURE CAPTIONS

Table A1. Sample location. Location of the studied sediment samples with year of sampling (see also the Google Earth file *Mocamedes.kmz*). Locality names in the Moçamedes Desert mostly after Torquato (1974).

Table A2. Sand petrography. GSZ= grain size. Q= quartz (Qp= polycrystalline); F= feldspars (KF= K-feldspar; P= plagioclase; Mic= cross-hatched microcline); L= aphanitic lithic grains (Lv= volcanic and subvolcanic; Lc= carbonate; Lh= chert; Lp= shale/siltstone; Lms= low-rank metasedimentary; Lmv= low-rank metavolcanic; Lmf= medium/high-rank metapelite/metapsammite/metafelsite; Lmb= medium/high-rank metabasite; Lu= ultramafic). HM= heavy minerals. Rock fragments: V= volcanic; Vm= intermediate and mafic volcanic; M= metamorphic; Mb= mafic metamorphic; n.d. = not determined. The Metamorphic Indices MI and MI* express the average metamorphic rank of rock fragments in each sample. MI varies from 0 (detritus shed by exclusively sedimentary and volcanic cover rocks) to 500 (very-high-rank detritus shed by exclusively high-grade basement rocks). MI* considers only metamorphic rock fragments, and thus varies from 100 (very-low-rank detritus shed by exclusively very low-grade metamorphic rocks) to 500 (Garzanti and Vezzoli, 2003).

Table A3. Heavy minerals. HM= heavy minerals; tHM= transparent heavy minerals; HMC and tHMC = total and transparent-heavy-mineral concentration indices (Garzanti and Andò, 2007); RF= rock fragments; n.d. = not determined. The ZTR index (sum of zircon, tourmaline and rutile over total transparent heavy minerals) evaluates the "chemical durability" of the detrital assemblage (Hubert 1962). The HCI (Hornblende Colour Index) and MMI (Metasedimentary Minerals Index) vary from 0 in detritus from greenschist-facies to lowermost amphibolite-facies rocks yielding exclusively blue/green amphibole and chloritoid, to 100 in detritus from granulite-facies rocks yielding exclusively brown hornblende and sillimanite, and are used to estimate the average metamorphic grade of metaigneous and metasedimentary source rocks, respectively (Andò et al. 2014).

Table A4. Raman point-counting of beach placers in the Moçamedes Desert and coastal Namib Erg. Composition of opaque Fe-Ti-Cr oxides is also indicated (magnetite* includes all Fe oxides and hydroxides; ilmenite* includes leucoxene). Carefully micro-quartered splits of placer sand were mounted on glass slides. All counted grains were identified under the Raman spectroscope (method described in detail in Andò et al., 2011). Each single grain within the counted area was identified on a photograph and numbered for grain counting and on a regularly spaced grid for point counting (Andò and Garzanti, 2014). Raman spectroscopy analyses were carried out with a Raman Renishaw inVia directly on loose grains spread on glass slides. After calibration using the 520.6 cm^{-1} Raman band of silicon internal standard, spectra were obtained by focusing the 532 nm laser beam on the grain surface for ~20 s for offshore samples. Raman counting of placer samples was carried out taking care to avoid heating of opaque Fe-Ti-Cr oxides by reducing the laser power down to 10% and by acquiring each spectrum for ~0.5 s in 60 cycles. HMC and tHMC = Heavy Mineral and transparent Heavy Mineral Concentration. &HM= other heavy minerals (including apatite, tourmaline, kyanite, Ti oxides of possibly authigenic origin, and few unidentified rare minerals).

Table A5. Discrimination of detrital pyroxenes in onshore and offshore sediments of the Orange littoral cell. Identification of clinopyroxenes, orthopyroxenes and pyroxenoids is based on diagnostic Raman peaks in the medium-frequency (around 666 cm^{-1}) and high-frequency (around 1000 cm^{-1}) regions (Huang et al. 2001; Wang et al., 2001; Tribaudino et al., 2012; Andò and

Garzanti, 2014). Augite prevails over diopside in most samples, with subordinate pigeonite, minor hypersthene, and sporadic pyroxenoid and enstatite.

Table A6. Composition of detrital garnets in beach placers of the Moçamedes Desert. Discrimination within the garnet isomorphous series is based on diagnostic Raman peaks, an efficient approach that allows rapid assessment of garnet chemistry (Bersani et al. 2009). The analysed detrital garnets are all pyralspites, with andradite and grossular molecules ≤ 10%. Most grains resulted to be almandine with pyrope molecule ≤ 36%, several nearly pure almandine, and several almandine with either spessartine or both pyrope and spessartine molecules. A few spessartine garnets, with or without almandine molecule, are also found. The pyrope molecule reaches 50% at most in a few grains also containing spessartine and almandine.

Table A7. Measured grain density and comparison with SRD values, heavy-mineral concentration indices, and percentages of ultradense minerals. Grain density was measured on a small (~ 1 g), micro-quartered fraction of the sand sample placed in a suitably small aluminium container, and weighed by a high-precision Mettler Toledo™ balance (0.1 mg readability) first in air and next immersed in deionized water. It is essential to wet the grains before immersion and take every possible care to avoid floating owing to surface tension. Mud must be eliminated by wet sieving. Grain density δ is thus obtained as: $\delta = W_{in\ air} / (W_{in\ air} - W_{in\ water}) \cdot \delta_{water}$, where the weight of the sand W is obtained as the total weight (sand + container) less the weight of the container, and δ_{water} is calculated at the measured temperature (e.g., 0.9982 g/ml at 20°C).

The HMC and tHMC (Heavy Mineral Concentration and transparent Heavy Mineral Concentration) indices are calculated as the volume percentage of total (HMC) and transparent (tHMC) heavy minerals, and the SRD (Source Rock Density) index as the weighted average density of extrabasinal terrigenous grains (Garzanti and Andò, 2007). The SRD index represents a maximum estimate of grain density, because an ideal density of each extrabasinal detrital component is assumed in its calculation, neglecting inclusions and weathering-induced alteration. Conversely, the measured density represents a minimum estimate of grain density in case of imperfect elimination of air from intergranular and intragranular pores. Moreover, the sediment may contain intrabasinal grains with low-density (e.g., rip-up clasts, glaucony pellets), intragranular porosity (e.g., shells of gastropods, tests of radiolaria or foraminifera), or irregular shape preventing the complete elimination of air bubbles during immersion. In order to increase analytical precision, four replicate measurements at least were made for each sample, and if good agreement was obtained then the maximum value was considered as the most accurate estimate. We observed that the discrepancy between the calculated SRD index and the measured grain density tends to increase in samples richer in opaque ferromagnetic minerals. The latter are generally mixtures of different oxides altered to various degrees in secondary hematite or leucoxene, and their density cannot be estimated accurately. Moreover, they tend to form grain clusters not easy to partition evenly during sample quartering. The largest discrepancies were caused by magnetite grains forming irregularly distributed lumps in the Inamangando outer berm semi-placer sample, which required 14 replicate measures on separately quartered fractions to obtain a reliable measure.

Table A8. Sand geochemistry (analyses made at ACME Laboratories, Vancouver; for information on adopted procedures, geostandards used and precision for various elements of group 4A-4B and code LF200 see http://acmelab.com). Elements analysed by aqua regia digestion (a.r.d.) are commonly underestimated because of only partial leaching of refractory minerals. Chemical weathering indices are defined in Nesbitt and Young (1982; CIA), Fedo et al. (1995; PIA), Harnois (1988; CIW), Garzanti et al. (2014; CIX), and Parker (1970; WIP). In order to avoid bias caused by hydraulic concentration of heavy minerals hosting Ti, REE and Th, α^{Al} values were normalized to non-mobile Al (Garzanti et al., 2014). The Eu anomaly is the measured chondrite-normalized Eu value over the value that Eu would have in a linear extrapolation between chondrite-normalized values of Sm and Gd. The Ce anomaly, indicative of redox state, is the measured PAAS-normalized Ce value over the value that Ce would have in a linear extrapolation between PAAS-normalized values of La and Pr. MREE is the average of Eu, Gd, Tb and Dy normalized to PAAS, MREE* the average of LREE (La, Ce, Pr, Nd) and HREE (Er, Tm, Yb, Lu) values (Haley et al., 2004). The chondrite-normalized La_N/Yb_N, La_N/Sm_N, Gd_N/Ho_N, and Ho_N/Yb_N ratios are also given. GSZ= grain size; D.L. = detection limit; n.d.= not determined.

Figure A1. **Chemical composition of detrital garnets**. Beach placers in the Moçamedes Desert contain pyralspite garnets with compositions that overlap widely the distribution of detrital garnets in Skeleton coast dunes, confirming common, long-distance provenance from the Orange River and subordinately from rivers draining amphibolite-facies metasediments of the Damara orogen in central Namibia (Gray et al., 2008). Classical Mg-(Fe+Mn)-Ca (Mange and Morton, 2007) and Mg-Mn-Ca (Teraoka et al., 1997; Win et al., 2007) ternary plots allow us to classify Moçamedes garnets as mainly of type Bi and subordinately of type A, suggesting provenance from amphibolite-facies rocks metamorphosed under low to intermediate P/T conditions and subordinately from higher-grade rocks. XMg, XFe, XMn and XCa are molecular proportions of Fe^{2+}, Mg, Ca and Mn (XMg is at the apex of both triangles).

APPENDIX B

U-Pb detrital zircon geochronology of modern sands from northern Namibia and southern Angola (analyses made at the London Geochronology Centre, University College London). We used $^{206}Pb/^{238}U$ and $^{207}Pb/^{206}Pb$ ages for zircons younger and older than 1100 Ma, respectively; grains with >10% age discordance were discarded. No common Pb correction was applied. Grains with +5/-15% age discordance were discarded.

CITED REFERENCES

Aitchison, J., 1986. The statistical analysis of compositional data. Chapman and Hall, London.

Andò, S., Garzanti, E., 2014. Raman spectroscopy in heavy-mineral studies. In: Scott, R., Smyth. H., Morton, A., Richardson, N. (Eds.), Sediment provenance studies in hydrocarbon exploration and production. Geological Society London, Special Publications 386, pp. 395-412.

Andó, S., Morton, A., Garzanti, E., 2014. Metamorphic grade of source rocks revealed by chemical fingerprints of detrital amphibole and garnet. In: Scott, R., Smyth. H., Morton, A., Richardson, N. (Eds.), Sediment provenance studies in hydrocarbon exploration and production. Geological Society London, Special Publications 386, pp. 351-371.

Andò, S., Vignola, P., Garzanti, E., 2011. Raman counting: a new method to determine provenance of silt. Rendiconti Lincei, 22, 327-347.

Bersani, D., Ando`, S., Vignola, P., Moltifiori, G., Marino, I.G., Lottici, P.P., Diella, V., 2009. Micro-Raman spectroscopy as a routine tool for garnet analysis. Spectrochimica Acta, Part A, 73, 484-491.

Buccianti, A., Mateu-Figueras, G., Pawlowsky-Glahn, V. (Eds.), 2006. Compositional Data Analysis in the Geosciences: From Theory to Practice. Geological Society, Special Publications 264, London.

Chayes, F., 1971. Ratio correlation: A manual for students of petrology and geochemistry. Univ. Chicago Press, Chicago (USA), 99 p.

Draper, N., and Smith, H. 1981. Applied regression analysis (2nd ed.). New York, Wiley, 709 p.

Egozcue, J. J., Pawlowsky-Glahn, V., Mateu-Figueraz, G., Barceló-Vidal, C., 2003. Isometric logratio transformations for compositional data analysis. Math. Geol. 35, 279-300.

Fedo, C.M., Nesbitt, H.W., Young, G.M., 1995. Unraveling the effects of potassium metasomatism in sedimentary rocks and paleosols, with implications for paleoweathering conditions and provenance. Geology, 23, 921-924.

Garzanti, E., Andò, S., 2007. Heavy-mineral concentration in modern sands: implications for provenance interpretation. In: Mange, M.A., Wright, D.T. (Eds.), Heavy Minerals in Use. Elsevier, Amsterdam, Developments in Sedimentology Series 58, pp.517-545.

Garzanti, E., Vezzoli, G., 2003. A classification of metamorphic grains in sands based on their composition and grade. Journal of Sedimentary Research, 73, 830-837.

Garzanti, E., Andó, S., France-Lanord, C., Vezzoli, G., Najman, Y., 2010. Mineralogical and chemical variability of fluvial sediments. 1. Bedload sand (Ganga-Brahmaputra, Bangladesh). Earth and Planetary Science Letters, 299, 368-381.

Garzanti, E., Vermeesch, P., Padoan, M., Resentini, A., Vezzoli, G., Andò, S., 2014. Provenance of passive-margin sand (southern Africa). The Journal of Geology, 122, 17-42.

Gray, D.R., Foster, D.A., Meert, J.G., Goscombe, B.D., Armstrong, R., Trouw, R.A.J., Passchier, C.W., 2008. A Damara Orogen perspective on the assembly of southwestern Gondwana. In: Pankhurst, R.J., Trouw, R.A.J., Brito Neves, B.B., De Wit, M.J. (Eds.), West Gondwana: pre-Cenozoic correlations across the South Atlantic region. Geological Society of London, Special Publication 294, 257-278.

Haley, B.A., Klinkhammer, G.P., McManus, J., 2004. Rare earth elements in pore waters of marine sediments. Geochimica Cosmochimica Acta, 68,1265-1279.

Harnois, L., 1988. The CIW index: a new chemical index of weathering. Sedimentary Geology, 55, 319-322.

Huang, E., Chen, C.H., Huang, T., Lin, E.H., Xu, J.A., 2000. Raman spectroscopic characteristics of Mg-Fe-Ca pyroxenes. American Mineralogist, 85, 473-479.

Hubert, J.F. 1962. A zircon-tourmaline-rutile maturity index and the interdependence of the composition of heavy minerals assemblages with the gross composition and texture of sandstones. Journal of Sedimentary Petrology 32:440-450.

Mange, M.A., Morton, A.C., 2007. Geochemistry of heavy minerals. In: Mange, M.A., Wright, D.T. (Eds.), Heavy Minerals in Use. Elsevier, Amsterdam, Developments in Sedimentology, 58, 345-391.

Nesbitt, H.W., Young, G.M., 1982. Early Proterozoic climates and plate motions inferred from major element chemistry of lutites. Nature, 299, 715-717.

Parker, A., 1970. An index of weathering for silicate rocks. Geological Magazine, 107, 501-504.

Pawlowsky-Glahn, V., Egozcue, J.J., 2006. Compositional data and their analysis: an introduction. In: Buccianti, A., Mateu-Figueras, G., Pawlowsky- Glahn, V. (Eds.), Compositional data analysis in the geosciences: From theory to practice. Geological Society of London Special Publications 264, pp. 1–10.

Pearson, K., 1897. Mathematical contributions to the theory of evolution. On a form of spurious correlation which may arise when indices are used in the measurement of organs. Proceedings of the Royal Society of London LX, 489–502.

Teraoka, Y., Suzuki, M., Hayashi, T., Kawakami, K., 1997. Detrital garnets from Paleozoic and Mesozoic sandstones in the Onogawa Area, East Kyushu, Southwest Japan. Bulletin of the Faculty of Education Hiroshima University, 19, 87-101 (in Japanese, English abstract).

Torquato, J.R., 1974. Geologia do sudoeste do Moçamedes e suas relaçoes con a evoluçao tectonica de Angola. Tese de doutoramento, Instituto de Geociencias, Universidade de São Paulo, 343 p.

Tribaudino, M., Mantovani, L., Bersani, D., Lottici, P.P., 2012. Raman spectroscopy of (Ca, Mg) $MgSi_2O_6$ clinopyroxenes. American Mineralogist, 97, 1339-1347.

Wang, A., Jolliff, B.L., Haskin, L.A., Kuebler, K.E., Viskupic, K.M., 2001. Characterization and comparison of structural and compositional features of planetary quadrilateral pyroxenes by Raman spectroscopy. American Mineralogist, 86, 790-806.

Weltje, G. J., 1997. End-member modelling of compositional data: numerical statistical algorithms for solving the explicit mixing problem. Math. Geol. 29, 503-549.

Weltje, G.J., Prins, M.A., 2003. Muddled or mixed? Inferring palaeoclimate from size distributions of deep-sea clastics. Sedimentary Geology 162, 39–62.

Win, K.S., Takeuchi, M., Tokiwa, T., 2007. Changes in detrital garnet assemblages related to transpressive uplifting associated with strike–slip faulting: an example from the Cretaceous System in Kii Peninsula, southwest Japan. Sedimentary Geology, 201, 412-431.

Table A1

Sample	River /Cruise	Site	Latitude	Longitude	Facies	Country	Collected by	Year
SOUTHERN ANGOLAN COAST								
S4941		Lucira	S 13 51 58	E 12 31 14	beach	Angola	E.Garzanti	2015
S4942	Carujamba	Lucira	S 13 59 19	E 12 31 01	fluvial	Angola	E.Garzanti	2015
S4943		Inamangando	S 14 02 33	E 12 23 09	outer berm	Angola	E.Garzanti	2015
S4944		Inamangando	S 14 02 34	E 12 23 10	inner berm	Angola	E.Garzanti	2015
S4945	Inamangando	Inamangando	S 14 03 04	E 12 25 38	fluvial	Angola	E.Garzanti	2015
S4946		Baia das Salinas	S 14 11 18	E 12 20 38	beach	Angola	E.Garzanti	2015
S4947	Bentiaba	Bentiaba	S 14 16 05	E 12 22 46	fluvial	Angola	E.Garzanti	2015
P4948		Bentiaba	S 14 17 23	E 12 22 11	beach placer	Angola	E.Garzanti	2015
S4948		Bentiaba	S 14 17 23	E 12 22 11	beach	Angola	E.Garzanti	2015
S4949		Chapeu Armado	S 14 26 55	E 12 20 38	beach	Angola	E.Garzanti	2015
S4950		Mariquita	S 14 45 41	E 12 17 04	beach	Angola	E.Garzanti	2015
S4951	Giraul	Giraul	S 15 04 30	E 12 09 18	fluvial	Angola	E.Garzanti	2015
S4952	Bero	Namibe	S 15 09 54	E 12 10 05	fluvial	Angola	E.Garzanti	2015
S4953		Namibe	S 15 11 32	E 12 08 50	beach	Angola	E.Garzanti	2015
S4954		Subida Grande	S 15 25 21	E 12 01 54	beach	Angola	E.Garzanti	2015
S4955	Curoca	Curoca mouth	S 15 43 53	E 11 55 24	fluvial	Angola	E.Garzanti	2015
S4956		Curoca mouth	S 15 43 56	E 11 54 38	beach	Angola	E.Garzanti	2015
S4802		Nonguai	S 15 45 57	E 12 04 40	fossil dune	Angola	P.Dinis	2014
MOÇAMEDES DESERT								
S4804		Tombua	S 15 47 54	E 11 51 18	beach	Angola	P.Dinis	2014
S4805		Tombua outer spit	S 15 47 20	E 11 49 08	beach	Angola	P.Dinis	2014
S4774		Tombua	S 15 47 56	E 11 51 54	eolian dune	Angola	E.Baptista	2014
S4957		Vanesa	S 15 57 09	E 11 46 06	beach	Angola	E.Garzanti	2015
S4961		Cova dos Medos	S 16 01 24	E 11 48 47	eolian dune	Angola	E.Garzanti	2015
S4958		Vanesinha	S 16 09 25	E 11 47 36	beach	Angola	E.Garzanti	2015
P4958		Vanesinha	S 16 09 25	E 11 47 36	beach placer	Angola	E.Garzanti	2015
S4960		Praia do Navio	S 16 16 25	E 11 48 44	eolian dune	Angola	P.Vermeesch	2015
S4959		Praia do Navio	S 16 16 23	E 11 48 35	beach	Angola	E.Garzanti	2015
P4959		Praia do Navio	S 16 16 23	E 11 48 35	beach placer	Angola	E.Garzanti	2015
S5059		Riscos	S 16 30 00	E 11 49 30	eolian dune	Angola	A.Sampaio	2016
S5058		Riscos	S 16 30 00	E 11 49 30	beach	Angola	A.Sampaio	2016
S5057		Saco dos Tigres	S 16 48 27	E 11 48 13	beach	Angola	A.Sampaio	2016
S5056		Praia dos Esponjas	S 17 05 00	E 11 45 08	eolian dune	Angola	A.Sampaio	2016
S5055		Praia dos Esponjas	S 17 05 00	E 11 45 08	beach	Angola	A.Sampaio	2016
S5054		Foz do Cunene	S 17 15 24	E 11 45 18	eolian dune	Angola	A.Sampaio	2016
S5053		Foz do Cunene	S 17 15 24	E 11 45 18	beach	Angola	A.Sampaio	2016
HOARUSIB & CUNENE RIVER SYSTEM								
S3938	Hoarusib	Purros	S 18 44 08	E 12 56 42	fluvial	Namibia	L.Ciceri	2008
S4773	Cunene	Matala	S 14 44 38	E 15 02 21	fluvial	Angola	A.Pereira	2014
S5049	Mucope	Techiulo	S 16 31 46	E 14 52 22	fluvial	Angola	A.Trindade	2016
S5050	Caculuvar	Techango	S 16 38 15	E 14 54 16	fluvial	Angola	A.Trindade	2016
S5051	Caculuvar confluenc	Omutele	S 16 46 12	E 14 54 55	fluvial	Angola	A.Trindade	2016
S3931	Cunene	Ruacana	S 17 24 30	E 14 13	fluvial	Namibia	L.Ciceri	2008
S3932	Ehomba	Ehomba	S 17 25 20	E 14 00 30	fluvial	Namibia	L.Ciceri	2008
S3933	Ondoto	Chitado	S 17 18 50	E 13 47 40	fluvial	Namibia	L.Ciceri	2008
S3935	Omuhongo	Etengua	S 17 28 20	E 13 03 40	fluvial	Namibia	L.Ciceri	2008
S3934	Omuhongo	Oryeheke	S 16 59 20	E 13 22 10	fluvial	Namibia	L.Ciceri	2008
S4775	Cunene	Epupa Falls	S 17 00	E 13 15	fluvial	Namibia	F.Vermeesch	2014
S3936	Otjinjange	Van Zyl's Pass	S 17 37 40	E 12 42 50	fluvial	Namibia	L.Ciceri	2008
S3937	Marienfluss	Otyoyonoka	S 17 39 20	E 12 38 00	fluvial	Namibia	L.Ciceri	2008
S5052	Cunene	Foz do Cunene	S 17 15 24	E 11 45 18	river mouth	Angola	A.Sampaio	2016
OFFSHORE CORE TOP SAMPLES					Depth (m)		Corer	
1019	Meteor M6/6	GeoB1019-3	S 17 10 29	E 11 38 50	-75	Cunene mouth	Giant box corer	1988
1020	Meteor M6/6	GeoB1020-1	S 17 10 07	E 11 32 53	-110	Cunene mouth	Giant box corer	1988
1021	Meteor M6/6	GeoB1021-3	S 17 10 34	E 11 24 00	-173	Cunene mouth	Giant box corer	1988
1022	Meteor M6/6	GeoB1022-2	S 17 10 24	E 11 17 53	-551	Cunene mouth	Giant box corer	1988
1704	Meteor 20/2	GeoB1704-1	S 19 24 24	E 11 36 42	-399	Walvis Ridge	Giant box corer	1992
1705	Meteor 20/2	GeoB1705-1	S 19 30 18	E 11 23 54	-642	Walvis Ridge	Gravity corer (Kiel type	1992
1/1 89-91	ODP Leg 175	1080 A	S 16 33 35	E 10 49 12	-2766	Baia dos Tigres	Hydraulic piston core	1997
2/4 31-33	ODP Leg 175	1080 A	S 16 33 35	E 10 49 12	-2766	Baia dos Tigres	Hydraulic piston core	1997
1/6 65-67	ODP Leg 175	1080 B	S 16 33 36	E 10 49 12	-2768	Baia dos Tigres	Hydraulic piston core	1997

Table A2

River / *(facies)*	Site	Sample	Operator	GSZ	Q	KF	P	Lv	Lc	Lh	Lp	Lms	Lmv	Lmf	Lmb	Lu	mica	HM		Q	F	L	**MI***	**MI**	Lm	Lv	Ls	Qp/Q	P/F	Mic/F	Vm/V	Mb/M
SOUTHERN ANGOLAN COAST				µm																												
	Lucira	S4941	A.Resentini	390	44	12	36	0	0.3	0	0	0	0.3	2	0.9	0	0.3	4.9	100.0	46	50	4	295	295	88	4	8	43	75	13	n.d.	30
Carujamba	Lucira	S4942	A.Resentini	490	48	21	29	0	0	0	0	0	0	0	0	0	0	1.6	100.0	49	51	0	n.d.	n.d.	n.d.	n.d.	n.d.	32	58	18	n.d.	n.d.
(outer berm)	Inamangando	S4943	G.Vezzoli	400	49	20	19	0	0	0	0	0	1	0	0.1	0	0	10.9	100.0	54	44	2	338	338	55	45	0	41	48	29	n.d.	58
(inner berm)	Inamangando	S4944	G.Vezzoli	340	51	19	22	0.3	0	0	0	0.3	0.3	0	0	0	0.3	6.8	100.0	55	44	1	240	200	n.d.	n.d.	n.d.	24	53	20	n.d.	30
Inamangando	Inamangando	S4945	A.Resentini	335	52	18	22	0	0.3	0	0.3	0	0.6	0.9	1	0	0.3	4.6	100.0	54	42	4	275	259	73	9	18	24	55	15	n.d.	41
(beach)	Baia das Salinas	S4946	G.Vezzoli	415	57	13	25	0	0	0	0	0	0.6	0	0.3	0	0.6	4.5	100.0	60	39	1	340	309	n.d.	n.d.	n.d.	34	66	11	n.d.	80
Bentiaba	Bentiaba	S4947	A.Resentini	350	52	19	28	0	0	0	0	0	0.3	0.3	0.3	0	0	1.2	100.0	52	47	1	317	317	n.d.	n.d.	n.d.	30	60	12	n.d.	42
(beach)	Bentiaba	S4948	G.Vezzoli	520	50	20	22	0.3	0.3	0	0	0	0.6	0	0	0	0	7.3	100.0	54	44	1	229	178	25	50	25	44	53	17	n.d.	50
(beach)	Chapeu Armado	S4949	G.Vezzoli	355	58	26	14	0.6	0.5	0	0.5	0	0	0	0	0	0	0	100.0	57	40	3	320	188	0	40	60	24	35	36	n.d.	0
(beach)	Mariquita	S4950	A.Resentini	670	59	20	19	0	0.3	0	0	0	0.3	0.3	0.3	0	0	0.9	100.0	59	40	1	350	300	63	13	25	24	49	12	n.d.	42
Giraul	Giraul	S4951	A.Resentini	325	53	17	23	0	0	0	0	0	0	0.6	0	0	0.3	5.2	100.0	56	43	1	250	250	n.d.	n.d.	n.d.	25	57	6	n.d.	6
Bero	Namibe	S4952	G.Vezzoli	230	42	16	32	0	0	0.3	0.7	0.3	0.3	2	0.3	0	1	5.1	100.0	45	51	4	350	311	67	4	29	12	67	7	n.d.	19
(beach)	Namibe	S4953	G.Vezzoli	325	47	12	27	0	0	0	0	0.6	0.6	0.9	1	0	0.3	9.8	100.0	53	43	4	383	358	83	8	8	11	70	3	n.d.	50
(beach)	Subida Grande	S4954	G.Vezzoli	285	75	7	11	3	0.3	0	0	0.6	0.8	1	0.3	0	0	1.4	100.0	76	18	6	277	144	33	59	9	7	63	7	58	35
fossil dune	Nonguai	S4802	A.Resentini	335	70	16	12	0	0	0	0	0.3	0	0.7	0.1	0	0.6	0.3	100.0	71	28	1	300	300	88	0	13	6	44	13	n.d.	13
Curoca	Curoca mouth	S4955	A.Resentini	320	62	6	16	3	0	0	0	0	0.6	0.6	0	0	0	12.0	100.0	70	24	5	200	80	20	80	0	7	74	11	100	33
(beach)	Curoca mouth	S4956	A.Resentini	345	69	7	13	2	0	0	0.3	0.6	0	0.3	0.3	0	0	7.2	100.0	74	22	4	200	83.3	25	58	17	10	65	5	100	20
MOÇAMEDES DESERT																																
(outer spit)	Tombua	S4805	A.Resentini	295	73	11	12	2	0	0	0	0	0	0	0	0	0	3.3	100.0	75	23	2	450	164	0	100	0	9	53	5	100	50
(eolian dune)	Tombua	S4774	G.Vezzoli	270	74	4	11	5	0	0	0.4	0	0	0.3	0.3	0	0.2	4.4	100.0	78	16	6	383	63.9	10	84	6	11	73	9	80	25
(beach)	Vanesa	S4957	A.Resentini	290	70	10	14	1	0	0	0	0.3	0	0	0	0	0	4.4	100.0	73	25	2	n.d.	28.6	8	83	8	9	59	18	100	n.d.
(eolian dune)	Cova dos Medos	S4961	G.Vezzoli	255	35	4	10	4	0.3	0	0.6	0.3	1	0	0.3	0	0	43.9	100.0	62	25	13	213	73.9	15	70	15	13	71	15	100	44
(beach)	Vanesinha	S4958	G.Vezzoli	300	60	5	11	2	0.6	0	0.3	0.9	0.3	0.3	0	0	0	18.9	100.0	74	20	6	233	111	19	53	28	9	67	12	88	17
(eolian dune)	Praia do Navio	S4960	A.Resentini	215	24	2	7	2	0	0	0	0	0	0	1	0	0	63.7	100.0	66	25	9	300	92.3	33	67	0	13	79	6	100	100
(beach)	Praia do Navio	S4959	A.Resentini	355	64	7	14	4	0	0	0	0	0	0	0	0	0	11.7	100.0	72	24	4	n.d.	68.8	0	100	0	12	68	11	100	n.d.
(eolian dune)	Riscos	S5059	G.Vezzoli	325	73	8	14	2	0	0.3	0.6	0	0.3	0.1	0.1	0	0	2.0	100.0	75	22	3	371	163	14	59	27	8	64	15	100	14
(beach)	Riscos	S5058	A.Resentini	165	57	8	16	1	0.3	0	0	0	0	0	0.3	0	0	16.7	100.0	69	29	2	n.d.	66.7	17	67	17	3	67	4	100	n.d.
(beach)	Saco dos Tigres	S5057	G.Vezzoli	345	74	9	13	2	0	0	0	0	0.3	0.6	0	0	0	1.2	100.0	75	22	3	260	108	28	72	0	14	59	15	100	10
(eolian dune)	Praia dos Esponjas	S5056	A.Resentini	325	65	12	17	2	0.6	0	0	0	0	0	0	0	0	3.7	100.0	67	30	3	n.d.	0	0	75	25	10	59	15	100	n.d.
(beach)	Praia dos Esponjas	S5055	G.Vezzoli	330	65	14	15	3	0	0	0.3	0	0.9	0.6	0.3	0	0	1.2	100.0	66	29	5	270	108	28	66	6	11	52	12	67	40
(eolian dune)	Foz do Cunene	S5054	G.Vezzoli	200	63	13	15	2	0	0	0.3	0.8	0.4	0.7	0	0	0.3	5.3	100.0	66	29	4	220	105	32	52	17	11	54	16	88	5
(beach)	Foz do Cunene	S5053	G.Vezzoli	340	57	9	13	3	0	0	0.6	1	1	0.3	0	0	0	15.0	100.0	67	26	7	192	100	25	57	18	8	59	17	78	35
HOARUSIB & CUNENE RIVER SYSTEM																																
Hoarusib	Purros	S3938	G.Vezzoli	200	63	16	10	1	3	0	0	2	0.3	3	0	0	1	0	100.0	64	27	9	284	244	42	18	40	53	39	28	60	6
Cunene	Matala	S4773	G.Vezzoli	230	75	19	6	0	0	0	0	0	0	0	0	0	0	0.3	100.0	75	25	0	n.d.	n.d.	n.d.	n.d.	n.d.	2	24	7	n.d.	n.d.
Mucope	Techiulo	S5049	A.Resentini	230	99	1	0	0	0	0	0	0	0	0	0	0	0	0	100.0	99	1	0	n.d.	n.d.	n.d.	n.d.	n.d.	5	0	25	n.d.	n.d.
Caculuvar	Techango	S5050	A.Resentini	470	99	1	0.3	0	0	0	0	0	0	0	0	0	0	0	100.0	99	1	0	n.d.	n.d.	n.d.	n.d.	n.d.	8	25	25	n.d.	n.d.
Caculuvar confluence	Omutele	S5051	A.Resentini	540	83	11	7	0	0	0	0	0	0	0	0	0	0	0	100.0	83	17	0	n.d.	n.d.	n.d.	n.d.	n.d.	14	38	19	n.d.	n.d.
Cunene	Ruacana	S3931	G.Vezzoli	130	79	12	4	0.6	1	0	1	0.3	0	0	0	0	0	1.4	100.0	80	17	3	n.d.	38.5	5	18	77	6	25	20	n.d.	n.d.
Ehomba	Ehomba	S3932	G.Vezzoli	120	80	11	2	0.9	0.9	0	4	0.3	0	0.3	0	0	0	0.6	100.0	80	14	6	n.d.	45.5	8	15	78	7	17	16	n.d.	n.d.
Ondoto	Chitado	S3933	G.Vezzoli	170	70	12	8	0.3	0	0	4	2	0.6	0.6	0.3	0	0.9	0.9	100.0	71	21	8	214	50.6	29	8	63	36	41	22	n.d.	21
Omuhongo	Etengua	S3935	G.Vezzoli	290	56	28	12	0	0	0	0	0	0.3	0.6	0.0	0	1	1.1	100.0	58	41	1	415	415	n.d.	n.d.	n.d.	34	31	31	n.d.	12
Omuhongo	Oryeheke	S3934	G.Vezzoli	370	43	25	26	0	0	0	0.9	0.3	0	1	0.3	0	0.6	2.1	100.0	45	53	3	319	213	61	0	39	47	51	17	n.d.	19
Cunene	Epupa Falls	S4775	G.Vezzoli	325	54	13	26	0.8	0	0	0.8	0.5	0.3	1	0.3	0	0.3	3.3	100.0	56	40	4	295	151	46	25	29	33	68	13	n.d.	17
Otjinjange	Van Zyl's Pass	S3936	G.Vezzoli	220	58	11	11	0	0.7	0	0.4	0	0.8	4	2	0	3	9.3	100.0	65	25	10	383	362	81	5	14	28	49	19	n.d.	35
Marienfluss	Otyoyonoka	S3937	G.Vezzoli	115	49	13	11	0	0	0	0	0	0.6	3	1	0	3	19.6	100.0	64	30	6	436	436	94	6	0	32	47	22	n.d.	44
Cunene	Foz do Cunene	S5052	G.Vezzoli	325	57	12	20	1	0	0	0	1	1	0.3	0	0.3	0.3	6.4	100.0	61	34	4	256	171	37	50	13	18	63	11	80	34
OFFSHORE CORE TOP SAMPLES																																
110 m outer shelf offshore of Cunene mou		1020	G.Vezzoli	70	68	7	14	0.6	0	0	1	2	0.6	0.6	0	0	0	6.0	100.0	72	22	6	150	90	39	17	44	4	66	11	n.d.	8
173 m outer shelf offshore of Cunene mou		1021	G.Vezzoli	85	69	8	13	1	0.7	0	1	1	0.7	0	0	0	0.7	4.7	100.0	73	22	5	143	77	21	29	50	4	62	10	n.d.	21

Table A3

River / (facies)	Site	Sample	GSZ class (µm)	% finer	% class	% coarser	method	tHM counted	total grains	Operator	HMC	tHMC	HM %weight	tHM %weight	zircon	tourmaline	rutile	Ti oxides	titanite	apatite	epidote group	epidote in RF	garnet	staurolite	andalusite	kyanite	sillimanite	amphibole	oxy-hornblende	amphibole in RF	clinopyroxene	clinopyroxene in RF	hypersthene	enstatite	olivine	spinel	others		HCI	MMI	ZTR	% transparent	% opaques	% Fe oxides	% Ti oxides	% turbid HM	% rock fragments	% soils & turbid	% glaucony & phosphat	% chlorite	% biotite	% carbonates	% light minerals	total
SOUTHERN ANGOLAN COAST																																																						
(beach)	Lucira	S4941	<500	0%	59%	41%	Point	212	362	M.Padoan	5.8	3.4	6.0	3.5	0	0	1	0	2	2	42	35	0.9	0	0	0	0	9	0	8	0	0	0	0	0	0	0	100.0	2	n.d.	1	59%	7%	0%	0%	1%	30%	2%	0%	0%	2%	0%	0%	100%
Carujamba	Lucira	S4942	<500	0%	34%	66%	Point	246	278	M.Padoan	1.8	1.5	2.2	1.8	0.4	0	0	0	0.8	0	39	24	0	0	0	0	0	33	0	3	0	0	0	0	0	0	0	100.0	2	n.d.	0	84%	1%	0%	0%	0%	13%	0%	0%	0%	1%	0%	1%	100%
(outer berm)	Inamangando	S4943	<500	0%	53%	47%	Area	253	306	M.Padoan	12.5	3.2	20.9	5.4	9	1	2	0	3	1	47	20	0.8	0	0	0	0	16	0	0.4	0	0	0	0	0	0	0	100.0	0	n.d.	12	26%	68%	0%	0%	0%	5%	2%	0%	0%	0%	0%	0%	100%
(inner berm)	Inamangando	S4944	<500	0%	78%	22%	Point	229	2056	M.Padoan	6.6	4.3	8.2	5.3	1	0	0	0	1	0	45	14	0.4	0	0	0	0	34	0	1	0	0	2	0	0	0	0	100.0	5	n.d.	1	65%	25%	0%	0%	0%	8%	1%	0%	0%	0%	0%	0%	100%
Inamangando	Inamangando	S4945	15-500	0.2%	63%	37%	Point	209	329	M.Padoan	4.0	3.1	3.8	2.9	1	0	0	0	3	0	48	30	0	0	0	0	0	17	0	1	0	0	0	0	0	0	0	100.0	17	n.d.	1	76%	5%	0%	0%	0%	16%	0%	0%	0%	1%	0%	1%	100%
(beach)	Baia das Salinas	S4946	<500	0%	43%	57%	Point	204	434	M.Padoan	5.0	4.1	6.4	5.2	0.5	0	0	0	2	1	35	16	0	0	0	0	0	44	0	2	0	0	0	0	0	0	0	100.0	5	n.d.	0	81%	7%	0%	0%	0%	10%	1%	0%	0%	1%	0%	0%	100%
Bentiaba	Bentiaba	S4947	15-500	0%	37%	63%	Point	208	298	M.Padoan	2.5	2.0	4.4	3.5	0	0	0	0	0.5	2	57	4	0	0	0	0	0	32	0	3	0.5	0	0	0	0	0	0	100.0	16	n.d.	0	81%	7%	0%	0%	0%	10%	0%	0%	0%	1%	0%	1%	100%
(beach)	Bentiaba	S4948	<500	0%	42%	58%	Point	210	1285	M.Padoan	6.9	4.2	7.4	4.5	1	0	2	0	1	0	38	27	0.5	0	0	0	0	22	0	7	0.5	0	0	0	0	0	0	100.0	4	n.d.	3	60%	21%	0%	0%	0%	18%	1%	0%	0%	0%	0%	0%	100%
(beach)	Chapeu Armado	S4949	<500	0%	79%	21%	Point	217	1229	M.Padoan	0.6	0.3	1.5	0.6	19	0	5	0	6	4	35	11	8	0	0	0	0	9	0	1	1	0.9	0.5	0	0	0	0	100.0	11	n.d.	24	41%	33%	0%	0%	0%	21%	2%	0%	0%	1%	1%	1%	100%
(beach)	Mariquita	S4950	<500	0%	19%	81%	Point	227	305	M.Padoan	1.5	0.7	1.5	0.7	0	0	1	0	0	0	22	19	2	0	0	0	0	33	0	13	11	0.4	0	0	0	0	0	100.0	1	n.d.	1	48%	3%	0%	0%	3%	45%	0%	0%	0%	0%	0%	1%	100%
Giraul	Giraul	S4951	15-500	0%	23%	77%	Point	224	974	M.Padoan	4.5	3.2	4.8	3.4	0.9	0	0	0	1	0.4	32	10	3	0	0	0	0	46	0	5	0.4	0	0.4	0	0	0	0	100.0	7	n.d.	1	71%	18%	0%	0%	2%	8%	1%	0%	0%	1%	0%	0%	100%
Bero	Namibe	S4952	15-500	0%	42%	58%	Point	223	1435	M.Padoan	5.1	3.1	4.5	2.8	0	0	0	0	0	0.9	11	10	0.4	0	0	0	0.4	46	0	15	8	1	7	0	0	0	0	100.0	5	n.d.	0	62%	6%	0%	0%	2%	27%	3%	0%	0%	0%	0%	1%	100%
(beach)	Namibe	S4953	<500	0%	96%	4%	Point	204	1131	S.Andò	10.8	7.9	13.4	9.8	0	0	0	0	2	0.5	24	5	1	0	0	0	0	44	0	5	9	0	7	1	1	0	0	100.0	14	n.d.	0	73%	10%	1%	1%	2%	10%	0%	0%	0%	1%	0%	1%	100%
(beach)	Subida Grande	S4954	<500	0%	99%	1%	Point	210	257	S.Andò	2.3	1.6	3.1	2.2	0.5	2	0	0	1	0.5	16	2	10	2	0.5	0	0	23	0	1	35	1	4	0	0	0	1	100.0	26	50	2	69%	5%	1%	1%	0%	16%	1%	4%	0%	0%	3%	1%	100%
(fossil dune)	Nonguai	S4802	<500	0%	97%	3%	Point	223	474	M.Padoan	0.2	0.1	0.2	0.1	9	25	1	0	2	1	8	1	23	27	0	1	0	2	0	0	0	0	0	0	0	0	0	100.0	n.d.	50	35	51%	26%	0%	1%	0%	15%	5%	0%	0%	0%	0%	1%	100%
Curoca	Curoca mouth	S4955	15-500	0.1%	98%	2%	Point	1342	649	M.Padoan	10.9	7.1	13.1	8.5	5	2	0.4	0	0.4	0.8	17	2	28	2	0	0	0	7	0.2	0.2	31	2	3	0	0	0	0	100.0	10	50	7	65%	26%	0%	0%	1%	6%	1%	0%	0%	0%	0%	2%	100%
(beach)	Curoca mouth	S4956	<500	0%	95%	5%	Point	200	303	M.Padoan	7.6	4.6	10.4	6.3	3	4	0	0	1	0	13	3	44	6	0	0	0	12	0	1	12	0	5	0	0	0	0	100.0	14	50	7	61%	25%	0%	0%	3%	8%	3%	0%	0%	0%	0%	1%	100%
MOÇAMEDES DESERT																																																						
(outer spit)	Tombua	S4805	<500	0%	97%	3%	Point	892	264	M.Padoan	2.9	2.0	2.8	1.9	1	4	0.6	0	0	0.7	14	3	23	2	0	0	0.4	18	0	4	25	0.4	4	0	0	0	0	100.0	16	58	5	69%	12%	0%	0%	2%	11%	3%	0%	0%	0%	0%	2%	100%
(eolian dune)	Tombua	S4774	bulk	0%	100%	0%	Point	206	341	S.Andò	4.7	3.2	5.4	3.7	0	2	1	0	1	0	9	2	24	3	0	0	0	12	0	0.5	39	3	1	0	0.5	0	0	100.0	1	50	4	69%	6%	3%	1%	1%	7%	4%	8%	0%	0%	0%	0%	100%
(beach)	Vanesa	S4957	<500	0%	97%	3%	Point	798	348	M.Padoan	3.9	2.6	4.0	2.6	2	3	0.5	0	0	0.1	11	3	43	7	0	0.5	0	11	0	3	13	0	4	0	0	0	0	100.0	15	50	6	65%	13%	0%	0%	3%	15%	3%	0%	0%	0%	0%	1%	100%
(eolian dune)	Cova dos Medos	S4961	<500	0%	98%	2%	Point	212	285	M.Padoan	30.2	21.0	18.5	12.9	2	1	0.5	0	0	0	11	3	39	5	0	0	0	13	0	1	19	0.5	4	0	0	0	0	100.0	4	50	4	70%	12%	0%	0%	1%	14%	2%	0%	0%	0%	0%	1%	100%
(beach)	Vanesinha	S4958	<500	0%	97%	3%	Point	768	276	S.Andò	15.1	11.9	14.5	11.5	0.1	1	0	0	0.3	0.5	5	5	68	4	0	0	0.3	6	0	0.8	7	0	2	0	0	0	0	100.0	20	53	1	79%	11%	1%	1%	0%	7%	1%	0%	0%	0%	0%	0%	100%
(eolian dune)	Praia do Navio	S4960	<500	0%	99%	1%	Point	771	292	M.Padoan	51.7	27.8	49.8	26.8	6	1	1	0	0	1	6	0.3	62	4	0	0	0.3	6	0	0.3	11	0	1	0	0	0.1	0	100.0	10	53	8	54%	38%	0%	0%	1%	3%	1%	0%	0%	0%	0%	3%	100%
(beach)	Praia do Navio	S4959	<500	0%	99%	1%	Point	764	320	M.Padoan	11.8	8.0	15.2	10.3	3	1	0	0	0	0.7	11	1	53	8	0	0	0.5	8	0.3	0.4	9	0.5	2	0	0	0	0	100.0	24	53	5	68%	19%	0%	0%	2%	7%	3%	0%	0%	0%	0%	1%	100%
(eolian dune)	Riscos	S5059	<500	0%	100%	0%	Point	201	438	S.Andò	1.9	1.5	2.5	1.9	3	1	0	0.5	1	0	12	1	42	3	0	0	0.5	8	0	0.5	21	3	2	0	0	0	0	100.0	18	57	4	78%	12%	2%	1%	0%	5%	1%	0.8%	0%	0%	0%	0%	100%
(beach)	Riscos	S5058	<500	0%	100%	0%	Point	480	352	M.Padoan	12.9	9.5	11.3	8.4	3	2	0.6	0	0	0.6	13	2	21	2	0	0	0	8	0	0.2	43	1	3	0	0	0	0	100.0	5	50	5	74%	16%	0%	0%	2%	6%	1%	0%	0%	0%	0%	1%	100%
(beach)	Saco dos Tigres	S5057	<500	0%	99%	1%	Point	201	484	S.Andò	2.0	1.3	3.7	2.5	0.5	2	0	0	2	0.5	6	1	46	1	0	0	0	11	0	0	20	2	5	0	0	0	0	100.0	9	n.d.	2	66%	24%	0%	0%	0%	8%	0%	0.7%	0%	0%	1%	0%	100%
(eolian dune)	Praia dos Esponjas	S5056	<500	0%	40%	60%	Point	348	678	S.Andò	3.0	2.2	2.7	2.0	2	0	0	0	0.6	3	12	5	7	1	0	0	0	17	0.3	0.3	41	2	8	0	0	0	0.3	100.0	12	50	2	73%	14%	1%	0%	0%	7%	1%	0.2%	1%	1%	1%	0%	100%
(beach)	Praia dos Esponjas	S5055	<500	0%	82%	18%	Point	214	424	M.Padoan	1.7	1.1	2.1	1.3	0.5	2	0.5	0	2	2	11	7	7	3	0	1	0	21	0	3	37	0.5	2	0	0	0	0	100.0	17	50	3	63%	7%	0%	0%	4%	25%	1%	0%	0%	0%	0%	0%	100%
(eolian dune)	Foz do Cunene	S5054	<500	0%	100%	0%	Point	200	582	S.Andò	4.6	3.5	4.9	3.7	0	1	0	0	2	0	16	3	13	2	0	0	0	17	0.5	3	36	3	6	0	0	0	0	100.0	21	n.d.	1	76%	15%	1%	1%	0%	5%	2%	0.4%	0%	0%	0%	1%	100%
(beach)	Foz do Cunene	S5053	<500	0%	44%	56%	Point	203	1375	S.Andò	14.2	8.3	17.7	10.3	0	0.5	0	0	1	0.5	12	6	23	0.5	0	0	0	16	1	1	33	0	3	0.5	0	0	0	100.0	26	n.d.	0	58%	33%	1%	1%	0%	5%	0%	0.6%	0%	1%	0%	1%	100%
HOARUSIB & CUNENE RIVER SYSTEM																																																						
Hoarusib	Purros	S3938	32-500	0.02%	96%	4%	Area	244	420	M.Padoan	2.2	1.3	5.5	3.2	2	0.4	0	0.8	0	0	67	0	4	0	0	0	0.4	26	0	0	0	0	0	0	0	0	0	100.0	14	n.d.	2	58%	23%	1%	0%	9%	0%	0%	0%	0%	6%	0%	3%	100%
Cunene	Matala	S4773	15-500	2.2%	69%	29%	Point	200	269	S.Andò	0.2	0.1	0.4	0.2	89	1	3	0	2	0.5	2	0	0	0.5	0	0.5	0	1	0	0	1	0	0	0	0	0	0	100.0	n.d.	n.d.	93	57%	27%	5%	1%	1%	0%	5%	0%	1%	0%	0%	3%	100%
Mucope	Techiulo	S5049	15-500	1.9%	91%	8%	Point	213	307	M.Padoan	0.04	0.02	0.13	0.06	50	23	4	0.9	0	1	8	0.5	0	5	4	2	0	0.9	0	0	0	0	0	0	0	0	0	100.0	n.d.	50	78	45%	48%	0%	1%	0%	2%	3%	0%	0%	0%	0%	1%	100%
Caculuvar	Techango	S5050	15-500	0.4%	55%	45%	Area	234	262	M.Padoan	0.04	0.01	0.14	0.02	48	8	4	0	0	2	24	1	2	3	7	1	0	1	0	0.4	0	0	0	0	0	0	0	100.0	n.d.	50	59	17%	73%	0%	0%	0%	4%	6%	0%	0%	1%	0%	0%	100%
Caculuvar confluence	Omutele	S5051	15-500	0.5%	61%	38%	Area	264	246	M.Padoan	0.07	0.03	0.21	0.09	31	2	1	0.4	0	0.4	48	10	0.8	1	0.4	0.8	0	4	0	0.0	0	0	0.8	0	0	0	0	100.0	0	50	33	45%	44%	0%	0%	2%	3%	5%	0%	0%	0%	0%	0%	100%
Cunene	Ruacana	S3931	32-500	0%	100%	0%	Area	212	316	M.Padoan	1.3	0.7	1.6	0.8	2	2	1	2	0	1	32	0	1	0	0.9	0	2	55	0	0	0	0	0	0	0	0	0	100.0	16	86	5	50%	25%	1%	0%	20%	0%	0%	0%	0%	1%	0%	3%	100%
Ehomba	Ehomba	S3932	32-500	0.1%	97%	3%	Area	129	276	M.Padoan	0.6	0.1	0.9	0.2	22	5	5	10	0	0	27	0	4	0	0	0.8	0	26	0	0	0	0	0	0	0	0	0	100.0	34	n.d.	33	19%	42%	4%	0%	29%	0%	0%	0%	0%	0%	0%	5%	100%
Ondoto	Chitado	S3933	32-500	0.1%	86%	14%	Area	201	290	M.Padoan	2.0	0.8	4.3	1.8	7	1	3	2	0	0	52	0	4	0	0	0	0.5	30	0	0	0	0	0	0	0	0	0	100.0	34	n.d.	11	42%	31%	0%	0%	22%	0%	0%	0%	0%	1%	0%	5%	100%
Omuhongo	Etengua	S3935	32-500	0%	27%	73%	Area	200	254	M.Padoan	1.8	1.0	3.3	1.9	5	0	0.5	0	0	0	83	0	2	0	0	0	2	9	0	0	0	0	0	0	0	0	0	100.0	22	n.d.	6	57%	15%	1%	0%	26%	0%	0%	0%	0%	0%	0%	1%	100%
Omuhongo	Oryeheke	S3934	32-500	0%	75%	25%	Area	254	306	M.Padoan	3.8	2.2	7.5	4.3	5	0	0	0	0	0.4	63	0	2	0	0	0	0.8	26	0	0	3	0	0	0	0	0	0	100.0	26	n.d.	5	58%	22%	0%	0%	18%	0%	0%	0%	0%	1%	0%	1%	100%
Cunene	Epupa Falls	S4775	15-500	0.3%	52%	48%	Point	200	590	S.Andò	4.7	3.0	6.8	4.3	0.5	0	0	0	0.5	4	21	7	0.5	0	0.5	0	0	36	3	6	13	2	9	0	0.5	0	0.5	100.0	38	n.d.	1	63%	16%	1%	1%	1%	12%	5%	0%	0%	1%	0%	0%	100%
Otjinjange	Van Zyl's Pass	S3936	32-500	0.1%	98%	2%	Area	215	420	M.Padoan	11.7	8.6	17.0	12.5	0.5	0.5	0	0	0	0	32	0	0.5	0	0	0	0.5	67	0	0	0	0	0	0	0	0	0	100.0	4	n.d.	1	74%	11%	0%	0%	12%	0%	0%	0%	1%	1%	0%	1%	100%
Marienfluss	Otyoyonoka	S3937	32-500	0.6%	64%	36%	Area	217	349	M.Padoan	19.6	15.4	22.3	17.5	1	0	0	0	0	0	23	0	0.5	0	0	0	1	74	0	0	0	0	0	0	0	0	0	100.0	0	n.d.	1	79%	8%	0%	0%	5%	0%	0%	0%	0%	6%	0%	2%	100%
Cunene	Foz do Cunene	S5052	15-500	0%	95%	5%	Point	216	478	S.Andò	5.6	4.2	5.4	4.1	0.5	0	0.5	0	2	0.9	14	6	10	4	0.9	0	0.5	29	0.5	4	20	3	6	0	0	0	0	100.0	9	54	1	76%	8%	2%	1%	0%	11%	0%	1%	0%	1%	0%	0%	100%
OFFSHORE CORE TOP SAMPLES																																																						
ORANGE LITTORAL CELL OFFSHORE																																																						
-2766 m c'tl rise offshore Baia dos Tigres		1/1 89-91	> 5	91%	9%	0%	Raman	202	374	M.Limonta	n.d.	n.d.	1.6	0.9	2.5	1.5	0.0	1.0	3.0	0.5	14.9	0.0	1.0	0.0	0.0	0.0	0.0	7.9	0.0	0.0	64.4	0.0	3.0	0.0	0.0	0.0	0.5	100.0	0	n.d.	4	54%	5%	0%	1%	0%	0%	27%	1%	0%	8%	0%	5%	100%
-2768 m c'tl rise offshore Baia dos Tigres		2/4 31-33	> 5	92%	8%	0%	Raman	200	385	M.Limonta	n.d.	n.d.	1.0	0.5	3.0	0.0	0.0	1.0	4.0	5.0	20.5	0.0	7.5	0.5	1.0	1.0	0.0	19.0	0.0	0.0	36.5	0.0	0.0	0.0	0.0	0.0	1.0	100.0	0	n.d.	3	52%	2%	2%	2%	0%	2%	23%	2%	0%	10%	1%	4%	100%
-2766 m c'tl rise offshore Baia dos Tigres		1/6 65-67	> 5	92%	8%	0%	Raman	205	424	M.Limonta	n.d.	n.d.	1.0	0.5	2.9	1.5	2.0	0.0	2.4	2.9	21.5	0.0	1.5	0.0	0.0	0.0	0.0	18.5	0.0	0.0	42.9	0.0	2.0	0.0	0.0	0.0	2.0	100.0	0	n.d.	6	48%	1%	1%	2%	0%	0%	28%	0%	0%	14%	2%	4%	100%
-75 m shelf offshore of Cunene mouth		1019	>15	46%	54%	0%	Raman	200	257	M.Limonta	n.d.	n.d.	7.5	5.9	0.5	0.5	1.0	0.5	4.5	2.0	10.0	0.0	1.5	0.0	0.5	0.0	0.0	11.0	0.0	0.0	66.5	0.0	0.5	0.0	0.0	0.0	1.0	100.0	0	n.d.	2	78%	1%	0%	0%	0%	0%	11%	0%	0%	5%	0%	4%	100%
-110 m outer shelf offshore of Cunene mouth		1020	>15	29%	71%	0%	Raman	201	256	M.Limonta	8.6	6.7	8.6	6.7	1.5	0.5	0.5	0.5	2.5	4.0	10.9	0.0	6.0	0.5	0.0	0.0	0.0	10.9	0.0	0.0	62.2	0.0	0.0	0.0	0.0	0.0	0.0	100.0	0	n.d.	2	79%	1%	0%	0%	0%	1%	15%	1%	0%	2%	0%	1%	100%
-173 m outer shelf offshore of Cunene mouth		1021	>15	15%	85%	0%	Raman	203	248	M.Limonta	5.9	4.8	5.9	4.8	0.0	0.0	2.0	1.0	2.5	2.0	13.8	0.0	1.5	0.0	0.0	0.0	0.5	6.9	0.0	0.0	70.0	0.0	0.0	0.0	0.0	0.0	0.0	100.0	n.d.	n.d.	2	82%	1%	0%	0%	0%	0%	10%	1%	0%	3%	0%	3%	100%
-551 m slope offshore of Cunene mouth		1022	>15	3%	97%	0%	Raman	198	244	M.Limonta	n.d.	n.d.	0.8	0.7	2.5	1.5	1.5	0.0	2.0	2.0	17.2	0.0	5.1	1.0	0.5	0.0	1.0	5.1	0.0	0.0	60.6	0.0	0.0	0.0	0.0	0.0	0.0	100.0	n.d.	70	6	81%	2%	0%	0%	0%	0%	11%	1%	0%	2%	0%	3%	100%
-399 m continental slope on Walvis Ridge		1704	>15	70%	30%	0%	Raman	208	274	M.Limonta	n.d.	n.d.	0.3	0.2	0.5	0.0	0.0	0.0	3.4	1.4	14.9	0.0	1.4	0.0	0.0	0.0	0.0	9.6	0.0	0.0	68.8	0.0	0.0	0.0	0.0	0.0	0.0	100.0	2	n.d.	0	76%	1%	0%	0%	0%	0%	8%	0.4%	2%	4%	8%	1%	100%
-642 m continental slope on Walvis Ridge		1705	>15	74%	26%	0%	Raman	164	203	M.Limonta	n.d.	n.d.	1.0	0.8	1.2	0.0	0.0	3.7	1.2	0.0	20.7	0.0	3.0	0.0	0.6	0.0	0.0	17.7	0.0	0.0	51.8	0.0	0.0	0.0	0.0	0.0	0.0	100.0	10	n.d.	1	81%	0%	0%	1%	0%	1%	11%	0%	0%	3%	0%	1%	100%

Table A4

Sample	Sediment	Site	points	Operator	quartz	K-feldspar	plagioclase	rock fragments	mica	magnetite*	ilmenite*	chromite	monazite	zircon	rutile	garnet	staurolite	titanite	epidote	clinopyroxene	hypersthene	amphibole	& tHM		glaucony	carbonates	sulphates	C organic	HMC	tHMC
P4948	*foreshore beach placer*	Bentiaba	3598	F.Crotti	1.1	0.3	0.5	1.2	0	76	12	0.5	0.6	2.8	0.6	0.4	0	0.5	1.9	0.0	0.01	0.7	0.01	100.0	0	0	1.0	0	97	7.7
P4958	*foreshore beach placer*	Vanesinha	3710	F.Crotti	0.5	0.1	0.1	0.5	0	53	6.6	1.6	0.3	2.0	0.4	32	0.4	0.2	0.8	0.9	0.1	0.1	0.5	100.0	0.03	0	0.3	1.0	99	37
P4959	*foreshore beach placer*	Praia do Navic	2381	F.Crotti	1.8	0.2	0.4	1.9	0	36	4.2	1.6	0.3	1.0	1.0	48	1.2	0.5	0.6	0.8	0.5	0.2	0.02	100.0	0.2	0	0	0.4	96	54
P4336	*foreshore beach placer*	Shawnee	200	L.Borromeo	25	1.0	6.0	5.5	0	27	2.0	0.01	0	4.0	0	8.5	0	0.5	1.5	18	0	0	0	100.0	0	0	0	0	62	32
P4330	*foreshore beach placer*	Bayview	300	L.Borromeo	8.1	0.7	3.4	3.0	0	13	1.4	0.1	0	1.0	0	49	1.3	0.3	1.3	16	0.3	0.7	0	100.0	0	0	0	0	85	70

Opaque Fe-Ti-Cr oxides					magnetite	magnetite/hematite	martite	hematite	hematite/ilmenite	ilmenite	leucoxene	chromite	goethite	limonite	Fe-Al hydroxide	
P4948	*foreshore beach placer*	Bentiaba	167	F.Crotti	30	17	31	8	0	14	0	0.6	0	0	0	100.0
P4958	*foreshore beach placer*	Vanesinha	155	F.Crotti	16	3	27	6	2	8	1	3	11	13	9	100.0
P4959	*foreshore beach placer*	Praia do Navic	79	F.Crotti	23	5	46	13	0	10	0	4	0	0	0	100.0

Table A5

	NAM13		S4358		Meteor M6/6 Site GeoB1074		Meteor M6/6 Site GeoB1019		Meteor M6/6 Site GeoB1020		Meteor M6/6 Site GeoB1021		Meteor M6/6 Site GeoB1022		ODP Leg 175 Site 1080A 1/1 89-91		ODP Leg 175 Site 1080A 2/4 31-33		ODP Leg 175 Site 1080B 1/6 65-67		S4958 + S4959	
	Orange River mouth @ Alexander Bay		*Mowe Bay dune*		*Walvis Ridge (-399 m)*		*offshore Cunene mouth (-79 m)*		*offshore Cunene mouth (-110 m)*		*offshore Cunene mouth (-173 m)*		*offshore Cunene mouth (-551 m)*		*offshore Baia dos Tigres (-2766 m)*		*offshore Baia dos Tigres (-2766 m)*		*offshore Baia dos Tigres (-2766 m)*		*Vanesinha + Praia do Navio beach placers*	
Augite	54	**78%**	39	**78%**	25	**30%**	99	**76%**	81	**65%**	86	**61%**	59	**50%**	77	**61%**	46	**74%**	51	**60%**	3	50%
Diopside	9	**13%**	4	**8%**	55	**66%**	15	**12%**	26	**21%**	39	**28%**	39	**33%**	31	**25%**	12	**19%**	21	**25%**	1	17%
Pigeonite	3	**4%**	3	**6%**	2	**2%**	11	**8%**	9	**7%**	6	**4%**	13	**11%**	10	**8%**	2	**3%**	4	**5%**	0	0%
Orthopyroxene	2	**3%**	1	**2%**	0	**0%**	4	**3%**	5	**4%**	4	**3%**	1	**1%**	7	**6%**	0	**0%**	7	**8%**	2	33%
Pyroxene n.d.	0	**0%**	0	**0%**	0	**0%**	0	**0%**	0	**0%**	0	**0%**	3	**3%**	0	**0%**	0	**0%**	0	**0%**	0	0%
Pyroxenoids	1	**1%**	3	**6%**	1	**1%**	1	**1%**	3	**2%**	5	**4%**	3	**3%**	1	**1%**	2	**3%**	2	**2%**	0	0%
TOTAL	**69**		**50**		**83**		**130**		**124**		**140**		**118**		**126**		**62**		**85**		**6**	

NAM13

grain #	Name	diagnostic peaks	
1	Hypersthene	661, 676	1005
2	Augite	662	995
3	Augite	667	1001
4	Augite	662	1005
5	Augite	665	1011
6	Augite	664	1007
7	Augite	664	1009
8	Augite	665	1009
9	Pigeonite	654, 671	999, 1012
10	Augite	662	1005
11	Diopside	667	1012
12	Pigeonite	656, 669	996, 1011
13	Diopside	667	1013
14	Augite	665	1010
15	Diopside	667	1012
16	Diopside	667	1012
17	Diopside	667	1011
18	Diopside	667	1011
19	Augite	665	1011
20	Augite	665	1010
21	Diopside	667	1012
22	Augite	663	1007
23	Pigeonite	657, 671	998, 1010
24	Augite	661	1004
25	Augite	662	1004
26	Hypersthene	663, 678	1002
27	Augite	659	1005
28	Augite	661	1003
29	Diopside	667	1011
30	Augite	666	1011
31	Augite	666	1011
32	Augite	664	1010
33	Augite	663	1007
34	Augite	662	1004
35	Augite	666	1011
36	Augite	664	1009
37	Augite	659	995
38	Augite	650	993
39	Augite	664	1008
40	Augite	660	1003
41	Augite	665	1005
42	Augite	655	987
43	Augite	655	996
44	Augite	663	1005
45	Augite	664	1006
46	Augite	665	1010
47	Augite	660	998
48	Augite	664	1006
49	Augite	659	1000
50	Augite	665	1008
51	Augite	654	993
52	Augite	658	1000
53	Augite	660	1001
54	Augite	664	1008
55	Augite	662	1005
56	Pyroxenoid	661	988, 1006
57	Augite	664	1008
58	Augite	665	1009
59	Augite	662	995
60	Augite	663	1006
61	Augite	662	1006
62	Augite	656	997
63	Diopside	666	1011
64	Augite	662	1005
65	Augite	663	1007
66	Augite	663	1006
67	Augite	660	1003
68	Augite	661	1004
69	Augite	664	1009

S4358

grain #	Name	diagnostic peaks	
1	Augite	663	1009
2	Augite	665	1009
3	Augite	663	995
4	Pigeonite	658, 674	998, 1013
5	Augite	665	1009
6	Augite	665	1009
7	Augite	661	1005
8	Augite	654	991
9	Augite	665	1009
10	Diopside	664	1012
11	Augite	666	1010
12	Pyroxenoid	662	991, 1006
13	Augite	665	1010
14	Augite	665	1010
15	Augite	660	1002
16	Augite	661	1004
17	Augite	665	1011
18	Augite	659	1000
19	Augite	666	1011
20	Diopside	667	1012
21	Augite	666	1011
22	Augite	656	996
23	Augite	667	1006
24	Augite	658	992
25	Augite	666	1011
26	Augite	658	998
27	Augite	666	1011
28	Diopside	667	1011
29	Augite	666	1011
30	Pigeonite	657, 673	999, 1015
31	Hypersthene	659.673	1002
32	Pyroxenoid	665	998, 1009
33	Augite	664	1008
34	Augite	661	1009
35	Augite	666	1011
36	Diopside	667	1011
37	Pyroxenoid	665	995, 1011
38	Augite	666	1011
39	Augite	665	1010
40	Augite	666	1010
41	Augite	665	1009
42	Augite	665	1009
43	Augite	666	1011
44	Augite	665	1009
45	Pigeonite	657, 669	998, 1010
46	Augite	663	1007
47	Augite	660	1003
48	Augite	664	1007
49	Augite	664	1008
50	Augite	666	1010

Meteor M6/6 Site GeoB1074

grain #	Name	diagnostic peaks	
4	Augite	666	1011
8	Diopside	667	1012
9	Diopside	667	1012
10	Diopside	667	1013
12	Diopside	667	1012
14	Diopside	667	1013
16	Diopside	667	1012
18	Augite	665	1010
19	Diopside	667	1012
20	Augite	666	1010
21	Augite	666	1011
24	Augite	665	1005
26	Pyroxenoid	666	998, 1012
27	Diopside	667	1013
30	Diopside	667	1013
31	Augite	666	1011
33	Diopside	667	1012
34	Diopside	667	1013
35	Diopside	666	1012
38	Diopside	667	1013
39	Diopside	667	1012
41	Diopside	667	1013
42	Augite	665	1009
43	Diopside	667	1012
46	Augite	665	1004
47	Diopside	667	1014
49	Diopside	667	1013
50	Diopside	667	1013
52	Diopside	667	1012
55	Diopside	667	1013
56	Diopside	667	1012
58	Diopside	667	1012
60	Diopside	667	1012
61	Diopside	667	1012
62	Diopside	667	1012
64	Diopside	667	1013
65	Augite	664	1009
67	Augite	664	1009
68	Augite	665	1009
70	Augite	664	1008
71	Diopside	667	1013
72	Diopside	667	1013
73	Diopside	667	1013
74	Augite	663	1008
75	Diopside	667	1012
76	Diopside	667	1012
77	Diopside	667	1012
78	Augite	664	1010
79	Diopside	667	1012
80	Diopside	667	1011
83	Diopside	667	1012
84	Diopside	667	1012
85	Diopside	667	1012
93	Diopside	667	1013
94	Diopside	667	1012
95	Augite	664	1006
96	Augite	666	1011
97	Diopside	667	1011
98	Diopside	667	1011
99	Diopside	667	1013
101	Pigeonite	659, 671	999, 1012
103	Augite	664	1009
106	Augite	666	1011
111	Pigeonite	650, 668	994, 1012
112	Augite	662	1004
115	Augite	664	1000
116	Augite	666	1011
117	Augite	666	1011
121	Diopside	667	1011
123	Diopside	667	1011
127	Diopside	667	1011
129	Diopside	667	1011
132	Diopside	667	1012
133	Diopside	667	1012
134	Diopside	667	1012
136	Diopside	667	1011
137	Diopside	667	1011
139	Augite	666	1011
141	Augite	664	1009
142	Augite	664	1009
143	Diopside	667	1012
144	Diopside	667	1011
145	Diopside	667	1011

Meteor M6/6 Site GeoB1019

grain #	Name	diagnostic peaks	
1	Augite	665	997
4	Augite	666	1009
5	Hypersthene	658, 673	1004
7	Augite	664	1008
8	Augite	661	996
10	Augite	663	1007
12	Augite	665	1008
13	Diopside	666	1012
17	Pigeonite	659, 672	999, 1012
18	Augite	665	1008
19	Augite	666	1011
28	Augite	663	1008
29	Pigeonite	657, 673	998, 1013
30	Augite	663	1004
31	Augite	666	1011
32	Augite	661	1004
35	Augite	661	1007
36	Augite	666	1011
37	Enstatite	661, 678	1009, 1024
38	Augite	665	1011
39	Augite	666	1011
40	Augite	666	1011
41	Augite	661	1005
42	Pigeonite	655, 667	998, 1010
43	Augite	664	1008
44	Augite	664	1008
45	Augite	664	1007
46	Augite	658	1001
48	Augite	658	999
49	Augite	663	1005
51	Augite	661	1005
54	Augite	660	1005
56	Diopside	666	1012
57	Diopside	666	1012
58	Augite	664	1008
61	Pigeonite	656, 671	995, 1011
62	Augite	658	998
63	Augite	662	1006
64	Augite	662	1003
66	Augite	655	998
67	Diopside	667	1011
68	Augite	656	997
70	Pigeonite	656, 670	998, 1010
71	Augite	663	1008
72	Augite	666	1011
73	Augite	662	1005
75	Hypersthene	657, 670	1000
76	Augite	667	1001
77	Augite	664	1008
78	Augite	666	1010
79	Augite	664	1007
81	Hypersthene	659, 674	1002
83	Augite	657	998
84	Augite	665	1011
85	Diopside	667	1011
87	Pigeonite	660, 674	999, 1012
88	Augite	657	998
90	Augite	658	1000
91	Augite	665	996
92	Diopside	667	1011
94	Augite	665	1008
95	Augite	666	1006
96	Augite	661	1004
98	Augite	664	1006
99	Pigeonite	657.671	998, 1012
101	Augite	662	1008
102	Pigeonite	655, 670	999, 1011
103	Augite	662	1006
106	Augite	661	1007
110	Augite	666	1011
111	Augite	666	1010
112	Augite	659	998
113	Augite	664	1006
114	Augite	660	995
115	Pigeonite	657, 671	998, 1012
116	Augite	665	1010
117	Augite	666	1011
118	Augite	665	1010
119	Augite	664	1008
120	Augite	665	1008
121	Augite	666	1010
122	Augite	664	1009
124	Augite	655	998
125	Augite	666	1011
127	Augite	665	1008
130	Pyroxenoid	662	993, 1007
131	Augite	663	1007
132	Augite	656	997
134	Augite	661	1001
136	Augite	665	1008
137	Pigeonite	653, 665	994, 1008
141	Diopside	667	1011
142	Diopside	667	1011
143	Augite	661	1004
144	Augite	664	1008
146	Diopside	666	1013
147	Augite	666	1011
151	Augite	666	1011
152	Augite	658	1001
153	Augite	663	1007
154	Augite	661	996
155	Diopside	667	1011
156	Augite	662	1007
159	Augite	664	1008
160	Augite	666	1011
164	Augite	660	1001
167	Augite	666	1011
169	Augite	663	1005
170	Augite	666	1010
171	Augite	665	1009
172	Augite	666	1010
173	Augite	666	1010
175	Augite	666	1010
176	Augite	665	1009
178	Augite	660	1003
179	Augite	657	999
180	Diopside	666	1013
183	Augite	662	1006
184	Augite	655	997
185	Augite	666	1010
186	Diopside	667	1011
187	Augite	666	1011
192	Augite	662	1006
193	Diopside	667	1011
194	Augite	665	1010
195	Augite	664	1009
196	Diopside	667	1012
197	Diopside	667	1012
198	Pigeonite	658, 669	994, 1010
200	Augite	658	999

Meteor M6/6 Site GeoB1020

grain #	Name	diagnostic peaks	
1	Augite	666	1011
3	Augite	658	1001
4	Augite	666	1011
5	Augite	666	1011
8	Augite	666	1011
9	Augite	660	1000
10	Augite	666	1011
11	Diopside	667	1011
12	Diopside	667	1012
14	Diopside	667	1012
15	Augite	666	1009
16	Augite	662	1004
17	Hypersthene	659, 678	1001
20	Hypersthene	659, 676	1003
21	Augite	666	1011
22	Augite	662	1004
23	Augite	666	1008
24	Augite	664	1008
25	Augite	664	1008
26	Augite	666	1011
30	Diopside	666	1012
32	Pigeonite	657, 672	998, 1010
33	Diopside	667	1012
34	Augite	666	1011
37	Augite	665	1007
38	Augite	665	1010
42	Pigeonite	659, 668	997, 1013
43	Augite	662	997
44	Pigeonite	656, 671	998, 1013
45	Augite	663	1007
46	Augite	660	1001
47	Diopside	666	1012
48	Augite	663	1006
49	Augite	657	997
50	Augite	665	1011
51	Augite	660	990
53	Pigeonite	657, 669	996, 1009
54	Augite	666	1011
57	Augite	665	1007
60	Augite	662	1006
63	Augite	666	1010
64	Augite	665	1008
65	Pigeonite	659, 669	994, 1009
68	Diopside	667	1011
70	Augite	659	998
71	Augite	666	1011
73	Diopside	667	1011
74	Pigeonite	658, 669	998, 1012
75	Augite	666	1010
76	Augite	665	1009
80	Augite	661	1003
82	Diopside	667	1011
84	Diopside	667	1011
86	Diopside	666	1012
87	Pigeonite	659, 670	995, 1010
89	Augite	658	995
90	Diopside	667	1011
92	Diopside	667	1011
93	Augite	665	1008
94	Augite	665	1008
96	Diopside	667	1011
100	Diopside	667	1012
101	Diopside	667	1012
102	Augite	653	991
103	Diopside	667	1014
105	Augite	665	1009
106	Augite	664	1009
107	Diopside	667	1011
110	Augite	664	1006
111	Diopside	667	1012
112	Rhodonite	667	1000, 1015
118	Augite	666	1009
119	Augite	663	1009
121	Augite	666	1011
123	Augite	665	1009
125	Hypersthene	659, 674	1001
131	Augite	666	1011
132	Diopside	667	1012
135	Augite	663	1000
137	Augite	664	1007
138	Pyroxenoid	666	997, 1010
139	Augite	658	999
141	Diopside	667	1011
142	Augite	665	1009
143	Diopside	667	1011
144	Augite	663	1006
145	Hypersthene	660, 675	1002
146	Augite	666	1010
148	Augite	666	1010
150	Augite	659	998
152	Diopside	667	1012
154	Augite	666	1010
157	Augite	660	1002
159	Augite	662	1000
160	Augite	662	1004
164	Augite	666	1011
165	Diopside	667	1012
168	Augite	666	1010
169	Diopside	667	1012
170	Augite	660	999
171	Hypersthene	659, 675	1004
172	Pyroxenoid	664	994, 1009
174	Augite	664	1007
176	Augite	665	1011
177	Pigeonite	658, 672	999, 1012
178	Diopside	666	1013
180	Augite	663	1009
181	Augite	660	1004
183	Augite	665	1009
184	Augite	663	1007
186	Augite	664	1007
187	Augite	663	1007
188	Augite	662	1006
189	Augite	664	1008
192	Augite	666	1011
193	Augite	656	996
194	Augite	665	1011
195	Augite	665	1010
196	Augite	663	1008
197	Augite	663	1007
198	Pigeonite	657, 673	998, 1013
201	Augite	666	1011
203	Augite	666	1011
205	Augite	666	1010

Meteor M6/6 Site GeoB1021

grain #	Name	diagnostic peaks	
2	Augite	665	1008
4	Diopside	666	1012
5	Augite	664	1007
6	Augite	664	1008
7	Diopside	667	1013
8	Augite	665	1011
9	Diopside	667	1012
11	Diopside	667	1011
12	Diopside	667	1012
14	Diopside	667	1011
16	Pigeonite	657, 671	999, 1013
17	Augite	665	1011
18	Diopside	667	1012
24	Diopside	666	1012
25	Diopside	667	1012
26	Diopside	667	1012
27	Augite	666	1009
28	Diopside	667	1012
30	Diopside	667	1012
31	Pigeonite	658, 672	997, 1013
32	Diopside	667	1012
33	Augite	665	1010
34	Augite	666	1007
35	Hypersthene	658, 674	1003
36	Augite	666	1011
37	Diopside	667	1012
39	Augite	662	1005
41	Augite	665	1008
44	Augite	665	1010
45	Augite	666	1010
46	Augite	666	1010
47	Diopside	667	1012
49	Augite	666	1008
50	Pyroxenoid	666	997, 1009
51	Augite	666	1011
53	Diopside	667	1012
54	Augite	663	1004
55	Diopside	667	1011
56	Diopside	667	1011
57	Augite	664	1006
58	Augite	661	1004
59	Hypersthene	658, 676	1003
61	Diopside	667	1012
62	Hypersthene	657, 677	1004
63	Diopside	667	1011
64	Diopside	667	1013
65	Augite	664	1005
67	Augite	665	1010
68	Pigeonite	658, 671	998, 1015
69	Augite	665	1010
72	Diopside	667	1012
73	Pigeonite	653, 669	998, 1013
74	Diopside	667	1012
76	Augite	666	1011
79	Augite	664	1008
80	Diopside	666	1012
81	Diopside	667	1012
83	Diopside	666	1012
84	Pyroxenoid	666	1001, 1010
85	Diopside	666	1012
87	Augite	660	1002
88	Augite	664	995
89	Pigeonite	659, 672	999, 1012
90	Diopside	667	1012
93	Augite	664	1008
95	Diopside	667	1011
96	Augite	661	1005
97	Augite	664	1008
99	Diopside	667	1011
103	Augite	666	1011
105	Augite	666	1011
106	Augite	666	1011
107	Augite	663	1006
108	Augite	666	1009
110	Pyroxenoid	666	998, 1014
111	Augite	665	1009
112	Augite	666	1010
113	Augite	666	1008
116	Augite	665	1010
117	Augite	664	1006
118	Pyroxenoid	664	995, 1006
119	Augite	663	1004
120	Augite	662	1003
121	Augite	663	1009
122	Augite	666	1010
123	Augite	666	1011
124	Diopside	667	1012
125	Augite	666	1011
126	Augite	660	1003
128	Augite	666	1011
129	Augite	664	1009
130	Augite	666	1010
131	Augite	663	1008
132	Diopside	666	1012
133	Augite	663	1007
140	Augite	661	1002
144	Augite	664	1009
145	Augite	666	1007
147	Augite	662	1007
148	Augite	666	1000
150	Augite	666	1002
152	Augite	666	1011
153	Augite	666	1011
154	Augite	665	1010
156	Diopside	667	1012
158	Augite	667	1002
159	Augite	666	1010
161	Augite	665	1010
162	Augite	665	1008
164	Augite	665	1010
165	Diopside	667	1011
167	Augite	666	1014
168	Augite	666	1010
169	Diopside	667	1011
172	Augite	666	1011
176	Augite	665	1010
177	Augite	666	1011
178	Augite	666	1011
179	Augite	662	1005
180	Augite	665	1008
182	Diopside	666	1012
183	Augite	666	1011
184	Augite	662	1003
185	Augite	665	1009
186	Augite	665	1010
187	Augite	666	1011
189	Augite	665	1010
190	Augite	666	1009
191	Augite	666	1011
192	Augite	666	1011
194	Hypersthene	657, 673	1002
195	Diopside	667	1012
196	Pigeonite	658, 672	998, 1012
197	Augite	665	1009
198	Diopside	667	1011
199	Augite	665	1009
200	Diopside	666	1012
205	Augite	662	1004
207	Augite	664	1007
208	Pyroxenoid	664	995, 1007

Meteor M6/6 Site GeoB1022

grain #	Name	diagnostic peaks	
4	Augite	666	1011
6	Augite	666	1011
7	Augite	666	1011
8	Diopside	667	1011
10	Diopside	667	1011
11	Diopside	666	1012
12	Augite	665	1010
13	Diopside	666	1013
14	Augite	665	1009
15	Diopside	665	1013
16	Diopside	666	1013
18	Hypersthene	656, 671	1001
20	Augite	664	1009
21	Pigeonite	657, 670	999, 1013
22	Pigeonite	658, 671	996, 1011
23	Augite	666	1011
24	Diopside	666	1012
25	Diopside	666	1012
28	Augite	663	1007
29	Augite	666	1011
34	Pigeonite	658, 673	999, 1011
35	Pyroxenoid	664	994, 1008
36	Augite	666	1010
37	Augite	665	1007
38	Pigeonite	656, 671	998, 1011
40	Diopside	667	1011
43	Diopside	666	1012
44	Augite	662	1000
48	Pigeonite	657, 671	998, 1011
51	Diopside	666	1012
55	Augite	664	1008
58	Pigeonite	656, 669	995, 1010
59	Augite	665	1011
60	Augite	666	1011
61	Augite	665	1010
62	Augite	666	1010
64	Diopside	667	1011
65	Augite	665	1010
66	Augite	666	1008
68	Augite	666	1011
70	Augite	666	1011
71	Augite	666	1011
73	Augite	665	1009
74	Augite	663	1008
75	Augite	665	1010
76	Diopside	666	1012
78	Diopside	666	1012
79	Diopside	666	1012
80	Pigeonite	659, 674	998, 1011
81	Augite	664	1008
84	Augite	665	1009
86	Diopside	666	1012
88	Diopside	666	1012
89	Pigeonite	660, 674	1000, 1012
94	Augite	666	1003
95	Augite	666	1011
96	Augite	665	1009
97	Diopside	666	1012
100	Augite	666	1011
103	Diopside	667	1012
105	Augite	665	1011
106	Pigeonite	658, 674	1000, 1014
111	Augite	664	1008
116	Augite	666	1011
119	Diopside	667	1011
120	Pyroxene		n.d.
121	Augite	666	1011
123	Augite	666	1011
125	Diopside	667	1011
126	Diopside	667	1012
127	Diopside	667	1012
128	Augite	665	1008
129	Diopside	667	1012
130	Augite	666	1010
133	Augite	667	1010
134	Pigeonite	657, 671	999, 1012
136	Diopside	667	1011
138	Augite	666	1011
141	Augite	662	1005
142	Augite	665	1010
143	Augite	666	1011
145	Diopside	667	1013
147	Augite	666	1009
149	Pyroxene		n.d.
151	Diopside	667	1012
153	Diopside	667	1012
154	Augite	664	1004
155	Augite	664	1007
156	Augite	664	1006
157	Augite	665	1009
158	Diopside	666	1012
159	Pigeonite	659, 674	999, 1012
160	Augite	666	1011
162	Diopside	667	1011
164	Diopside	667	1013
166	Augite	664	1009
167	Augite	666	1010
169	Pigeonite	657, 671	999, 1014
170	Diopside	667	1012
171	Pyroxene		n.d.
172	Diopside	667	1011
174	Diopside	667	1012
175	Pyroxenoid	656	996, 1005
176	Diopside	667	1013
177	Diopside	667	1013
178	Augite	665	1011
183	Augite	663	990
187	Diopside	667	1011
188	Diopside	667	1011
189	Diopside	667	1011
190	Pyroxenoid	666	995, 1010
192	Pigeonite	657, 672	998, 1012
193	Augite	666	1010
195	Augite	665	1010
196	Augite	661	996
198	Augite	665	1010
200	Augite	667	1007
201	Augite	665	1011

ODP Leg 175 Site 1080A 1/1 89-91

grain #	Name	diagnostic peaks	
2	Diopside	667	1011
3	Pigeonite	656, 672	999, 1011
5	Augite	666	1011
9	Diopside	667	1011
12	Augite	664	1009
13	Hypersthene	660, 678	1005
17	Augite	658	1004
18	Augite	666	1000
19	Augite	661	1000
20	Hypersthene	662, 678	1006
21	Augite	663	1007
22	Augite	665	1008
23	Pigeonite	658, 670	999, 1012
24	Diopside	667	1013
27	Augite	665	1010
28	Augite	665	1010
29	Augite	666	1010
30	Augite	666	1008
31	Augite	662	1004
33	Diopside	667	1012
35	Augite	662	1008
36	Hypersthene	662, 679	1006
37	Diopside	667	1011
38	Augite	662	992
39	Augite	659	999
41	Augite	665	1008
43	Augite	664	1004
47	Augite	662	1005
49	Augite	657	989
51	Pyroxenoid	668	1000, 1011
53	Augite	665	1008
54	Hypersthene	660, 679	1007
61	Pigeonite	654, 669	995, 1009
63	Augite	663	1007
66	Augite	665	1007
67	Augite	663	1007
68	Augite	664	1008
73	Diopside	666	1012
74	Hypersthene	659, 677	1005
75	Diopside	667	1011
76	Augite	666	1009
77	Augite	666	998
78	Augite	667	1010
79	Augite	666	1011
80	Diopside	667	1011
83	Diopside	667	1011
84	Augite	665	1009
85	Diopside	667	1011
87	Augite	665	1008
91	Diopside	667	1011
92	Augite	666	1011
93	Augite	666	1011
94	Augite	666	1006
95	Diopside	667	1011
96	Augite	665	1009
97	Augite	665	1009
98	Diopside	667	1011
99	Diopside	667	1011
100	Diopside	665	1011
101	Diopside	667	1011
105	Augite	662	1002
106	Augite	666	1001
107	Diopside	667	1011
108	Augite	659	1000
112	Augite	665	1009
113	Diopside	666	1012
115	Augite	665	1009
119	Diopside	667	1012
120	Pigeonite	652, 668	993, 1011
123	Augite	666	1011
125	Diopside	667	1011
127	Augite	666	1011
130	Augite	666	1011
134	Pigeonite	654, 668	995, 1011
138	Augite	660	1004
139	Diopside	667	1011
144	Augite	664	1004
146	Augite	665	1007
147	Hypersthene	660, 679	1009
151	Augite	663	1008
154	Pigeonite	656, 670	996, 1011
160	Augite	666	1011
161	Augite	660	1001
162	Diopside	667	1012
163	Diopside	666	1012
164	Augite	664	1008
165	Hypersthene	661, 678	1007
166	Augite	660	1004
167	Augite	666	1000
168	Augite	658	1000
169	Augite	665	1010
171	Diopside	665	1012
174	Augite	654	993
177	Augite	664	993
178	Augite	657	990
180	Diopside	667	1011
181	Augite	658	986
182	Diopside	666	1011
183	Augite	664	1007
184	Pigeonite	655, 670	998, 1011
185	Diopside	667	1013
186	Augite	665	1011
187	Augite	665	1009
189	Augite	662	1006
190	Augite	664	1008
191	Augite	666	1010
193	Pigeonite	658, 671	998, 1012
197	Diopside	667	1011
198	Pigeonite	656, 669	998, 1011
199	Augite	664	1011
201	Diopside	666	1012
202	Diopside	667	1012
203	Diopside	667	1011
209	Augite	660	1004
212	Augite	666	1009
213	Augite	665	1009
214	Augite	664	1006
217	Augite	657	996
218	Augite	658	999
221	Augite	666	1011
222	Augite	664	1007
223	Augite	660	1002
224	Augite	665	1010
225	Augite	665	1010
226	Pigeonite	654, 668	996, 1011
228	Augite	664	1009

ODP Leg 175 Site 1080A 2/4 31-33

grain #	Name	diagnostic peaks	
4	Diopside	666	1012
17	Augite	665	1008
18	Augite	665	1008
21	Augite	661	1004
22	Diopside	666	1010
23	Augite	664	1008
26	Diopside	667	1011
29	Augite	666	1009
30	Pigeonite	656, 670	997, 1014
34	Diopside	667	1011
35	Pigeonite	659, 674	999, 1010
44	Augite	666	1010
47	Augite	666	1010
48	Augite	666	1010
50	Augite	661	998
56	Diopside	667	1012
57	Augite	664	1006
58	Diopside	667	1011
59	Augite	660	1001
64	Augite	665	1008
65	Augite	665	1009
66	Augite	666	1009
73	Augite	666	1011
78	Diopside	667	1011
80	Augite	664	1011
84	Pyroxenoid	668	999, 1012
87	Augite	666	1011
89	Augite	664	1007
93	Diopside	667	1013
94	Diopside	667	1013
98	Augite	658	998
100	Augite	664	1007
103	Augite	661	1003
106	Augite	655	994
107	Augite	661	1004
113	Augite	664	1011
114	Augite	664	1008
117	Augite	665	1008
118	Augite	665	1009
120	Augite	665	1010
130	Augite	660	1000
132	Augite	665	1009
133	Augite	661	1002
134	Augite	665	1008
135	Augite	663	1008
138	Augite	664	1007
140	Augite	658	999
145	Augite	664	1008
147	Augite	665	1008
148	Augite	662	1005
151	Augite	661	1004
154	Augite	663	1004
156	Augite	660	1002
164	Pyroxenoid	666	997, 1010
168	Augite	658	1000
172	Augite	663	990
173	Augite	665	1009
178	Diopside	667	1011
179	Diopside	667	1011
189	Augite	658	995
190	Diopside	667	1011
191	Augite	665	1011

ODP Leg 175 Site 1080B 1/6 65-67

grain #	Name	diagnostic peaks	
1	Diopside	667	1011
3	Diopside	668	1011
4	Hypersthene	659, 677	1002
8	Augite	663	1006
11	Fe-hypersthene	655, 673	997
12	Augite	665	1010
16	Diopside	667	1011
18	Hypersthene	660, 673	1002
19	Pigeonite	657, 671	998, 1012
23	Augite	665	1009
25	Augite	664	1008
33	Augite	660	1002
34	Augite	664	1008
37	Diopside	667	1011
39	Augite	660	1004
43	Augite	665	1008
44	Augite	664	1008
46	Augite	661	1007
47	Augite	660	1002
48	Diopside	665	1012
50	Augite	664	1008
54	Diopside	667	1013
56	Augite	665	1009
58	Diopside	667	1011
62	Diopside	667	1012
63	Augite	662	1004
65	Augite	665	1007
66	Diopside	667	1012
70	Augite	666	1011
73	Augite	664	1007
76	Augite	662	1005
79	Diopside	667	1012
83	Pyroxenoid	670	1004, 1016
87	Augite	661	1005
88	Augite	660	1002
93	Diopside	665	1010
94	Augite	665	1009
95	Augite	666	1009
98	Pyroxenoid	666	1001, 10013
99	Augite	664	1009
102	Diopside	666	1012
103	Diopside	666	1012
104	Hypersthene	661, 676	1003
105	Augite	665	1011
107	Augite	665	1008
108	Pigeonite	656, 669	997, 1010
109	Augite	665	1010
110	Augite	665	1009
111	Diopside	667	1011
113	Augite	663	1007
116	Augite	661	1004
119	Hypersthene	660, 678	1004
120	Augite	666	1011
121	Augite	666	1011
123	Diopside	667	1012
125	Augite	666	1011
126	Diopside	667	1012
127	Diopside	667	1011
128	Augite	666	1011
129	Diopside	667	1013
132	Augite	665	1008
138	Augite	662	1005
140	Diopside	666	1012
141	Augite	666	1011
142	Augite	666	1011
143	Augite	666	1011
144	Augite	666	1011
145	Diopside	667	1012
147	Augite	666	1011
151	Diopside	666	1012
152	Augite	666	1010
154	Augite	664	1009
157	Augite	659	1003
162	Augite	665	1010
163	Hypersthene	661, 679	1004
167	Augite	666	1011
168	Augite	666	1011
173	Pigeonite	655, 670	998, 1012
176	Augite	662	1004
179	Pigeonite	657, 672	998, 1011
183	Fe-hypersthene	653, 668	996
184	Augite	665	996
186	Augite	663	993
187	Augite	661	989
188	Augite	661	1004

S4958 + S4959

grain #	Name	diagnostic peaks	
58/95	Augite	664	1010
58/101	Diopside	667	1011
58/137	Augite	664	1009
58/229	Augite	666	1010
59/89	Hypersthene	659, 676	1001
59/106	Hypersthene	660, 678	1004

	Selected Raman peaks (cm^{-1})						Composition from Raman peaks distribution (mol%)				
Grain n°	Peak 1	Peak 2	Peak 3	Peak 4	Peak 5	Peak 6	almandine	pyrope	spessartine	andradite	grossular
Sample P4958 Vanesinha beach placer											
1	214.0	344.3	371.3	554.6	857.7	910.3	72%	0%	26%	2%	0%
4	211.0	344.7	370.2	555.8	861.0	914.4	84%	12%	2%	2%	0%
12	212.5	342.2	369.4	554.2	855.3	909.2	86%	0%	4%	10%	0%
21	214.0	344.9	367.2	555.4	859.1	912.2	86%	6%	2%	6%	0%
22	209.5	347.7	371.7	554.9	854.0	909.6	42%	14%	40%	4%	0%
23	216.9	348.5	375.1	552.8	857.5	904.9	60%	18%	4%	10%	8%
25	206.6	341.9	369.7	556.8	857.7	911.0	86%	0%	14%	0%	0%
27	208.4	343.2	369.1	555.3	856.8	911.9	88%	6%	0%	6%	0%
28	209.6	342.6	370.1	555.3	857.7	911.4	86%	2%	8%	4%	0%
30	210.5	343.7	370.3	554.9	857.7	912.4	84%	8%	2%	6%	0%
31	209.5	345.4	371.0	556.1	860.5	913.6	84%	12%	2%	2%	0%
39	211.2	344.3	370.8	554.0	863.8	908.4	96%	0%	0%	4%	0%
40	217.8	344.0	370.9	555.8	860.5	912.2	90%	2%	2%	0%	6%
42	211.8	343.0	371.5	554.7	862.0	912.6	88%	6%	4%	2%	0%
49	206.3	342.9	373.0	555.5	862.0	912.1	86%	12%	0%	2%	0%
53	212.9	343.1	370.9	556.5	856.3	911.5	72%	0%	28%	0%	0%
55	213.4	343.3	370.3	554.8	857.7	911.0	84%	0%	12%	4%	0%
57	211.5	344.5	370.6	555.5	860.2	914.2	74%	10%	16%	0%	0%
58	214.1	342.8	370.2	554.9	860.5	912.8	96%	0%	2%	2%	0%
59	210.8	343.7	370.2	555.0	859.1	912.6	84%	8%	4%	4%	0%
64	209.9	345.9	371.1	555.0	859.3	913.3	76%	18%	0%	6%	0%
65	212.3	343.4	370.4	555.2	860.3	914.1	88%	8%	0%	4%	0%
75	216.3	348.0	372.8	554.9	863.5	909.9	74%	18%	0%	4%	4%
77	213.2	344.2	371.5	555.7	861.0	914.4	84%	10%	4%	2%	0%
80	214.5	347.5	372.0	554.7	858.5	911.6	58%	20%	16%	6%	0%
98	213.8	344.6	371.9	555.9	861.3	915.3	74%	12%	14%	0%	0%
99	212.7	347.4	372.4	556.1	862.4	915.0	74%	22%	0%	4%	0%
112	217.3	345.6	373.1	556.7	862.8	915.2	80%	16%	0%	0%	4%
113	214.7	346.2	372.9	556.2	863.7	916.3	76%	18%	6%	0%	0%
116	211.3	354.7	372.8	557.3	858.6	913.2	26%	50%	16%	8%	0%
120	215.2	345.4	373.1	556.2	865.3	916.5	84%	16%	0%	0%	0%
122	213.8	348.2	373.6	556.9	863.6	916.8	64%	30%	6%	0%	0%
123	214.0	345.6	373.0	556.6	865.3	916.9	76%	24%	0%	0%	0%
125	214.2	34.6	372.6	556.5	864.8	916.8	100%	0%	0%	0%	0%
128	215.9	346.3	373.0	555.6	861.4	914.2	64%	12%	24%	0%	0%
131	213.8	346.4	373.0	556.9	864.9	917.2	76%	24%	0%	0%	0%
135	217.1	345.7	372.6	555.6	861.1	915.2	62%	14%	24%	0%	0%
136	213.6	346.2	372.3	556.5	865.2	917.3	76%	24%	0%	0%	0%
140	213.9	346.7	373.1	556.7	862.6	916.2	72%	24%	2%	2%	0%
144	224.0	347.1	373.5	556.4	863.2	916.0	74%	18%	0%	0%	8%
145	217.1	347.2	373.0	554.9	860.6	913.1	72%	18%	2%	4%	4%
150	216.1	345.5	372.7	555.9	865.0	916.7	84%	16%	0%	0%	0%
159	216.3	345.7	372.9	556.2	863.0	916.4	76%	18%	4%	2%	0%
164	213.9	346.9	373.0	556.8	864.8	917.7	74%	26%	0%	0%	0%
165	216.9	346.0	373.1	555.8	862.5	914.9	80%	16%	0%	0%	4%
169	214.3	346.9	372.9	556.5	864.6	917.6	74%	26%	0%	0%	0%
177	218.9	354.3	377.6	556.8	858.0	912.5	16%	40%	36%	0%	8%
180	217.4	345.6	373.1	555.2	860.4	914.0	62%	10%	28%	0%	0%
181	217.2	346.7	372.9	555.3	862.2	914.4	72%	20%	2%	4%	2%
182	217.4	343.7	373.1	556.7	864.4	916.4	86%	12%	2%	0%	0%
183	212.8	349.0	373.3	557.6	861.1	918.6	58%	32%	10%	0%	0%
184	214.8	347.0	372.7	556.9	865.0	917.8	75%	25%	0%	0%	0%
202	212.1	348.8	373.5	557.4	864.8	918.5	64%	36%	0%	0%	0%
203	213.4	346.6	372.9	556.7	864.3	917.6	74%	26%	0%	0%	0%
209	215.0	346.0	373.0	556.1	864.4	916.3	76%	18%	6%	0%	0%
211	214.8	345.9	372.4	556.4	864.5	916.9	84%	16%	0%	0%	0%
215	215.5	344.7	373.0	556.3	864.6	916.8	84%	16%	0%	0%	0%
221	215.6	345.2	372.5	556.4	866.9	916.9	84%	16%	0%	0%	0%
225	211.1	349.1	373.4	557.3	864.9	918.8	64%	36%	0%	0%	0%
232	217.8	344.8	372.4	554.5	860.0	912.8	72%	4%	22%	0%	2%
233	213.2	345.6	372.7	555.9	863.5	915.8	74%	24%	0%	2%	0%
234	213.3	346.4	372.6	556.4	864.8	917.0	76%	24%	0%	0%	0%
238	214.5	3,44,4	372.3	555.9	863.4	916.1	86%	10%	4%	0%	0%
244	213.7	346.9	372.8	556.5	865.3	917.3	75%	25%	0%	0%	0%
246	213.8	344.7	372.3	555.5	862.8	916.1	84%	14%	2%	0%	0%
249	214.6	345.8	372.1	556.5	864.6	916.7	84%	16%	0%	0%	0%
259	216.6	344.9	372.8	555.4	860.1	913.5	72%	8%	18%	2%	0%
264	215.2	343.9	371.8	555.1	862.1	915.0	86%	10%	2%	2%	0%
266	214.6	346.0	373.9	556.7	865.6	917.0	76%	24%	0%	0%	0%
269	212.9	346.6	372.2	556.1	863.6	916.7	72%	26%	0%	2%	0%
270	213.9	345.0	371.6	555.6	864.9	916.8	84%	16%	0%	0%	0%
Sample P4959 - Praia do Navio beach placer											
3	214.1	344.5	371.7	555.6	864.9	916.2	84%	16%	0%	0%	0%
4	215.2	346.6	372.3	555.5	861.8	915.1	72%	22%	2%	4%	0%
12	214.2	344.6	371.6	555.5	863.9	919.2	84%	16%	0%	0%	0%
13	206.3	346.8	372.4	556.2	863.5	916.8	72%	28%	0%	0%	0%
17	214.0	344.5	371.6	555.6	839.5	916.3	10%	0%	90%	0%	0%
24	216.3	345.3	372.9	554.8	861.6	913.8	74%	12%	12%	2%	0%
28	215.4	343.7	371.5	555.0	850.5	915.3	48%	0%	52%	0%	0%
31	219.2	348.3	374.8	554.1	844.4	910.5	0%	0%	100%	0%	0%
32	218.1	344.0	371.4	554.8	861.3	915.0	86%	6%	4%	2%	2%
33	213.2	346.7	371.7	554.9	863.6	913.8	74%	22%	0%	4%	0%
36	211.9	346.0	372.6	556.0	863.0	916.6	74%	24%	0%	2%	0%
44	214.2	342.4	371.5	554.6	862.7	915.1	98%	2%	0%	0%	0%
46	216.0	344.6	371.7	554.6	861.7	914.1	84%	12%	0%	4%	0%
50	213.2	346.3	372.2	555.9	863.3	916.6	74%	24%	0%	2%	0%
51	216.0	345.5	372.4	554.6	860.3	913.7	72%	14%	10%	4%	0%
55	213.4	346.8	372.9	555.7	862.2	916.1	72%	24%	0%	4%	0%
57	211.6	346.4	372.3	556.2	861.8	917.3	74%	22%	2%	2%	0%
58	212.2	347.2	372.6	556.5	864.2	917.6	74%	26%	0%	0%	0%
59	216.0	346.3	372.9	555.1	863.3	913.4	76%	16%	4%	4%	0%
60	214.6	346.7	371.6	556.1	863.6	916.9	74%	24%	0%	2%	0%
63	212.0	346.5	371.1	556.2	863.9	917.1	76%	24%	0%	0%	0%
70	213.4	346.6	372.7	556.3	864.3	916.6	72%	26%	0%	2%	0%
71	212.6	347.4	372.9	556.8	864.9	917.9	74%	26%	0%	0%	0%
76	214.6	345.5	372.7	554.6	862.0	914.6	76%	18%	2%	4%	0%
78	211.9	346.4	372.4	556.4	864.6	917.4	76%	24%	0%	0%	0%
86	216.2	345.2	372.3	554.8	856.0	914.0	58%	4%	38%	0%	0%
87	212.9	347.0	372.5	556.0	864.8	917.5	74%	26%	0%	0%	0%
92	213.3	346.3	372.4	556.3	864.7	917.2	76%	24%	0%	0%	0%
93	220.0	345.6	372.3	554.9	864.3	914.1	82%	12%	0%	0%	6%
94	213.6	345.9	372.5	556.1	863.8	917.0	74%	22%	4%	0%	0%

96	212.0	346.3	371.4	556.3	863.2	917.0	84%	16%	0%	0%	0%
97	214.4	346.6	372.2	556.3	864.8	917.4	76%	24%	0%	0%	0%
100	214.7	344.4	371.5	555.6	863.1	915.8	86%	10%	4%	0%	0%
101	214.1	346.0	372.3	555.9	864.1	916.7	84%	16%	0%	0%	0%
102	213.5	345.7	372.5	556.0	864.3	916.9	74%	22%	4%	0%	0%
105	213.8	345.8	372.7	555.6	862.7	916.0	74%	22%	2%	2%	0%
107	213.7	345.6	372.4	555.6	862.5	916.5	76%	18%	6%	0%	0%
109	213.2	344.8	372.9	555.6	863.9	916.3	84%	16%	0%	0%	0%
110	215.4	343.5	371.7	554.8	864.3	915.4	86%	12%	0%	2%	0%
112	214.5	345.7	373.5	554.8	860.5	913.6	72%	16%	8%	4%	0%
113	215.5	346.5	372.5	555.8	861.0	915.0	62%	16%	22%	0%	0%
114	215.9	344.4	371.5	554.6	862.0	914.4	86%	10%	0%	4%	0%
116	210.1	349.3	373.4	557.1	864.4	918.7	64%	36%	0%	0%	0%
117	211.8	347.4	373.4	556.6	864.2	917.0	75%	25%	0%	0%	0%
118	220.1	347.2	371.4	554.5	863.1	913.7	78%	14%	0%	0%	8%
119	213.2	346.1	372.4	556.1	875.3	917.1	72%	28%	0%	0%	0%
120	214.7	344.1	371.9	555.0	864.3	915.1	86%	12%	0%	2%	0%
123	216.2	349.5	375.9	554.0	859.5	912.0	46%	30%	16%	8%	0%
125	213.2	345.7	372.3	555.9	863.6	916.7	84%	16%	0%	0%	0%
126	213.1	346.1	371.9	556.0	864.6	916.9	76%	24%	0%	0%	0%
130	211.6	346.8	372.9	556.2	864.7	917.4	75%	25%	0%	0%	0%
132	212.0	346.6	372.5	556.3	864.3	917.2	72%	26%	0%	2%	0%
133	213.5	345.6	371.8	556.1	863.8	916.8	84%	16%	0%	0%	0%
134	213.0	346.7	372.1	556.3	864.4	917.2	72%	26%	0%	2%	0%
139	214.4	346.1	372.5	555.3	862.8	914.8	74%	22%	0%	4%	0%
142	216.3	346.7	373.0	555.0	860.3	913.2	62%	16%	18%	4%	0%
143	213.2	345.5	372.0	555.8	864.8	917.0	76%	24%	0%	0%	0%
148	215.0	344.3	371.8	555.4	862.4	915.4	86%	10%	2%	2%	0%
149	213.6	345.0	372.1	555.7	861.1	916.7	76%	18%	4%	2%	0%
152	212.9	346.3	372.8	556.2	864.9	917.0	76%	24%	0%	0%	0%
155	213.9	345.2	371.5	555.7	863.3	916.2	84%	14%	2%	0%	0%
158	221.8	350.6	374.9	553.4	852.1	906.9	14%	8%	70%	0%	8%
163	215.1	342.7	371.6	554.7	863.2	915.1	88%	6%	6%	0%	0%
164	212.3	347.1	372.8	556.5	864.4	917.2	75%	25%	0%	0%	0%
166	213.5	347.1	372.8	556.6	865.7	917.5	74%	26%	0%	0%	0%
168	213.7	353.4	375.3	555.4	856.6	912.4	18%	38%	38%	6%	0%
169	215.1	344.7	373.0	554.8	865.4	913.9	84%	14%	0%	2%	0%
172	216.2	347.0	373.4	555.0	861.2	912.7	72%	20%	0%	6%	2%
176	212.2	346.6	372.5	556.2	864.2	917.0	72%	26%	0%	2%	0%
177	214.3	346.3	372.6	555.7	862.1	915.2	74%	18%	6%	2%	0%
181	215.8	346.9	370.7	556.0	864.0	916.4	74%	22%	2%	2%	0%
182	213.5	344.9	372.7	555.1	865.4	915.6	84%	16%	0%	0%	0%
185	212.8	348.5	372.3	557.0	864.2	918.0	62%	36%	0%	2%	0%
186	214.1	344.3	372.0	555.3	862.9	915.8	86%	12%	0%	2%	0%
189	215.3	346.2	371.9	555.0	861.7	914.5	76%	18%	2%	4%	0%
190	215.2	344.6	372.4	555.4	863.4	916.4	84%	14%	0%	2%	0%
191	216.0	348.5	371.2	553.8	868.8	912.5	74%	24%	0%	2%	0%
193	215.6	346.6	372.7	554.8	861.1	913.6	72%	20%	2%	6%	0%
197	212.7	345.0	372.0	555.4	867.6	916.1	84%	16%	0%	0%	0%
200	216.0	345.9	372.6	555.8	865.4	915.7	80%	18%	0%	0%	2%
201	216.3	345.9	372.4	555.0	860.5	913.9	74%	14%	8%	4%	0%
202	213.3	346.2	372.3	556.0	863.6	916.7	84%	16%	0%	0%	0%
205	218.3	344.6	371.2	553.0	864.3	914.2	86%	10%	0%	4%	0%
206	213.4	347.2	372.5	556.8	864.7	917.2	75%	25%	0%	0%	0%
207	211.0	347.7	373.0	556.8	864.9	917.6	72%	28%	0%	0%	0%
209	221.3	349.1	373.3	555.1	855.6	912.8	46%	14%	32%	0%	8%

Table A7

River / (facies)	Site	Sample	HMC	tHMC	% zircon	% monazite	% garnet	% magnetite	% ilmenite	% intrabasinal	SRD (estimated grain density)	Measured grain density (g/cm^3)	standard deviation	Major potential reason for inaccurate density measures or SRD values
SOUTHERN ANGOLAN COAST														
Inamangando	Inamangando	S4945	4.0	3.1	0.04	n.f.	traces	0.2		0.0	2.68	**2.67**	*0.01*	SRD ignores mineral weathering and inclusions, underestimating density
(inner berm)	Inamangando	S4944	6.6	4.3	0.06	n.f.	0.02	1.6		0.3	2.72	**2.67**	*0.02*	SRD ignores mineral weathering and intrabasinal grains
(outer berm)	Inamangando	S4943	12.4	3.2	0.29	n.f.	0.03	8.5		0.3	2.87	**2.77**	*0.03*	Inaccurate quartering due to formation of magnetite clusters
(berm)	Bentiaba	S4948	6.9	4.2	0.06	n.f.	0.02	1.4		1.5	2.71	**2.64**	*0.01*	SRD ignores common intrabasinal grains with intragranular pores
PLACER LAG														
(foreshore)	Bentiaba	P4948	96.9	7.7	2.8	0.6	0.40	76.4	12.3	1.0	4.81	**4.61**	*0.04*	Inaccurate estimate of the average density of Fe-Ti-Cr oxides
MOÇAMEDES DESERT														
(berm)	Vanesa	S4957	3.9	2.6	0.05	n.f.	1.1	0.5		2.0	2.69	**2.67**	*0.01*	SRD ignores weathering and presence of common intrabasinal grains
(berm)	Vanesinha	S4958	15.1	11.9	0.02	n.f.	8.2	1.7		3.8	2.85	**2.78**	*0.01*	SRD ignores weathering and common intrabasinal grains
(berm)	Praia do Navio	S4959	11.8	8.0	0.26	n.f.	4.2	2.2		1.1	2.80	**2.76**	*0.00*	SRD ignores weathering and presence of intrabasinal grains
(eolian dune)	Cova dos Medos	S4961	30.2	21.0	0.50	n.f.	8.2	3.7		4.4	2.98	**2.82**	*0.01*	Inaccurate estimate of oxide density and common intrabasinal grains
(eolian dune)	Praia do Navio	S4960	51.8	27.8	1.8	n.f.	17.2	19.7		0.8	3.49	**3.26**	*0.01*	Inaccurate estimate of the average density of Fe-Ti-Cr oxides
PLACER LAGS														
(foreshore)	Vanesinha	P4958	98.8	37.3	2.0	0.3	31.6	53.4	6.6	1.4	4.57	**4.40**	*0.01*	Inaccurate estimate of the average density of Fe-Ti-Cr oxides
(foreshore)	Praia do Navio	P4959	95.7	53.8	0.95	0.3	47.8	36.1	4.2	0.5	4.33	**4.17**	*0.05*	Inaccurate estimate of the average density of Fe-Ti-Cr oxides
COASTAL NAMIB BEACH PLACERS														
(foreshore)	Shawnee	P4336	62.0	32.5	4.00	0	8.5	27.5	2.0	0.0	3.67	**3.23**	*0.06*	Magnetite clusters and mixing with laminae of non-placer sand
(foreshore)	Bayview	P4330	84.8	70.0	1.01	0	49.2	13.3	1.4	0.0	3.80	**3.75**	*0.02*	Weathering, estimate of oxide density and few intrabasinal grains

Table A8

River / (facies)	Site	Sample	GSZ class	Analysed class	SiO_2	Al_2O_3	Fe_2O_3	MgO	CaO	Na_2O	K_2O	TiO_2	P_2O_5	MnO	LOI	Total	Rb	Cs	Be
			μm	wt%	wt%	wt%	wt%	wt%	wt%	wt%	wt%	wt%	wt%	wt%	wt%	wt%	ppm	ppm	ppm
				D.L.	0.01	0.01	0.04	0.01	0.01	0.01	0.01	0.01	0.01	0.01	0.1	0.01	0.1	0.1	1
SOUTHERN ANGOLAN COAST																			
(beach)	Lucira	S 4941	63-2000 wet	96.8%	74.1	12.9	1.8	0.5	3.3	3.0	2.2	0.2	0.06	0.03	1.8	99.8	40	1	2
(outer berm)	Inamangando	S 4943	63-2000 wet	99.7%	71.7	8.9	10.2	0.2	1.5	1.7	2.9	1.6	0.06	0.14	0.8	99.6	64	1	<1
(inner berm)	Inamangando	S 4944	63-2000 wet	98.6%	78.2	10.1	2.0	0.3	2.0	1.9	3.4	0.3	0.04	0.04	1.5	99.8	70	1	<1
Inamangando	Inamangando	S 4945	63-2000 wet	95.6%	79.6	10.2	1.4	0.3	1.9	2.0	3.0	0.2	0.06	0.02	1.2	99.8	59	1	<1
Bentiaba	Bentiaba	S 4947	63-2000 wet	96.3%	79.8	10.7	0.9	0.2	1.2	2.1	4.0	0.1	0.02	0.02	0.9	99.8	81	1	<1
(beach)	Bentiaba	S 4948	63-2000 wet	100.0%	80.6	9.3	1.5	0.3	1.9	1.8	2.8	0.3	0.03	0.03	1.3	99.9	59	1	2
Giraul	Giraul	S 4951	63-2000 wet	97.1%	80.4	9.7	1.4	0.3	1.3	1.7	3.7	0.2	0.03	0.03	1.2	99.9	97	1	<1
Bero	Namibe	S 4952	63-2000 wet	98.9%	77.1	10.7	2.1	0.8	2.1	2.1	2.9	0.3	0.05	0.04	1.7	99.8	74	1	<1
(beach)	Namibe	S 4953	63-2000 wet	100.0%	75.2	9.6	3.8	1.5	3.2	1.7	2.2	0.9	0.18	0.07	1.5	99.8	55	1	<1
Curoca	Curoca mouth	S 4955	63-2000 wet	99.6%	79.5	6.5	4.0	1.0	3.1	1.2	1.3	1.0	0.78	0.13	1.4	99.8	40	1	<1
MOÇAMEDES DESERT																			
(eolian dune)	Tombua	S 4774	63-2000 wet	n.d.	81.4	6.1	2.7	1.0	3.3	1.2	1.2	0.5	0.88	0.08	1.5	99.9	37	1	<1
(beach)	Vanesa	S 4957	63-2000 wet	100.0%	86.0	5.8	1.4	0.4	1.7	1.1	1.3	0.2	0.37	0.07	1.8	100.0	41	1	<1
(beach)	Praia do Navio	S 4959	63-2000 wet	100.0%	78.3	7.0	4.3	1.0	3.6	1.2	1.1	0.7	1.00	0.17	1.7	99.9	32	1	1
(eolian dune)	Praia do Navio	S 4960	63-2000 wet	99.9%	48.5	11.0	24.9	2.3	4.0	0.7	0.6	5.1	0.85	0.98	0.5	99.4	17	1	5
HOARUSIB & CUNENE RIVER SYSTEM																			
Hoarusib	Purros	S3938	63-2000 dry	98.8%	82.8	7.3	2.4	0.8	2.3	1.8	2.3	0.5	0.06	0.03	n.d.	100.1	44	1	<1
Cunene	Matala	S 4773	63-2000 wet	n.d.	92.0	3.8	0.6	0.1	0.1	0.2	2.1	0.1	0.02	0.01	0.8	100.0	62	0	<1
Cunene	Ruacana	S 3931	63-2000 dry	97.9%	89.1	4.7	0.7	0.2	0.6	0.4	2.7	0.2	0.02	0.01	n.d.	98.6	75	1	3
Omuhongo	Oryeheke	S 3934	63-2000 dry	97.7%	74.6	12.5	2.0	0.6	2.9	2.1	3.6	0.4	0.06	0.03	1.0	99.8	85	1	<1
Cunene	Epupa Falls	S 4775	63-2000 wet	n.d.	75.8	11.6	2.6	0.8	2.9	2.0	2.4	0.7	0.05	0.04	1.1	99.9	54	1	<1
MOÇAMEDES BEACH PLACERS																			
(foreshore placer)	Bentiaba	P4948	63-2000 wet	100.0%	5.6	1.2	77.9	0.2	0.9	0.1	0.1	11.8	0.57	0.97	-1.8	97.6	4	0	0.5
(foreshore placer)	Vanesinha	P4958	63-2000 wet	100.0%	17.2	8.6	51.8	1.9	1.4	0.0	0.1	16.2	0.15	1.48	-1.0	97.8	3	0	0.5
(foreshore placer)	Praia do Navio	P4959	63-2000 wet	100.0%	24.5	12.5	43.4	2.5	2.5	0.1	0.1	11.7	0.33	1.72	-0.5	98.7	4	0	0.5
COASTAL NAMIB BEACH PLACERS																			
(foreshore placer)	Shawnee	P4336	bulk	100.0%	38.5	12.6	35.5	4.2	3.3	0.4	0.3	3.9	0.12	1.07	-0.6	99.3	8	0	2
(foreshore placer)	Bayview	P4330	bulk	100.0%	52.6	6.2	25.2	3.4	3.9	1.1	0.7	4.1	0.16	0.36	1.0	98.9	25	0	1

Sample	Sr	Ba	Sc	Y	La	Ce	Pr	Nd	Sm	Eu	Gd	Tb	Dy	Ho	Er	Tm	Yb	Lu	Th	U	Zr	Hf	V	Nb	Ta	Cr
	ppm	ppm	ppm	ppm	ppm	ppm	ppm	ppm	ppm	ppm	ppm	ppm	ppm	ppm	ppm	ppm	ppm	ppm	ppm	ppm	ppm	ppm	ppm	ppm	ppm	ppm
	0.5	1	1	0.1	0.1	0.1	0.02	0.3	0.05	0.02	0.05	0.01	0.05	0.02	0.03	0.01	0.05	0.01	0.2	0.1	0.1	0.1	8	0.1	0.1	14
S 4941	463	866	6	7	19	36	4	16	3	0.8	2	0.3	1	0.3	1	0.1	1	0.1	3	0	71	2	35	3	0.2	14
S 4943	279	904	6	36	123	253	29	100	15	1.2	11	1.3	7	1.3	4	0.5	3	0.5	48	3	685	16	171	33	2.0	68
S 4944	306	911	5	9	23	43	5	18	3	0.5	3	0.4	2	0.4	1	0.2	1	0.2	11	1	168	5	39	6	0.4	14
S 4945	354	987	6	6	18	33	4	14	2	0.6	2	0.3	1	0.3	1	0.1	1	0.1	5	1	306	8	28	4	0.4	<14
S 4947	278	1110	2	4	11	21	2	9	1	0.4	1	0.1	1	0.1	0	0.1	0	0.1	3	0	52	1	18	2	0.2	<14
S 4948	322	845	4	7	15	29	4	12	2	0.5	2	0.2	1	0.3	1	0.1	1	0.1	5	0	72	2	28	5	0.5	<14
S 4951	255	878	3	6	14	25	3	12	2	0.5	2	0.2	1	0.2	1	0.1	1	0.1	11	1	92	2	28	3	0.4	21
S 4952	320	916	5	8	15	25	3	12	2	0.7	2	0.3	1	0.4	1	0.1	1	0.1	3	1	84	2	40	3	0.3	48
S 4953	351	657	11	14	17	36	5	19	3	1.0	3	0.5	3	0.6	2	0.2	2	0.2	4	1	168	4	80	10	0.7	82
S 4955	196	310	10	28	16	31	4	14	3	0.7	3	0.6	4	1.1	4	0.6	4	0.6	6	4	785	19	83	11	0.8	89
S 4774	188	222	7	22	15	30	3	13	3	0.6	3	0.5	3	0.7	2	0.4	3	0.4	4	4	403	10	56	8	0.7	62
S 4957	129	285	4	14	8	17	2	7	2	0.4	2	0.4	2	0.6	2	0.3	2	0.3	2	2	55	2	22	6	0.6	21
S 4959	193	233	12	36	16	34	4	16	3	0.7	4	0.8	5	1.4	5	0.7	5	0.8	4	4	265	7	70	8	0.6	62
S 4960	183	122	56	159	40	86	10	38	8	1.1	10	2.8	23	6.2	23	3.7	28	4.4	22	8	3106	77	380	56	5.9	281
S3938	144	566	5	13	13	30	3	14	2	0.6	2	0.4	2	0.5	2	0.3	1	0.2	4	1	248	6	34	6	0.4	27
S 4773	19	280	<1	6	6	12	1	5	1	0.4	1	0.2	1	0.2	1	0.1	1	0.1	3	1	192	5	13	13	1.0	<14
S 3931	60	587	2	6	8	15	2	6	1	0.3	1	0.2	1	0.2	1	0.1	1	0.1	3	1	71	2	21	6	0.4	41
S 3934	237	1062	4	9	13	20	3	8	2	0.6	2	0.3	2	0.4	1	0.2	1	0.2	8	1	286	8	33	5	0.2	68
S 4775	257	710	4	8	11	23	3	11	2	0.7	2	0.3	2	0.3	1	0.1	1	0.1	4	0	106	3	51	6	0.4	41
P4948	75	42	34	494	1805	3779	429	1502	232	13.4	161	18.2	92	15.9	45	6.6	43	6.7	812	38	6972	176	1336	189	16.8	541
P4958	24	25	83	240	94	191	22	79	16	1.3	18	4.0	34	8.7	31	5.5	40	6.9	73	20	13131	323	1038	172	13.9	657
P4959	63	38	96	285	43	93	11	40	9	1.2	15	4.0	37	10.3	37	6.5	47	7.6	36	13	7254	177	757	127	10.0	452
P4336	44	67	96	271	41	84	10	37	8	1.0	13	3.9	38	9.1	31	5.4	39	6.4	33	8	3585	91	497	61	5.8	506
P4330	92	152	36	94	60	115	14	49	9	1.2	9	1.8	14	3.1	10	1.8	13	2.3	44	9	6776	166	631	54	4.2	534

Sample	a.r.d. Mo	W	Co	Ni	a.r.d. Ni	a.r.d. Cu	a.r.d. Ag	a.r.d. Au	a.r.d. Zn	a.r.d. Cd	a.r.d. Hg	Ga	a.r.d. Tl	Sn	a.r.d. Pb	a.r.d. As	a.r.d. Sb	a.r.d. Bi	a.r.d. Se	TOT/C	TOT/S
	ppm	ppm	ppm	ppm	ppm	ppm	ppm	ppb	ppm	ppm	ppm	ppm	ppm	ppm	ppm	ppm	ppm	ppm	ppm	wt%	wt%
	0.1	0.5	0.2	0.1	20	0.1	0.1	0.5	1	0.1	0.01	0.5	0.1	1	0.1	0.5	0.1	0.1	0.5	0.02	0.02
S 4941	0.2	<0.5	5	<20	4	5	<0.1	<0.5	12	<0.1	<0.01	13	<0.1	<1	5	1	<0.1	<0.1	<0.5	0.12	<0.02
S 4943	0.1	1.1	4	<20	3	n.d.	<0.1	<0.5	n.d.	<0.1	<0.01	9	<0.1	2	5	1	<0.1	<0.1	<0.5	0.05	<0.02
S 4944	0.1	7.4	2	<20	2	n.d.	<0.1	<0.5	n.d.	<0.1	<0.01	9	<0.1	<1	3	1	<0.1	<0.1	<0.5	0.11	<0.02
S 4945	<0.1	0.9	1	<20	2	3	<0.1	<0.5	8	<0.1	<0.01	10	<0.1	<1	3	<0.5	<0.1	<0.1	<0.5	0.06	<0.02
S 4947	<0.1	3.8	1	<20	1	3	<0.1	<0.5	7	<0.1	<0.01	9	<0.1	<1	3	<0.5	<0.1	<0.1	<0.5	0.05	<0.02
S 4948	0.1	1.0	2	<20	1	2	<0.1	1	5	<0.1	<0.01	9	<0.1	<1	3	<0.5	<0.1	<0.1	<0.5	0.08	<0.02
S 4951	0.2	0.6	2	<20	3	5	<0.1	<0.5	6	<0.1	<0.01	8	<0.1	<1	4	<0.5	<0.1	<0.1	<0.5	0.03	<0.02
S 4952	0.1	0.6	5	<20	8	7	<0.1	<0.5	11	<0.1	<0.01	9	<0.1	<1	3	1	<0.1	<0.1	<0.5	0.04	<0.02
S 4953	0.2	1.8	9	24	9	6	<0.1	<0.5	13	<0.1	<0.01	9	<0.1	1	4	2	<0.1	<0.1	<0.5	0.04	<0.02
S 4955	0.2	2.5	7	<20	5	5	<0.1	2	12	<0.1	<0.01	7	<0.1	1	3	2	<0.1	<0.1	<0.5	0.13	<0.02
S 4774	0.2	0.6	5	<20	7	7	<0.1	<0.5	11	<0.1	<0.01	6	<0.1	2	3	3	<0.1	<0.1	<0.5	0.17	0.03
S 4957	0.2	<0.5	2	<20	3	4	<0.1	<0.5	6	<0.1	<0.01	5	<0.1	<1	2	3	<0.1	<0.1	<0.5	0.09	<0.02
S 4959	0.4	<0.5	5	<20	5	6	<0.1	<0.5	11	<0.1	<0.01	7	<0.1	1	3	4	<0.1	<0.1	0.5	0.13	0.03
S 4960	0.7	2.6	27	26	12	10	<0.1	<0.5	29	0.1	<0.01	13	<0.1	9	5	3	0.1	0.1	<0.5	0.1	0.03
S3938	<0.1	<0.5	3	<20	5	5	<0.1	<0.5	11	<0.1	<0.01	6	<0.1	<1	3	<0.5	<0.1	<0.1	<0.5	n.d.	n.d.
S 4773	0.4	0.6	1	<20	1	2	<0.1	<0.5	15	<0.1	<0.01	5	<0.1	<1	4	<0.5	<0.1	<0.1	<0.5	0.08	<0.02
S 3931	<0.1	0.8	1	<20	2	2	<0.1	2	7	<0.1	<0.01	4	<0.1	<1	2	<0.5	<0.1	<0.1	<0.5	n.d.	n.d.
S 3934	0.4	0.7	4	<20	8	7	<0.1	<0.5	9	<0.1	<0.01	11	0.1	<1	3	<0.5	<0.1	0.2	<0.5	0.05	0.08
S 4775	<0.1	<0.5	6	<20	12	4	<0.1	<0.5	12	<0.1	<0.01	8	<0.1	<1	4	<0.5	<0.1	<0.1	<0.5	0.04	<0.02
P4948	0.3	5.6	33	13	13	5	0.1	0	29	0.1	0.0	18	0.1	9	25	1	0.1	0.1	0.5	0.03	0.01
P4958	0.8	4.6	46	19	19	15	0.1	0	48	0.1	0.0	18	0.1	15	7	1	0.1	0.1	0.3	0.02	0.01
P4959	0.7	3.8	42	15	15	14	0.1	0	37	0.1	0.0	18	0.1	11	5	2	0.1	0.1	0.3	0.03	0.01
P4336	0.9	2.8	40	26	18	18	0.1	2	39	0.2	0.0	15	0.1	8	8	3	0.2	0.2	0.3	0.04	0.02
P4330	0.9	4.6	31	31	19	16	0.1	2	45	0.1	0.0	15	0.1	7	8	3	0.2	0.1	0.3	0.08	0.03

Sample	CIA	PIA	CIW	CIX	WIP	CIA/WIP	$\alpha^{Al}Mg$	$\alpha^{Al}Ca$	$\alpha^{Al}Na$	$\alpha^{Al}K$	$\alpha^{Al}Rb$	$\alpha^{Al}Sr$	$\alpha^{Al}Ba$	LaN/YbN	LaN/SmN	GdN/HoN	HoN/YbN	Eu/Eu*	Ce/Ce*	MREE/MREE*
S 4941	50	49	54	64	55	0.9	4.3	1.0	1.0	1.2	2.1	0.6	0.6	23.7	4.3	2.1	1.5	1.06	0.90	1.34
S 4943	51	52	63	60	44	1.2	7.2	1.5	1.3	0.6	0.9	0.7	0.4	25.3	5.0	2.4	1.1	0.28	0.98	0.76
S 4944	49	49	60	60	52	0.9	5.5	1.3	1.2	0.6	0.9	0.7	0.4	13.5	4.2	1.6	1.1	0.56	0.88	0.98
S 4945	51	51	61	61	49	1.0	6.3	1.4	1.2	0.7	1.1	0.6	0.4	13.7	4.5	1.6	1.0	0.81	0.90	1.03
S 4947	52	54	66	58	56	0.9	9.7	2.3	1.2	0.5	0.8	0.8	0.4	19.0	5.3	2.6	0.8	0.90	0.95	1.08
S 4948	50	50	60	61	46	1.1	5.3	1.3	1.2	0.7	1.0	0.6	0.4	12.0	4.0	1.8	0.9	0.74	0.93	1.10
S 4951	52	53	66	59	51	1.0	5.1	1.9	1.3	0.5	0.6	0.8	0.4	14.0	5.0	2.0	0.9	0.85	0.85	1.00
S 4952	51	52	60	62	51	1.0	2.1	1.3	1.2	0.8	0.9	0.7	0.4	10.6	4.5	1.5	1.1	1.08	0.83	1.31
S 4953	48	47	54	65	46	1.0	1.0	0.8	1.3	0.9	1.1	0.6	0.6	6.9	3.0	1.7	1.0	0.88	0.91	1.39
S 4955	48	47	53	66	30	1.6	1.0	0.5	1.3	1.0	1.0	0.7	0.8	2.7	3.3	0.8	0.8	0.71	0.92	0.85
S 4774	46	45	51	66	29	1.6	0.9	0.5	1.2	1.1	1.0	0.7	1.1	3.9	3.4	1.1	0.8	0.69	0.99	0.99
S 4957	52	53	60	64	25	2.1	2.3	0.9	1.3	0.9	0.9	1.0	0.8	2.5	3.4	0.8	0.8	0.73	0.95	0.91
S 4959	49	49	54	69	28	1.7	1.1	0.5	1.4	1.3	1.4	0.8	1.1	2.2	3.2	0.7	0.8	0.61	0.97	0.83
S 4960	61	62	63	86	25	2.5	0.7	0.7	3.7	4.0	4.1	1.3	3.5	1.0	3.1	0.4	0.6	0.37	0.98	0.57
S3938	44	41	52	58	43	1.0	1.5	0.8	1.0	0.6	1.1	1.1	0.5	5.9	3.7	1.3	0.9	0.79	1.07	1.08
S 4773	58	76	89	60	20	2.9	4.9	8.1	4.7	0.4	0.4	4.4	0.5	5.5	4.2	1.2	0.8	1.23	0.95	1.14
S 3931	51	52	74	57	28	1.8	3.8	2.2	2.7	0.4	0.4	1.7	0.3	7.2	4.8	1.3	0.9	0.83	0.97	1.11
S 3934	50	50	59	63	59	0.9	3.2	1.1	1.4	0.7	0.9	1.2	0.5	8.7	4.6	1.3	1.1	1.08	0.80	1.17
S 4775	51	52	58	66	48	1.1	2.2	1.0	1.4	1.0	1.4	1.0	0.6	8.8	3.5	1.5	1.1	1.12	0.95	1.33
P4948	69	72	74	86	2	30.7	1.1	0.3	5.7	2.5	1.8	0.4	1.1	28.6	4.9	2.8	1.1	0.21	0.99	0.72
P4958	79	79	80	99	9	8.9	0.7	1.6	67.3	34.8	20.2	8.0	13.2	1.6	3.7	0.6	0.6	0.23	0.97	0.55
P4959	76	77	77	98	14	5.6	0.8	1.3	36.5	28.0	20.7	4.4	12.6	0.6	3.1	0.4	0.6	0.32	0.99	0.53
P4336	66	66	67	93	25	2.6	0.5	1.0	7.4	10.2	9.9	6.3	7.2	0.7	3.2	0.4	0.7	0.29	0.94	0.61
P4330	40	39	42	70	35	1.1	0.3	0.4	1.3	1.8	1.6	1.5	1.6	3.0	4.0	0.8	0.7	0.38	0.93	0.72

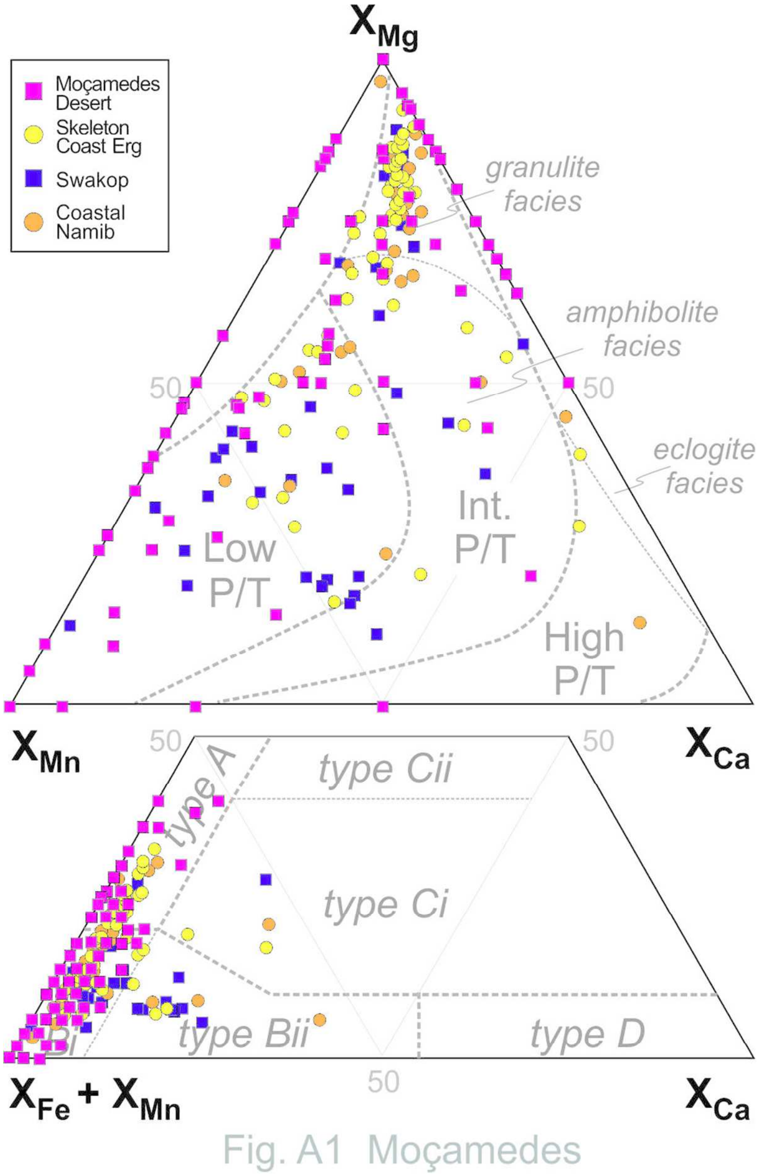

90x140mm (300 x 300 DPI)